

THE POLARIZATION SAGNAC INTERFEROMETER  
FOR GRAVITATIONAL WAVE DETECTION

A DISSERTATION  
SUBMITTED TO THE DEPARTMENT OF PHYSICS  
AND THE COMMITTEE ON GRADUATE STUDIES  
OF STANFORD UNIVERSITY  
IN PARTIAL FULFILLMENT OF THE REQUIREMENTS  
FOR THE DEGREE OF  
DOCTOR OF PHILOSOPHY

Peter T. Beyersdorf

January 2001

© Copyright by Peter T. Beyersdorf 2001  
All Rights Reserved

I certify that I have read this dissertation and that in my opinion it is fully adequate, in scope and quality, as a dissertation for the degree of Doctor of Philosophy.

---

R.L. Byer  
(Principal Adviser)

I certify that I have read this dissertation and that in my opinion it is fully adequate, in scope and quality, as a dissertation for the degree of Doctor of Philosophy.

---

M.M. Fejer

I certify that I have read this dissertation and that in my opinion it is fully adequate, in scope and quality, as a dissertation for the degree of Doctor of Philosophy.

---

Steven Chu

Approved for the University Committee on Graduate Studies:

# Abstract

Future advanced interferometric gravitational wave detectors will be limited by thermal distortions induced by high circulating power. An all-reflective configuration based on the Sagnac interferometer, presented here, is well suited to operation with high circulating power. A polarization scheme is presented that allows the interferometer to be used in a reciprocal configuration, so that static imperfections and thermally induced distortions of the beamsplitter and optics have a minimal effect on the interference contrast. The necessary low-frequency response of the interferometer requires delay-lines in the arms. To deal with the noise introduced by scattered light in the delay lines, a laser frequency sweep is presented that frequency shifts the scattered light so that it does not produce noise in the measurement band. The control requirements and alignment tolerances are calculated for the components of the detector and they are compared with the levels necessary for an alternative interferometer configuration, the Fabry-Perot Michelson, to highlight the advantages and disadvantages of the polarization Sagnac interferometer.

The all-reflective delay-line polarization Sagnac interferometer design is demonstrated on a 10 m prototype interferometer with suspended optics that incorporates the laser frequency sweep to provide a shot-noise-limited phase sensitivity of  $\Delta\phi = 10^{-9} \text{radHz}^{-1/2}$  at frequencies as low as 200 Hz. Scaling this prototype to several kilometers with kilowatts of circulating power requires several technical improvements in high-power solid-state lasers, second harmonic generation, and the fabrication of large mirrors, which are likely to be made in the next 10 years.

# Preface

The idea of using a Sagnac interferometer for gravitational wave detection was independently proposed by J. Anandan in 1982 and Rai Weiss at MIT in 1986. The motivation for considering this configuration was the potential to reduce the control effort of the detector and integrate a full gravitational period to produce a useful signal. Despite the belief that these qualities would be useful for a future interferometric detector, relatively little resources were devoted to investigating the Sagnac. Nearly 10 years later Marty Fejer at Stanford University, who was familiar with the Sagnac interferometer for fiber gyroscopes and for various laser applications which were being investigated by Tony Siegman at Stanford University, began considering the Sagnac interferometer for gravitational wave detection, hoping to exploit the properties that make fiber gyroscopes so robust.

Experimental investigation of the Sagnac interferometer for gravitational wave detection began in 1994 by Ke-Xun Sun, a post doc working for R.L. Byer. His preliminary work exposed the problem of detecting on the reciprocal port of the beamsplitter while simultaneously detecting the dark fringe of the interference. His search for a method of generating an appropriate local oscillator field led to the signal extraction scheme based on a local oscillator orthogonally polarized to the signal, which has been modified for the polarization Sagnac interferometer. He was also the first to demonstrate a Sagnac interferometer with a diffractive beamsplitter, although he did not address the challenges of using such a design in an advanced detector.

In 1996 two graduate students on opposite sides of the earth began independent studies of the Sagnac interferometer for gravitational wave detection. Daniel Shaddock at the Australian National University investigated resonant sideband extraction

in the Sagnac with ring cavities in the arms. His investigations concluded that there was no advantage to using the Sagnac in a resonant configuration. At the same time I began working closely with Marty Fejer and Ke-Xun Sun at Stanford University investigating the Sagnac interferometer with delay lines in the arms.

We knew we faced several challenges to develop this configuration into something appropriate for an advanced detector. The first was to find a way to allow detection of the dark fringe of interference at the reciprocal port of the beamsplitter. This was necessary for an advanced detector; without it any Sagnac design would be of no more utility than the sketch initially drawn by Rai Weiss in his notebook back in 1986. Secondly we knew from studies on delay lines in Michelson interferometers over the last several decades, much of which was conducted at Garching, Germany for GEO, that noise would be introduced by stray light trapped in the delay lines. Modulation schemes had been proposed to suppress this noise but it was unclear which, if any, would be the most appropriate option for a Sagnac interferometer.

We have addressed these issues and believe that our work will allow a more informed evaluation of the Sagnac interferometer for an advanced gravitational wave detector.

# Acknowledgments

To my advisor, Bob Byer, for having confidence in me,

to Marty Fejer for challenging me to see my research in a broader scope,

to Eric Gustafson for transferring so much knowledge to me,

to Mike Hennessey for building the infrastructure for my experiment,

to my friends and family for their emotional support during this endeavor,

and

to Joyce Kuo for giving me an escape from the world of physics

thank you.

# Contents

<b>Abstract</b>	<b>iv</b>
<b>Preface</b>	<b>v</b>
<b>Acknowledgments</b>	<b>vii</b>
<b>1 Introduction to General Relativity</b>	<b>1</b>
1.1 Gravity in general relativity . . . . .	2
1.2 Gravitational radiation . . . . .	5
1.3 Sources of gravitational radiation . . . . .	7
<b>2 Principles of gravitational wave detection</b>	<b>9</b>
2.1 Measures of detector performance . . . . .	9
2.2 Observable effects of gravitational waves . . . . .	11
2.2.1 A Michelson interferometer as an antenna for gravitational radiation . . . . .	12
2.2.2 A Sagnac interferometer as an antenna for gravitational radiation	16
2.3 Detection of signal sidebands . . . . .	20
2.3.1 Optical homodyne detection . . . . .	23
2.3.2 Optical heterodyne detection . . . . .	23
2.4 Understanding measurement noise . . . . .	24
2.4.1 Seismic noise . . . . .	24
2.4.2 Thermal noise . . . . .	25
2.4.3 Quantum Noise . . . . .	25

2.4.4	Other noise sources . . . . .	27
2.5	The LIGO project . . . . .	28
2.6	Other Gravitational Wave Observatories . . . . .	28
<b>3</b>	<b>The Polarization Sagnac Interferometer</b>	<b>31</b>
3.1	Interferometer Topology . . . . .	33
3.1.1	The need for delay lines in the interferometer arms . . . . .	35
3.1.2	Zero-area Sagnac as a common path interferometer . . . . .	36
3.1.3	Using the Sagnac in a Reciprocal Configuration . . . . .	38
3.2	Polarization control in the Sagnac interferometer . . . . .	40
3.3	Signal readout in the polarization Sagnac Interferometer . . . . .	41
3.4	Experimental investigations of a tabletop polarization Sagnac interferometer . . . . .	43
3.4.1	Fringe Contrast . . . . .	44
3.4.2	Birefringence . . . . .	45
3.4.3	Laser frequency noise . . . . .	46
3.4.4	Laser amplitude noise . . . . .	48
3.5	Summary . . . . .	49
<b>4</b>	<b>Delay lines for energy storage</b>	<b>50</b>
4.1	The delay line design . . . . .	52
4.1.1	Delay line geometry . . . . .	52
4.1.2	Gaussian beam parameters of the beam in the delay line . . . . .	55
4.1.3	Delay line mirror size . . . . .	57
4.1.4	Effect of beam clipping . . . . .	63
4.2	Implementation of the delay line . . . . .	65
4.2.1	Alignment tolerances of the delay line . . . . .	65
4.2.2	Thermal noise from the delay line mirrors . . . . .	66
4.2.3	Laser frequency sweep to control scattered light noise . . . . .	69
4.3	Conclusion . . . . .	75

<b>5</b>	<b>Alignment tolerances</b>	<b>76</b>
5.1	Parameters for the alignment calculations . . . . .	77
5.1.1	Power recycled Fabry-Perot Michelson interferometer . . . . .	77
5.1.2	Polarization Sagnac interferometer . . . . .	78
5.2	Alignment and stability of core optics . . . . .	79
5.2.1	Sensitivity to mirror tilt . . . . .	79
5.2.2	Sensitivity to mirror translation . . . . .	83
5.3	Sensitivity to laser noise . . . . .	88
5.4	Polarization effects . . . . .	90
5.5	Internal loss . . . . .	93
5.6	Summary of alignment and control requirements . . . . .	93
<b>6</b>	<b>Scaling to High-Power</b>	<b>96</b>
6.1	Thermal distortions . . . . .	96
6.2	Reflective optics . . . . .	104
6.2.1	Grating beamsplitter . . . . .	104
6.2.2	Reflective waveplates . . . . .	110
6.2.3	Spatial filter . . . . .	111
6.3	The polarization Sagnac with reflective optics . . . . .	112
6.3.1	The suspension system . . . . .	112
6.3.2	The reflective optics . . . . .	117
6.3.3	Scattered light in the interferometer . . . . .	119
6.4	Summary . . . . .	122
<b>7</b>	<b>Conclusion</b>	<b>123</b>
7.1	Summary of this work . . . . .	123
7.2	Future work . . . . .	125
<b>A</b>	<b>Methods to reduce scattered light noise</b>	<b>127</b>
	<b>Bibliography</b>	<b>133</b>

# List of Tables

5.1	A comparison of the alignment and control requirements for the Michelson and Sagnac interferometers . . . . .	95
6.1	Absorption coefficients and material parameters of some relevant optical materials. . . . .	98
6.2	Material parameters of some relevant optical materials. . . . .	101

# List of Figures

1.1	Gravitational wave strain fields . . . . .	6
2.1	The interaction of a gravitational wave with a Michelson interferometer	12
2.2	The power recycled Fabry-Perot Michelson interferometer . . . . .	14
2.3	the Sagnac interferometer . . . . .	16
2.4	The response of a LIGO-scale Sagnac and Michelson interferometer .	18
2.5	The phasor representation of a single frequency wave . . . . .	20
2.6	The phasor representation of phase modulation . . . . .	21
2.7	The phasor representation of an amplitude modulated wave . . . . .	22
2.8	The spectrum of various noise sources in an interferometric gravita- tional wave detector . . . . .	24
2.9	Sensitivity curves for LIGO I, LIGO II and an advanced LIGO detector	30
3.1	The layout of the Michelson and Sagnac interferometers. . . . .	32
3.2	The asymmetry of optics in the Sagnac interferometer. . . . .	35
3.3	The reciprocal configuration for the Sagnac interferometer . . . . .	39
3.4	Output polarization state of the polarization Sagnac interferometer. .	42
3.5	Heterodyne detection scheme for the polarization Sagnac interferometer.	43
3.6	Optical layout for a tabletop delay line Sagnac interferometer. . . . .	44
3.7	Output power versus internal birefringence in the polarization Sagnac interferometer . . . . .	46
3.8	Measurement of the frequency noise suppression of the polarization Sagnac interferometer. . . . .	47

3.9	Demonstration of the amplitude noise suppression due to balanced detection. . . . .	48
4.1	The response of the delay line Sagnac interferometer . . . . .	51
4.2	The the ray position and angle for calculations with the ABCD matrices	53
4.3	The pattern of reflection spots on a delay line mirror. . . . .	59
4.4	The minimum mirror diameter required for various delay line configurations as a function of the number of spots on the mirror. . . . .	62
4.5	Interference contrast as a function of beam clipping in a delay-line Sagnac interferometer. . . . .	64
4.6	Effects of thermal noise in delay line mirrors. . . . .	68
4.7	Effect of scattered light on measurement phase uncertainty. . . . .	69
4.8	The ideal modulation waveform for laser frequency sweep. . . . .	71
4.9	The achievable waveform for laser frequency sweep. . . . .	71
4.10	Effect of scattered light on the output noise spectrum with and without laser frequency sweep. . . . .	74
5.1	The power recycled Fabry-Perot Michelson interferometer. . . . .	78
5.2	The delay-line polarization Sagnac interferometer. . . . .	79
5.3	The displacement of the center of the spot pattern relative to the mirror center allows tilt noise to couple into the signal. Offset of the center of the spot pattern together with a tilted mirror couples pointing noise of the laser and tilt noise of the optic into phase noise at the interferometer output. . . . .	80
6.1	The axial surface deformation of a cylindrical substrate illuminated with a Gaussian beam. . . . .	102
6.2	The radial surface deformation of a cylindrical substrate illuminated with a Gaussian beam. . . . .	103
6.3	Illustration of the transfer of frequency noise of the laser to pointing noise of the diffracted beam. . . . .	105

6.4	The displacement of the diffracted beam as a function of distance from the grating when the laser frequency is swept over 20 GHz. . . . .	106
6.5	The total phase distortion of a wavefront reflected (top curve) and diffracted (bottom curve) from a thermally loaded grating. The magnitude of the distortion is normalized to $k_o u_c$ . For silicon optics an absorbed power of about 15 W will produce a phase distortion of $\lambda/100$ across the beam waist for a wavelength of $532nm$ . . . . .	109
6.6	A resonant cavity with a grating as an input coupler . . . . .	112
6.7	The 10 m Sagnac. . . . .	113
6.8	The delay line suspension system located within the Engineering test Facility 10 m vacuum system end tank . . . . .	115
6.9	An overview of the suspension system . . . . .	116
6.10	The reference beam for interferometer alignment . . . . .	118
6.11	10 m interferometer noise spectrum with and without laser frequency sweep . . . . .	120
6.12	The low frequency noise floor of the polarization Sagnac interferometer.	121
A.1	The spot pattern in a delay line with (a) coherent illumination and (b) incoherent illumination. The interference effects where the beams overlap are not present with the incoherent illumination . . . . .	128

A.2 Scattered light noise with laser illumination and with low coherence ASE illumination. A thin wire was placed in front of one delay line mirror to introduce scatter that couples seismic noise and laser frequency noise to the output signal. The top curve (solid trace) shows the noise level from 0 to 10 MHz when a highly coherence Nd:YAG laser illuminates the interferometer. The noise level is measured relative to the noise level with low-coherence ASE illumination (dashed trace). The noise from scattered light has a frequency dependence because of the relative delay of the scattered light compared to the main beam. The coupling of scattered light noise to the output is nulled at frequencies corresponding to the relative delay of the scattered light. With low coherence illumination the output noise level is comparable to the noise level with highly coherent illumination at the null frequencies indicating that the scatted light noise has been suppressed below the electronic noise floor of the measurement. . . . . 132

# Chapter 1

## Introduction to General Relativity

Einstein's theory of general relativity provides a description of gravity that differs from the Newtonian theory in regions of high energy density. One of the consequences of these differences is the prediction of gravitational radiation, traveling waves in the fabric of space-time in general relativity. Today an immense effort is underway in the physics community to build receivers capable of detecting gravitational radiation both to confirm the validity of General Relativity and also to observe regions of high energy density in the universe.

Several first-generation interferometric receivers are being built, and although their sensitivity will likely not be great enough to detect gravitational waves, the second and third generation receivers now being considered will likely have enough sensitivity to make such a detection. With each successive generation of receiver, new laser technological, control systems advances, and material breakthroughs allow the sensitivity to be improved over the previous generation.

The polarization Sagnac interferometer explored in this thesis requires different performance characteristics from the detector subsystems than the recycled Fabry-Perot Michelson interferometer used for the first generation receivers. Although the development of the Sagnac interferometer requires solutions to a new set of engineering problems, it promises more robust operation with high circulating power than the Fabry-Perot Michelson interferometer, an advantage in an advanced detector. This thesis characterizes the polarization Sagnac interferometer so that the technology

advances necessary to make it a feasible candidate for an advanced receiver can be understood. The thesis also lays the groundwork for the research necessary to develop the interferometer for an advanced detector.

Before addressing the interferometer design and characteristics, I present an introduction to gravitational radiation in general relativity followed by a discussion of some principles of gravitational wave detection. In this chapter I describe the interaction of energy and space-time followed by a description of gravitational radiation, the travelling wave solutions to the distortions in space-time caused by a changing energy distribution. Finally I describe some astrophysical events which are expected to produce gravitational radiation which might be detectable by earth based interferometric detectors. These descriptions are meant as a guide for a reader with some understanding of the theory of General Relativity. For a more complete picture of General Relativity consult a text such as *A first course in General Relativity* by Schutz [1] or *Gravitation* by Misner, Thorne and Wheeler[2]. In chapter 2 the manifestation of the curvature of space time to an interferometric detector is discussed.

## 1.1 Gravity in general relativity

In Newtonian physics gravity is a force between massive objects described by

$$F_{12} = -G \frac{m_1 m_2}{r_{12}^2} \quad (1.1)$$

where  $G = 6.673 \times 10^{-11} N m^2 / kg^2$  is the universal gravitational constant, and  $r_{12}$  is the separation between masses  $m_1$  and  $m_2$ . Although this description of gravity is adequate for most practical applications, it is flawed in that it assumes instantaneous action at a distance. In General Relativity, gravity is instead considered a warping of space and time by energy – including the rest mass energy of objects. In this geometric interpretation of gravity, the trajectory of the center of mass of a freely falling objects lies on a geodesic of space-time and is therefore governed by the space-time curvature produced by other objects.

*Space-time* is the 4 dimensional fabric of the universe which contains the coordinate grid that is used to describe time and position. The metric is a tensor that measures the separation of coordinates on that grid. In the absence of gravity, space-time is flat; the geodesics which describe the motion of objects are straight lines, locally parallel lines remain parallel to infinity and the separation of coordinates is measured by the Minkowski metric

$$\eta = \begin{bmatrix} -c & 0 & 0 & 0 \\ 0 & 1 & 0 & 0 \\ 0 & 0 & 1 & 0 \\ 0 & 0 & 0 & 1 \end{bmatrix}. \quad (1.2)$$

This can be used to define the magnitude of the invariant interval,  $d\vec{s}$ , between events with coordinate  $x_1$  and  $x_2$ . For

$$d\vec{s} = \begin{bmatrix} t_1 \\ x_1 \\ y_1 \\ z_1 \end{bmatrix} - \begin{bmatrix} t_2 \\ x_2 \\ y_2 \\ z_2 \end{bmatrix}, \quad (1.3)$$

the magnitude of the invariant interval squared is a function of the metric

$$ds^2 = d\vec{s}^\mu g_{\mu\nu} d\vec{s}^\nu. \quad (1.4)$$

(In this chapter the *Einstein summation convention* is used; any product of tensor components with a common index raised and lowered is understood to represent a sum over all values of the common index.) The magnitude of this interval reveals information about the metric and is measured by the gravitational wave interferometer as described in chapter 2.

Gravity, however, warps space-time so that the geodesics are no longer straight lines, locally parallel lines eventually intersect and the metric tensor is no longer diagonal.

The relationship between the curvature of space-time and the gravitational source

is contained in the Einstein field equations, which when written in a frame invariant form, give the tensor relationship

$$\mathbf{T} = \frac{c^4}{8\pi G} \mathbf{G}. \quad (1.5)$$

Here the source of gravity is  $\mathbf{T}$ , the stress energy tensor describing the distribution of mass, energy and momentum.  $\mathbf{G} = \mathbf{R} - \frac{1}{2}\mathbf{g}R$  is the Einstein curvature tensor, a function of the Ricci tensor  $\mathbf{R}$  and the Ricci scalar  $R$  defined by

$$R = g^{\mu\nu} R_{\mu\nu} \quad (1.6)$$

$$R_{\mu\nu} = R_{\mu\nu\alpha}^{\alpha} \quad (1.7)$$

where  $g^{\mu\nu}$  is the metric and  $R_{\beta\mu\nu}^{\alpha}$  is the Riemann tensor describing the global deviation from parallelism of locally parallel lines. The Riemann tensor can be expressed in terms of the metric by

$$R_{\beta\mu\nu}^{\alpha} = \frac{1}{2}g^{\alpha\sigma} (\partial_{\beta}\partial_{\mu}g_{\sigma\nu} - \partial_{\beta}\partial_{\nu}g_{\sigma\mu} + \partial_{\sigma}\partial_{\nu}g_{\beta\mu} - \partial_{\sigma}\partial_{\mu}g_{\beta\nu}). \quad (1.8)$$

The constant of proportionality between the stress and strain of space-time in equation 1.5  $\frac{c^4}{8\pi G} = 4.83 \times 10^{42} J/m$  is extremely large. Thus extremely large energy densities are necessary to produce a significant amount of curvature in space-time. In regions without a high energy density the metric of curved space-time can approximated by a first order expansion about the metric of flat space-time.

$$\mathbf{g} \approx \eta + \mathbf{h} \quad (1.9)$$

where  $h_{\mu,\nu} \ll \eta_{\mu,\nu}$ . This approximation is valid in all but the most exotic environments such as near black holes, at the surface of neutron stars, etc. In the next section I show that in empty space the Einstein field equations have travelling wave solutions in the perturbation tensor  $\mathbf{h}$ . The form of these solutions reveal some general properties of gravitational radiation.

## 1.2 Gravitational radiation

Equation 1.5, 1.6, 1.7, 1.8 and 1.9 combine to give a second order differential equation for the perturbation metric.

$$\left(-\frac{\partial^2}{\partial t^2} + \nabla^2\right) \bar{h}^{\mu\nu} = -16\pi T^{\mu\nu} \quad (1.10)$$

where  $\bar{h}^{\mu\nu}$  is called the *trace reverse* of  $h^{\mu\nu}$  and is defined by

$$\bar{h}^{\mu\nu} = h^{\mu\nu} - \frac{1}{2}\eta^{\mu\nu}\eta^{\alpha\beta}h_{\beta\alpha}. \quad (1.11)$$

The solutions to the equation 1.10 are travelling wave solutions which can be written as a superposition of frequency components since small amplitude perturbations obey the superposition principle. The solutions are

$$h^{\alpha\beta} = \frac{A^{\alpha\beta}}{r} \sum_{k,\omega} \exp(k_i x^i - \omega t) = \frac{A^{\alpha\beta}}{r} \sum_k \exp(k_\mu x^\mu). \quad (1.12)$$

Differentiating 1.12 gives

$$\partial_u h^{\alpha\beta} = k_u h^{\alpha\beta} \quad (1.13)$$

From conservation of energy and momentum the stress energy tensor must have zero divergence,

$$\partial_\nu T^{\mu\nu} = 0. \quad (1.14)$$

From equation 1.10 it follows that the perturbation to the metric must also have zero divergence,

$$\partial_\nu h^{\mu\nu} = 0. \quad (1.15)$$

Equation 1.13 together with equation 1.15 require the amplitude of the wave projected along the direction of propagation to be

$$k_\nu h^{\mu\nu} = 0. \quad (1.16)$$

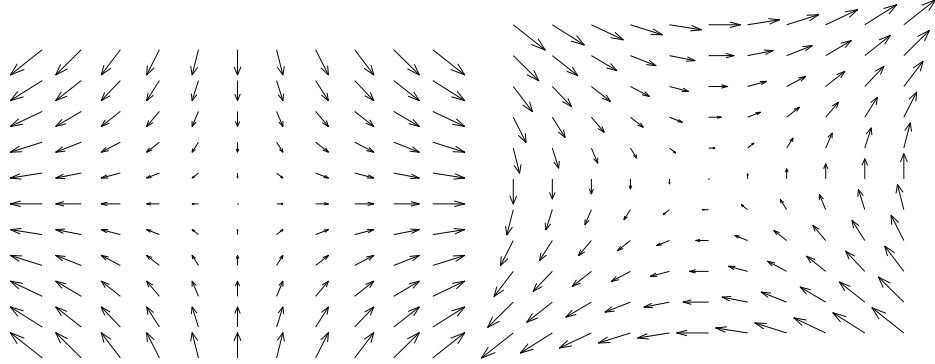


Figure 1.1: The strain field produced by a gravitational wave with + polarization (left) and with  $\times$  polarization (right)

so that the gravitational waves are necessarily transverse to their direction of propagation.

For a gravitational wave propagating in the  $z$ -direction the perturbation to the metric is

$$\bar{\mathbf{h}} = \begin{bmatrix} 0 & 0 & 0 & 0 \\ 0 & h_{xx} & h_{xy} & 0 \\ 0 & h_{yx} & h_{yy} & 0 \\ 0 & 0 & 0 & 0 \end{bmatrix}, \quad (1.17)$$

and has only two independent components,

$$h_+ \equiv h_{xx} = -h_{yy} \quad (1.18)$$

from the tracelessness of  $\bar{h}$  and

$$h_\times \equiv h_{xy} = h_{yx} \quad (1.19)$$

from symmetry. These two components represent the two polarization states of the wave. They represent quadrupolar strain fields oriented at  $45^\circ$  with respect to each other.

Equations 1.12 and 1.17 combine to give a full expression for the perturbation to

the metric:

$$\bar{\mathbf{h}} = \int_{-\infty}^{\infty} \frac{1}{z} \begin{bmatrix} 0 & 0 & 0 & 0 \\ 0 & A_+(\omega) & A_\times(\omega) & 0 \\ 0 & A_\times(\omega) & -A_+(\omega) & 0 \\ 0 & 0 & 0 & 0 \end{bmatrix} \exp\left(\omega\left(t - \frac{z}{c}\right)\right) d\omega. \quad (1.20)$$

This expression reveals two important properties of gravitational radiation: gravitational waves propagate at  $c$ , the speed of light, and are transverse waves with two polarization states,  $+$  polarization and  $\times$  polarization.

### 1.3 Sources of gravitational radiation

A mass distribution with a time varying quadrupole moment will radiate gravitational waves. The Einstein quadrupole formula for gravitational radiation [3], [4] gives a wave amplitude of

$$h_{jk} = \frac{2G}{r c^4} \frac{\partial^2}{\partial t^2} [D_{jk}(t - r/c)]^{TT} \quad (1.21)$$

Where  $[D_{jk}(t - r/c)]^{TT}$  is the transverse traceless projection of the quadrupole moment. Extremely massive objects with very high acceleration (unlike any terrestrial sources) may produce gravitational waves with amplitudes large enough to be detected by earth-based interferometric detectors. These detectors will have sensitivities between  $h = 10^{-20}$  and  $h = 10^{-23}$  above about 10 Hz. (see section 2.1 for a description of sensitivity).

Inspiring binary systems of compact massive objects are relatively efficient radiators of gravitational waves. Black hole pairs radiate strongly enough so that for a  $10^9$  solar mass system at 3 Gpc, the edge of the universe, the wave amplitude at the earth would be  $h \approx 10^{-15}$  as the black holes inspiral, merge then settle. The characteristic frequency of such a system, however, is near  $10^{-5} Hz$  well below the measurement band of earth-based detectors. Lower mass systems have higher characteristic frequencies, but even for the lowest mass black hole systems thought to exist, with a mass of  $10^3$  solar masses, the characteristic frequency would not exceed 10 Hz,

the low frequency cutoff of earth-based detectors.

Neutron star systems produce lower amplitude radiation than black hole systems due to their decreased mass. The frequency of the radiation they produce, however, overlaps better with the 10 Hz to 1 kHz spectrum of earth-based detectors. A neutron star binary system at 3 Gpc produces a wave amplitude of  $h = 10^{-23}$ . As it evolves its center frequency increases from approximately 10 Hz to 1 kHz, covering the band in which earth-based gravitational wave detectors will be most sensitive, making it a strong candidate for detection.

Another interesting source of gravitational radiation is asymmetric supernovae. Supernovae with a radial asymmetry produce gravitational radiation at a range of frequencies above 100 Hz but for likely levels of asymmetry will only be strong enough to be detected if they occur within the milky way galaxy, where supernova events occur on the order of one every one hundred years. Thus it is unlikely that any sources would be visible during the finite lifetime of current detectors.

Binary pulsar systems are of interest because they can be optically observed. Their orbital periods can be measured very accurately using the pulsar period as a comparison. This measurement allows the energy lost due to gravitational radiation to be determined. An indirect measurement of this kind on the binary pulsar PSR 1913+16 remains the only observational evidence of gravitational radiation to date [5][6].

Neutron star binary systems are the most efficient radiator of gravitational radiation in the measurement band of earth-based interferometric detectors. Accordingly the bandwidth and frequency range of interferometric detectors are optimized for the spectrum of radiation they produce. The goal of the advanced interferometric detectors being considered today is a sensitivity of  $h \approx 10^{-23}$  at 100 Hz [35], sufficient to detect a neutron star binary system anywhere in the universe.

## Chapter 2

# Principles of gravitational wave detection

To better understand the design issues of a gravitational wave interferometer it is helpful to have an understanding of the interaction of the gravitational radiation with the interferometer and the interaction of the environment with the interferometer.

To reach the sensitivity goal of an advanced interferometric detector higher power lasers with improved noise characteristics are required, as are suspension systems with better low frequency isolation and core optics with improved mechanical properties compared to what is available for the initial detectors currently being built. An improved interferometer configuration may be necessary to handle the high circulating power without limitations from thermal effects.

Although many interferometer topologies exist which may be able to meet the advanced LIGO sensitivity requirement, each has tradeoffs in the complexity, in risk and in engineering feasibility. To compare different configurations it is useful to consider the interferometer response, noise spectrum, and sensitivity.

### 2.1 Measures of detector performance

The performance of an interferometer is characterized by its response, its noise spectrum and its sensitivity.

The *interferometer response*, or the *frequency response*, is a frequency dependent expression giving the magnitude of the phase difference between the output beams of an interferometer in response to a gravitational wave with unit amplitude (propagating normal to the plane of the interferometer and polarized along the interferometer axes.) Since the gravitational wave magnitude is a unitless strain, the response has units of radians. The interferometer response allows the detection efficiency of different optical configurations to be compared independent of the noise sources that set the absolute sensitivity of the interferometer. The greater the interferometer response at a particular frequency the better the interferometer is able to measure gravitational radiation at that frequency.

The *noise spectrum*, of the interferometer is the power spectral density of phase fluctuations between the interfering beams that would produce an output power spectrum equivalent to the total noise on the output signal – including that due to optical, mechanical, and electronic noise. Unlike the frequency response of the interferometer, the noise spectrum is not only dependent on the optical configuration, but also on the noise levels of many of the detector subsystems such as the laser and suspension systems, as well as the coupling efficiency of the noise into the interferometer.

The *sensitivity* of an interferometer is a combination of the noise level and the response. It is the smallest amplitude wave that can be detected with a given signal to noise ratio (usually 1) as a function of frequency. Many expected signal waveforms are periodic, but most noise sources in the interferometer are not and so can be reduced by time averaging the output signal. A description of the sensitivity of an interferometer must therefore also include the associated measurement interval. Often the dependence on the measurement time is separated from the expression for the sensitivity to give a measurement-interval-independent-sensitivity with units of  $Hz^{-1/2}$ . This is calculated by dividing the total equivalent phase noise of the interferometer by the interferometer response. To determine the actual sensitivity from this, the measurement-interval-independent-sensitivity must be multiplied by the square root of the measurement bandwidth.

These three terms describe the detector performance. The interferometer response

allows different interferometer configurations to be compared directly without concern for engineering feasibility or other practical matters. To compare the feasibility of different configurations it is useful to choose a sensitivity level at a particular frequency and determine what level of noise and noise coupling is necessary to achieve that sensitivity in various interferometer configurations. This allows estimates to be made of the alignment and control requirements for interferometer optics and for the various detector sub-systems.

Before calculating the response of different interferometer configurations, we must understand how gravitational radiation interacts with an interferometer.

## 2.2 Observable effects of gravitational waves

An interferometer measures the phase difference of two or more light beams. Light travels on a null line. That is, for the path of photons,  $\Delta s = 0$ . The interval is related to the metric by equation 1.4 giving

$$ds^2 = -(cdt)^2 + (1 + h_+(r, t))dx^2 + (1 - h_+(r, t))dy^2 + dz^2 = 0 \quad (2.1)$$

when a gravitational wave is propagating in the z-direction. Solving for the effective speed of light travelling in the x-direction gives

$$\frac{dx}{dt} = \sqrt{\frac{c^2}{1 + h_+(r, t)}} \simeq (1 - h_+(r, t)/2)c \quad (2.2)$$

and in the y-direction

$$\frac{dy}{dt} = \sqrt{\frac{c^2}{1 - h_+(r, t)}} \simeq (1 + h_+(r, t)/2)c \quad (2.3)$$

Thus it is acceptable to think of the gravitational radiation as modulating the effective refractive index of the vacuum so that  $n_{eff} = 1 \pm h_+(r, t)/2$ . With this interpretation the gravitational radiation stretches the coordinate system so the mirror coordinates do not change but the distance between them does. For an interferometer aligned to

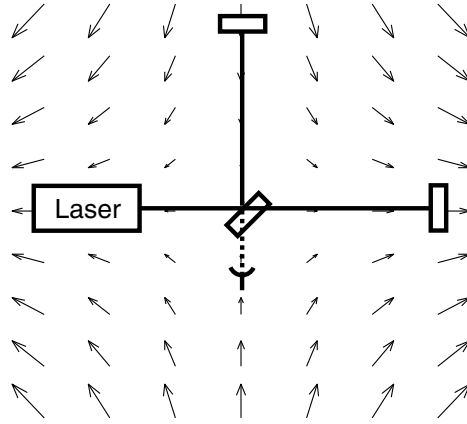


Figure 2.1: The strain field from a gravitational wave acts on the interferometer by effectively shortening the length of one arm while extending the length of the other. For a basic Michelson interferometer, which compares the relative phase of two beams that have travelled in opposite arms of the interferometer, an output signal is produced by the gravitational wave.

the polarization axis of the gravitational wave, as shown in Figure 2.1, the beams will acquire a phase difference due to the gravitational wave modulating the “refractive index” of the vacuum in the arms. We use this analogy to calculate the response of various interferometer configurations.

### 2.2.1 A Michelson interferometer as an antenna for gravitational radiation

A Michelson interferometer compares the phase of two beams that have travelled in different arms of the interferometer, as shown in Figure 2.1. The phase difference between these beams can be calculated using equations 2.2 and 2.3. The phase accumulated by a beam travelling to the end of an interferometer arm of length  $L$  and back is

$$\phi(t) = 2 \int_{t-2L/c}^t \frac{2\pi c}{n_{eff}\lambda} dt \tag{2.4}$$

where  $\lambda$  is the optical wavelength. For a gravitational wave  $h(t)$  with a spectral density  $h(\omega)$  such that

$$h(t) = \int_{-\infty}^{\infty} h(\omega)e^{i\omega t}d\omega \tag{2.5}$$

the phase accumulated in one arm is

$$\phi(t) = \frac{2\pi c}{\lambda} \left( 1 + \int_{-\infty}^{\infty} \frac{h(\omega)}{2\omega} e^{i\omega(t-L/c)} \sin(\omega L/c) d\omega \right) \quad (2.6)$$

and in the other arm is

$$\phi(t) = \frac{2\pi c}{\lambda} \left( 1 - \int_{-\infty}^{\infty} \frac{h(\omega)}{2\omega} e^{i\omega(t-L/c)} \sin(\omega L/c) d\omega \right) \quad (2.7)$$

giving a phase difference of

$$\Delta\phi(t) = \omega_o \int_{-\infty}^{\infty} \frac{h(\omega)}{\omega} e^{i\omega(t-L/c)} \sin(\omega L/c) d\omega \quad (2.8)$$

The absolute value of the spectral density of the phase difference due to a unit magnitude gravitational wave is the response of the Michelson interferometer and is given by

$$\chi_{Michelson}(\omega) = \frac{\omega_o}{\omega} h(\omega) \sin(\omega L/c) \quad (2.9)$$

where  $\omega_o = 2\pi c/\lambda$  is the optical frequency.

Interferometric detector topologies based on the two-arm Michelson interferometer have been extended in a number of ways. For example, power recycling increases the effective power illuminating the interferometer, Fabry-Perot arm cavities increase the effective arm length and signal recycling tailors the storage time of the signal to tune the detector.

## Power Recycling

Power recycling [7][8][9][10] is a technique to increase the effective laser power incident on the beamsplitter of the interferometer. Since only the dark fringe of the interference is detected most of the light returns back towards the laser in the bright fringe. A power recycling mirror, shown in Figure 2.2, between the interferometer and the laser returns light to the interferometer increasing the circulating power. The *power recycling cavity* formed by this mirror and the interferometer must be held on resonance and therefore increases the control system complexity by adding one degree of

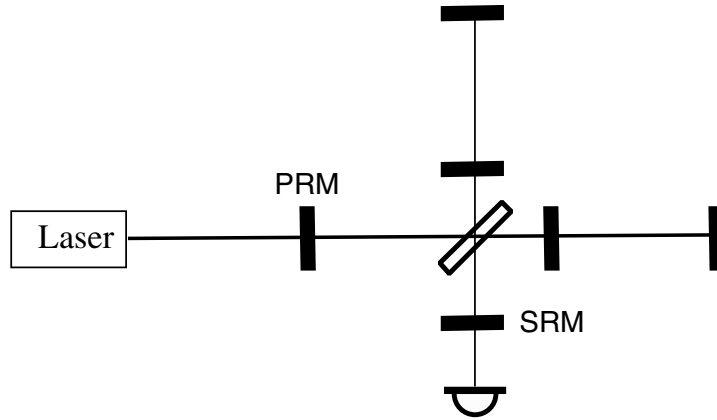


Figure 2.2: The power recycled Fabry-Perot Michelson interferometer. The power recycling cavity is formed by the power recycling mirror (PRM) and the Michelson interferometer. The signal recycling cavity is formed by the signal recycling mirror (SRM) and the Michelson interferometer.

freedom, the power recycling cavity length, which must be controlled. Although it is generally desirable to have a high finesse cavity so that the power recycling factor is large, the power handling capacity of the interferometer optics may limit the finesse of the recycling cavity.

### Fabry-Perot arm cavities

Resonant cavities in the arms of the interferometer increase the storage time or the effective length of the interferometer arms. The finesse of the arm cavities is chosen to set the storage time. For an interferometer without resonant sideband extraction the magnitude of the interferometer response is maximized at frequencies where the storage time is half of the gravitational wave period. When resonant sideband extraction is used, the storage time is made as long as possible to increase the optical power transferred to the extracted sidebands, while the storage time of the signal is set independently by the tuning of the signal recycling cavity.

Although arm cavities allow the peak of the interferometer response to be tuned into the measurement band, they complicate the control system by requiring two additional degrees of freedom to be controlled. Additionally the use of transmissive input

and output coupling mirrors adds two optics through which the circulating power must pass decreasing the thermal power limit of the interferometer (see chapter 6).

### Dual recycling

There are two methods to tailor the bandwidth of the interferometer response using a signal recycling mirror that reflects the signal sidebands back into the interferometer – They are both generically called signal recycling. The first, when used in conjunction with power recycling, is often called dual-recycling [11][12]. A signal recycling mirror, shown in figure 2.2, at the output of the interferometer forms a *signal cavity* that enhances the signal but decreases the bandwidth of the interferometer response. The amount that bandwidth may be traded off against the enhancement factor at the center frequency is a function of the signal cavity finesse and hence of the signal recycling mirror reflectivity. For a simple case of dual recycling one more degree of freedom, the signal cavity length, must be controlled. If two signal recycling mirrors are used to form a tuneable cavity that acts as a variable reflectivity compound signal recycling mirror, two additional degrees of freedom must be controlled.

Signal recycling can be simply described as a form of temporal quasi-phase matching [13]. In the arms of the interferometer the gravitational radiation converts some of the carrier light into signal sidebands which have a frequency difference from the carrier given by the frequency of the gravitational wave. After a time period  $\tau = \frac{1}{2f}$ , the signal and carrier become  $180^\circ$  out-of-phase resulting in the signal being converted back to the carrier. The aim of a dual recycled interferometer is to quasi-phasesmatch the signal and carrier by adding an additional  $180^\circ$  phase shift to the signal in the signal recycling cavity every time the signal and carrier drift out of phase.

### Resonant sideband extraction

Another form of signal recycling which allows the peak-frequency response to be traded off against the bandwidth of the response is *resonant sideband extraction* [14][15][16][17]. Like dual recycling resonant sideband extraction uses a signal recycling mirror at the output of the interferometer. The short compound cavity formed

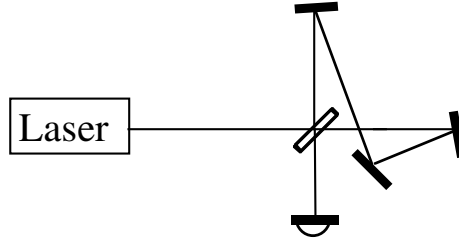


Figure 2.3: a) the basic layout of the Sagnac interferometer. The beamsplitter interferes two beams which have each travelled through *both* arms of the interferometer, but in opposite order.

by the signal recycling mirror and the near mirror of the Fabry-Perot arm cavities is locked on resonance, requiring one additional degree of freedom to be actively controlled. This cavity is only seen by the signal sidebands, since the carrier light interferes destructively at the output port of the interferometer where the signal recycling mirror is located. By tuning the signal cavity near resonance the effective finesse of the Fabry-Perot arm cavities is lowered to near unity for the signal sidebands. This allows the finesse of the arm cavities to be impedance matched for the carrier allowing maximum buildup of stored energy but independently allows the storage time of the signal sidebands to be reduced so that the signal sidebands exit the interferometer before drifting out-of-phase with the carrier.

### 2.2.2 A Sagnac interferometer as an antenna for gravitational radiation

The Sagnac interferometer[18][19][20][21][22] compares the phase of two beams of light that have each travelled in *both* arms of the interferometer, but in the opposite directions. Since they travel along the same path, low-frequency optical path changes do not produce a phase difference. High-frequency optical path changes, with periods comparable to the storage time of the light in the interferometer, *do* produce a phase difference, since the beams are in different arms at different times, and the path changes during that time difference.

The derivation of the phase response of the Sagnac interferometer is similar to

that of the Michelson interferometer in section 2.2.1 but with an additional term accounting for the beams travelling in the opposite arm of the interferometer.

For a gravitational wave polarized along the axis of the interferometer propagating in a direction orthogonal to the plane of the interferometer, the difference in phase accumulated by the light in the counterpropagating beams as they travel through the interferometer is

$$\begin{aligned} \Delta\phi(t) = & \omega_o \int_{t-\tau_{arm}}^t \left(1 + \frac{h_{xx}(t)}{2}\right) dt + \omega_o \int_{t-2\tau_{arm}}^{t-\tau_{arm}} \left(1 + \frac{h_{yy}(t)}{2}\right) dt - \\ & \omega_o \int_{t-\tau_{arm}}^t \left(1 + \frac{h_{yy}(t)}{2}\right) dt - \omega_o \int_{t-2\tau_{arm}}^{t-\tau_{arm}} \left(1 + \frac{h_{xx}(t)}{2}\right) dt \end{aligned} \quad (2.10)$$

where  $\tau_{arm}$  is the storage time of the light in one arm of the interferometer. With  $h_{xx}(t) = -h_{yy}(t) = h_o(t)$  this gives

$$\begin{aligned} \Delta\phi(t) = & \frac{\omega_o}{2} \int_{t-\tau_{arm}}^t h_o(t) dt - \frac{\omega_o}{2} \int_{t-2\tau_{arm}}^{t-\tau_{arm}} h_o(t) dt + \\ & \frac{\omega_o}{2} \int_{t-\tau_{arm}}^t h_o(t) dt - \frac{\omega_o}{2} \int_{t-2\tau_{arm}}^{t-\tau_{arm}} h_o(t) dt. \end{aligned} \quad (2.11)$$

Taking the Laplace transform of each side gives the relationship as a function of frequency

$$\begin{aligned} \Delta\phi(\omega) = & \frac{\omega_o}{\omega} h_o(\omega) - \frac{\omega_o}{\omega} h_o(\omega) e^{-i\omega\tau_{arm}} - \\ & \frac{\omega_o}{\omega} h_o(\omega) e^{-i\omega\tau_{arm}} + \frac{\omega_o}{\omega} h_o(\omega) e^{-2i\omega\tau_{arm}}. \end{aligned} \quad (2.12)$$

or

$$\Delta\phi(\omega) = -4 \frac{\omega_o}{\omega} e^{-i\omega\tau_{arm}} \sin^2(\omega\tau_{arm}/2) h_o(\omega) \quad (2.13)$$

Dividing both sides by  $h_o(\omega)$  and taking the absolute value gives the frequency response

$$\chi(\omega) = 4 \frac{\omega_o}{\omega} \sin^2 \omega\tau_{arm}/2 \quad (2.14)$$

Figure 2.2.2 shows the response of the Sagnac and the Michelson interferometer.

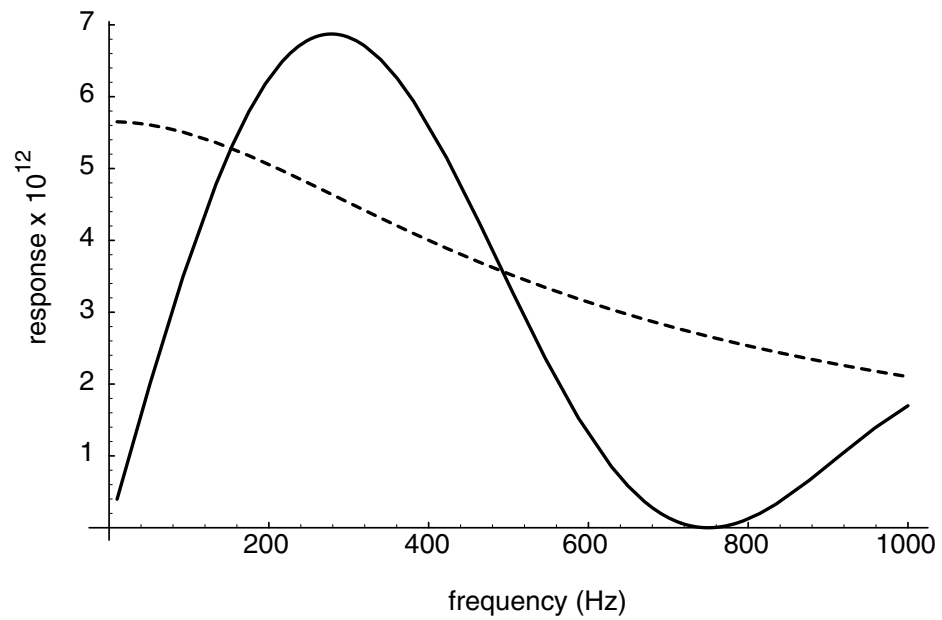


Figure 2.4: The response of a 4 km arm length, 50-bounce delay-line Sagnac interferometer (solid curve) and a 4 km arm length Fabry-Perot Michelson interferometer with a cavity buildup of 50 (dashed curve). The response is in radians per unit strain. The wavelength of the illuminating laser is assumed to be 532 nm.

The frequency response of the Sagnac interferometer is, unlike the Michelson interferometer, zero at zero-frequency. This has a dramatic impact on the design and control requirements for the laser and optics of the Sagnac. The interferometer is passively locked to a dark fringe, even in the presence of slow laser frequency drift or drift in the mirror position, eliminating the need for complex servo loops like those used to control the recycled Fabry-Perot Michelson interferometer. Although arm cavities and recycling configurations can be used to extend the Sagnac interferometer as well as the Michelson, they introduce a response at zero-frequency complicating the control of the Sagnac interferometer and eliminating the interferometer's insensitivity to quasi-static effects, such as thermally induced deformation of the optics. For this reason we consider a Sagnac interferometer that lacks resonant cavities altogether allowing the interferometer control scheme to be kept as simple as possible and removing many of the restrictions that resonant cavities place on the interferometer design such as laser frequency stability and the optical quality of the core substrates in transmission. A Sagnac interferometer must differ from an enhanced Michelson interferometer in several ways to meet the desired sensitivity level of LIGO III without using resonant cavities.

To illuminate the Sagnac interferometer near the optimum power level, a high power laser source is necessary. Although the power level of the laser must be nearly two orders of magnitude larger than for the power recycled Michelson interferometer, the frequency stability of the laser is less critical.

Optical delay lines in the interferometer arms are an alternative to Fabry-Perot cavities to increase the storage time of the light in the interferometer. Delay lines require large optics to accommodate the many beam spots and also require that light scattered from the delay line mirrors be controlled so that the phase noise produced when that light scatters back into the main beam does not limit the interferometer sensitivity. Additionally the interferometer must be operated like the Michelson interferometer, in a manner that uses the beamsplitter in a symmetrical fashion so that the fringe contrast is maximized. These challenges are addressed by the polarization Sagnac interferometer design presented in chapter 3.

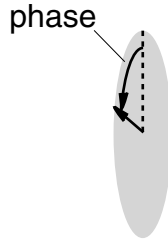


Figure 2.5: The phasor representation of a single frequency wave. The phasor is a vector whose magnitude and phase give the amplitude and phase of the wave it represents.

Regardless of the particular interferometer configuration, the gravitational radiation produces phase modulation sidebands on the light in the interferometer that must be detected. Because gravitational wave amplitudes are quite small, however, the modulation produced is very weak. It is therefore necessary to understand how to efficiently extract and detect the modulation sidebands that are produced in the interferometer.

### 2.3 Detection of signal sidebands

A gravitational wave produces modulation sidebands on the light in the interferometer. Information can be extracted from these sidebands in a number of ways, all involving the detection of a beat between the sidebands and another frequency component of the light. To describe three common detection schemes, detection on the side of a fringe, homodyne detection, and heterodyne detection, it is useful to consider the phasor model of light in a rotating frame[23]. In the phasor picture, shown in Figure 2.5, each frequency component of the light is represented as a vector. The magnitude and phase of the vector represent the amplitude and phase of the wave that it represents. The frequency components of the waveform are separated and plotted on the frequency axis. The vector rotates at its optical frequency. We can compare relative phases of different frequency components most easily by transforming to a reference frame rotating at the center optical frequency. The phasor at this frequency is stationary while phasors of higher frequency components continue to rotate forward

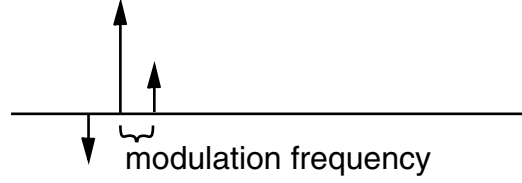


Figure 2.6: The phasor representation of a phase modulated wave with the carrier (center arrow) and the two phase modulation sidebands (outside arrows)

and phasors with lower frequencies rotate backwards at the difference frequency.

Phase modulation is represented by a carrier with two sidebands spaced on either side by the modulation frequency, as shown in Figure 2.6. When viewed in the rotating frame of the carrier, the sidebands rotate at the modulation frequency, and are  $180^\circ$  out of phase when they are aligned with the carrier phasor. Each sideband beats with the carrier, but the beat signal from each is  $180^\circ$  out of phase. The result is that the beating amplitudes cancel out and only the phase of the resultant light field is modulated. The detected intensity is given by

$$\begin{aligned}
 I_{\text{det}} = & \frac{1}{2\eta} \cdot \left( E_{\text{car}}^2 + 2E_{\text{car}}E_+ \cos\left(\omega t + \frac{\pi}{2}\right) \right. \\
 & \left. + 2E_{\text{car}}E_- \cos\left(-\omega t + \frac{\pi}{2}\right) + E_+^2 + E_-^2 \right) \quad (2.15)
 \end{aligned}$$

where  $\eta = 377\Omega$  is the impedance of free space,  $E_{\text{car}}$  is the magnitude of the carrier fields and  $E_+$  and  $E_-$  are the magnitudes of the upper and lower sidebands respectively.

Amplitude modulation is represented by a carrier with two sidebands spaced on either side of the carrier by the modulation frequency. When viewed in the rotating frame of the carrier the sidebands rotate at the modulation frequency and are in phase when they are aligned with the carrier phasor. Both sidebands beat with the carrier in phase. The result is addition of the beats producing an amplitude modulated intensity.

$$I_{\text{det}} = \frac{1}{2\eta} \cdot \left( E_{\text{car}}^2 + 2E_{\text{car}}E_+ \cos(\omega t) + 2E_{\text{car}}E_- \cos(-\omega t) + E_+^2 + E_-^2 \right) \quad (2.16)$$

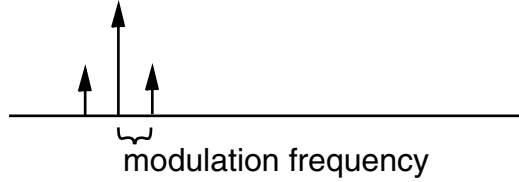


Figure 2.7: The phasor representation of an amplitude modulated wave with the carrier (center arrow) and the two amplitude modulation sidebands (outside arrows)

Since optical detectors are square law detectors, they measure the intensity of the light, not the electric field amplitude, so the phase difference between the two beams of the light cannot be directly measured. To extract information contained in the phase difference of the beams, it is necessary to convert the phase modulation into amplitude modulation. The conventional way to do this is to bias the output of the interferometer to the side of a fringe so that the phase difference is converted to an amplitude level by the interferometer. The measured intensity is then

$$I_{det} = \frac{1}{4\eta} (E_0^2 - E_0^2 \sin(\Delta\phi)) \tag{2.17}$$

where  $\Delta\phi$  is the differential phase and  $E_0$  is the electric field amplitude of the beam illuminating the interferometer. In the phasor picture this amounts to setting a  $90^\circ$  phase offset between the carrier frequencies of the interfering beams. The phase between the sidebands of the two interfering beams is then also  $90^\circ$ . The beamsplitter acts to separate the components along  $\pm 45^\circ$ . The projection of the sidebands at  $45^\circ$  are in phase and the result is amplitude modulation. Only half of the carrier light and half of the sidebands exit each port of the beamsplitter so detection of the signal on both ports is necessary to maximize the signal.

Since the power level of the carrier light is too high for the photodetectors, it is necessary to bias the interferometer to a dark fringe and use an external local oscillator to detect the sidebands. By creating a 180 degrees phase offset between the carriers of the interfering beams, the carriers add destructively when recombined but the sidebands add constructively. If only the signal sidebands are detected the detected amplitude modulation is due to the beating of the two sidebands. These

sideband amplitudes are proportional to the modulation depth but the intensity of their beat signal is only proportional to the square of the modulation depth, which makes detection of small signals difficult. To improve the extraction efficiency a local oscillator is used, an external field which beats against both sidebands, to produce a signal with an intensity directly proportional to the modulation depth.

### 2.3.1 Optical homodyne detection

In homodyne detection the local oscillator has the same frequency as the carrier field. The local oscillator phase is adjusted to be at  $90^\circ$  with respect to the carrier so that the sidebands beat in phase with the local oscillator to produce amplitude modulation. This gives a measured intensity

$$I_{det} = \frac{1}{2\eta} \left( E_{lo}^2 - E_0^2 \sin^2(\Delta\phi) + 2E_0 E_{lo} \sin(\Delta\phi) \right) \quad (2.18)$$

where the third term provides the useful signal. In this way the signal is linear just as it was when biasing the interferometer to the side of a fringe. The light power on the photodetector is controllable, however, and is set by the power of the local oscillator, independent of the magnitude of the power illuminating the interferometer.

### 2.3.2 Optical heterodyne detection

In heterodyne detection a local oscillator is used just as it was in homodyne detection, however the frequency of the local oscillator is shifted from that of the carrier by the RF heterodyne frequency. This gives a measured intensity of

$$I_{det} = \frac{1}{2\eta} \left( E_{lo}^2 - E_0^2 \sin^2(\Delta\phi) + 2E_0 E_{lo} \sin(\Delta\phi + \omega_r ft) \right). \quad (2.19)$$

The output photocurrent is amplitude modulated at the heterodyne frequency. The photocurrent can be mixed with an electronic signal at the heterodyne frequency to convert the signal back to the original frequency. This is useful in situations where the noise level of the laser is too high at the signal frequency but is quieter around the heterodyne frequency.

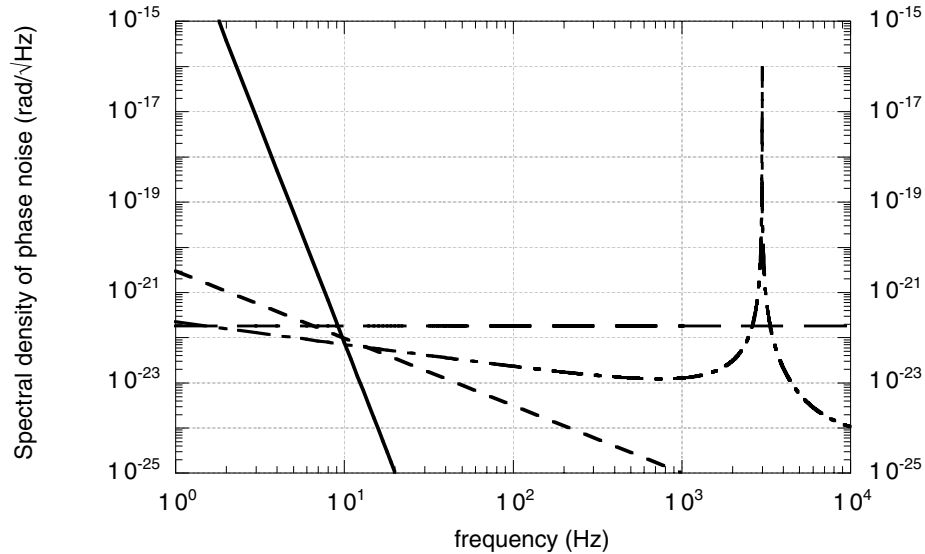


Figure 2.8: The spectrum of various noise sources in an interferometric gravitational wave detector. Seismic noise (solid curve), shot noise (large dashes), radiation pressure (small dashes), and thermal noise (dashed-dotted curve) are shown.

## 2.4 Understanding measurement noise

With an understanding of how signals from gravitational radiation are detected, it is necessary to consider the sources of noise that limit sensitivity to those signals. Of the many possible noise sources, three are expected to limit the interferometer sensitivity in different frequency regions: seismic noise at low frequencies, thermal noise at intermediate frequencies and shot noise at high frequencies. The strength of the coupling of these noise sources into the photocurrent signal depends on the interferometer configuration. Thus different interferometer configurations have different operating tolerances. Understanding these tolerances allows us to choose the interferometer configuration that yields the best signal to noise ratio in a given environment.

### 2.4.1 Seismic noise

At low frequencies, below 10 Hz, the coupling of seismic noise into the position of the interferometer test masses limits the interferometer sensitivity [24]. The coupling is

reduced by a complex seismic isolation system that reduces the seismic noise induced motion of the test masses at high frequencies. Figure 2.8 shows that below about 10 Hz the motion of the mirrors produces modulation on the beams that is indistinguishable from that produced by gravitational radiation and is the dominant noise source.

### 2.4.2 Thermal noise

Between 10 Hz and 100 Hz the internal thermal noise of the test masses is expected to be the limiting noise source [25][26][27][28]. Thermally excited modes of vibration of the test masses cause the reflecting surface of the masses to move. The fluctuations in the position of these surfaces imposes a modulation on the light which is indistinguishable from the modulation produced by gravitational radiation. Materials with low mechanical loss are being used for the test masses so that the thermal energy is efficiently stored in a few modes of vibration which have large amplitude but are at frequencies outside of the measurement band, as shown in Figure 2.8. The off-resonant noise is then reduced. The choice of materials, however, is constrained by the need for materials with excellent optical properties as well as cost considerations, size, and availability.

### 2.4.3 Quantum Noise

The quantization of light energy adds noise to the measurement in two different ways[29]. The statistical variation in the number of photons in a measurement interval at the detector is called shot noise and is important at low power levels [30], [31]. The statistical variation of the mirror position produced by the statistical variation in the radiation pressure on the mirrors is called radiation pressure noise and is important at high power levels [32]. The sum of these noise sources is quantum noise, which can be reduced to the *standard quantum limit* when the power is optimized so that the shot noise and radiation pressure noise are equal.

The shot noise power increases as the square root of the number of photons,  $n$ ,

illuminating the beamsplitter in a measurement interval  $\Delta t$ ,

$$\frac{P_{sn}}{P_o} = \frac{1}{\sqrt{n}} \quad (2.20)$$

where

$$n = \frac{P_o \Delta t}{\hbar \omega_o}. \quad (2.21)$$

Here  $\hbar$  is Plank's constant and  $\omega_o$  is the frequency of the light. Since shot noise is white noise the shot noise power spectral density is given by

$$\tilde{P}_{sn} = 2\sqrt{\frac{\pi \hbar c P_o}{\lambda}} Hz^{-1/2}. \quad (2.22)$$

The shot noise power spectral density leads to a phase noise spectral density

$$\tilde{\phi}_{sn} = 2\sqrt{\frac{\pi \hbar c}{\lambda P_o}} rad Hz^{-1/2}. \quad (2.23)$$

Since the interferometer signal increases linearly with the circulating power, but the shot noise power increases as the square root of the circulating power, the shot noise limited signal to noise may be improved by increasing the optical power in the interferometer. At very high circulating power, however, radiation pressure noise limits the interferometer sensitivity. The momentum imparted to the mirrors is given by

$$p_{sn} = \frac{4\pi}{\lambda} \hbar N n \quad (2.24)$$

where  $N$  is the number of beam reflections on the mirror (which may be greater than 1 if the mirror is part of a delay line or Fabry-Perot cavity) and  $\frac{4\pi}{\lambda} \hbar$  is the momentum recoil of a single photon. The radiation pressure is subject to the statistical variations in the number of photons illuminating the mirror, so that the imparted momentum is given by

$$p_{sn} = \frac{4\pi N \hbar}{\lambda} \sqrt{n} = \frac{4\pi N \hbar}{\lambda} \sqrt{\frac{P \Delta t \lambda}{hc}}. \quad (2.25)$$

The displacement noise produced by the momentum fluctuations can be found by

relating the imparted momentum to the change in velocity of the mirror,

$$\Delta p = m\Delta v = m\frac{\Delta x}{\Delta t}. \quad (2.26)$$

With the measurement interval related to the bandwidth of the measurement by  $\Delta t = \frac{1}{2f}$  the spectral density of displacement noise of the mirror becomes

$$\Delta\tilde{x}_{rp}(f) = \frac{1}{mf^2}\sqrt{\frac{\pi\hbar NP}{\lambda c}}mHz^{-1/2}. \quad (2.27)$$

This produces a power spectral density of phase noise given by

$$\tilde{\phi}_{rp}(f) = k\Delta\tilde{x}_{rp} = \frac{2\pi}{m\lambda f^2}\sqrt{\frac{\pi\hbar NP}{\lambda c}}mHz^{-1/2}. \quad (2.28)$$

The sum of the shot noise of equation 2.23 and the radiation pressure noise of equation 2.28 give the total quantum noise which can be minimized to the standard quantum limit, given by

$$\tilde{\phi}_{sql} = \frac{4\pi}{\lambda f}\sqrt{\frac{N\hbar}{m}}radHz^{-1/2}, \quad (2.29)$$

when the interferometer is illuminated with the optimal power for the frequency being measured

$$P_{opt} = \frac{c\lambda mf^2}{\pi\sqrt{N}}. \quad (2.30)$$

#### 2.4.4 Other noise sources

It is expected that seismic noise, thermal noise, and quantum noise will limit the noise floor of advanced LIGO detectors. All other noise sources must be suppressed well below these levels. These other noise sources include noise derived from the Sagnac effect, laser intensity noise, laser frequency noise and mirror orientation noise. The level to which these noise sources affect the measured photocurrent is highly dependent on the interferometer configuration. The required tolerances for these parameters is calculated for the Sagnac interferometer in chapter 5.

## 2.5 The LIGO project

The National Science Foundation has funded the construction of a gravitational wave observatory with two sites in the United States housing a total of three interferometric receivers for gravitational wave detection [33][34][35][36]. Completion of the first generation Laser Interferometric Gravitational Wave Observatory (LIGO I) is scheduled for 2002. LIGO I receivers are Michelson interferometers with Fabry-Perot cavities in the arms to increase the storage time of the light. Future upgrades to the detector are planned in 2006 (LIGO II) and 2010 (LIGO III) to improve sensitivity. The LIGO interferometric receivers are housed in 4 km-long 1 m diameter vacuum tubes. Long interferometer arms are desirable for maximum strain sensitivity. However, the practical length that can be constructed on the surface of the earth is a few kilometers. Beyond this length the curvature of the earth causes the vertical suspensions of the near and far mirror to deviate sufficiently from parallel so that the coupling of noise from vertical motion of the pendulums to the longitudinal direction limits the interferometer's sensitivity.

## 2.6 Other Gravitational Wave Observatories

In addition to LIGO several other gravitational wave observatories are proposed or are being constructed around the world. The existence of multiple gravitational wave detectors not only allows for measurement correlation for improved detection confidence, but also allows the location of the source to be determined by triangulation.

- GEO 600[37] is a 600 m interferometer that has been constructed in Ruthe Germany as part of a German-Scottish collaboration. GEO increases the effective arm length of the interferometer by double-passing the arms. The sensitivity of the detector is maximized for a narrow band of frequencies by using signal recycling.
- VIRGO[38] is a 3 km interferometer being constructed outside of Pisa, Italy by a French-Italian collaboration.

- ACIGA[39][40][41] is a proposed 500 m interferometer to be built near Perth in Western Australia. Dual-recycling is planned to increase the sensitivity of the interferometer. The observatory may be upgraded with future expansions to increase the length up to 5 km. ACIGA will be the only southern hemisphere detector.
- TAMA[42][43][44] is a 300 m interferometer in Tokyo. It is a prototype for an eventual 3 km interferometer to be built at an undetermined location.

All of these interferometers use L-shaped interferometers with various methods to increase the energy stored, or the effective length of the arms. The different configurations make different tradeoffs between complexity, sensitivity and measurement bandwidth. Although each observatory will be optimized for different bandwidths and center frequencies, collectively the observatories will allow coincidence detection, full sky coverage and source triangulation.

The polarization Sagnac interferometer discussed in this thesis is for consideration in an advanced LIGO detector. As such it should have good sensitivity near  $h \leq 10^{-23} Hz^{-1/2}$  from 10 Hz to 1 kHz and its beams should fit within the 1 m clear aperture of the vacuum tubes. Figure 2.9 shows the desired sensitivity curve for an advanced LIGO detector compared to the sensitivity curves for LIGO I and LIGO II.

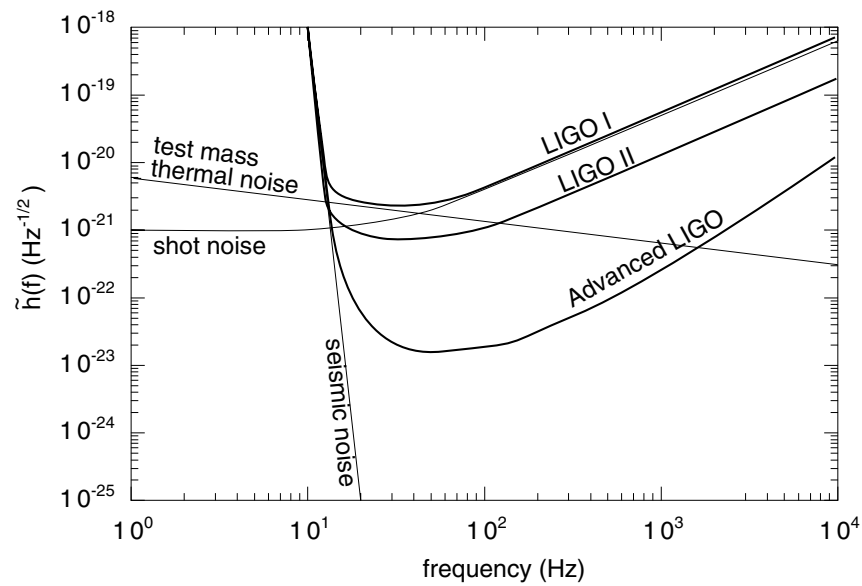


Figure 2.9: Sensitivity curves for LIGO I, LIGO II and an advanced LIGO detector. The limiting noise sources for LIGO I are also shown. The advanced LIGO sensitivity curve is only a reference. The exact shape of the sensitivity curve is dependent on the specific interferometer configuration.

## Chapter 3

# The Polarization Sagnac Interferometer

The performance of early interferometer designs for gravitational wave detection was limited by the available laser power. This led to the development of recycling techniques using resonant cavities to use the available power more efficiently. As high power lasers become available, however, thermal distortions will limit circulating power. In this thermally limited regime it is undesirable to use resonant cavities, as thermally induced distortions may drive the cavities unstable. Interferometer configurations for advanced gravitational wave detectors may bear little resemblance to those used in first generation detectors.

The ideal characteristics of a laser interferometer for gravitational wave detection are numerous and are not likely to be simultaneously achievable in any single design. Among the desirable characteristics are a high in-band signal response, little transfer of in-band environmental and technical noise to the output signal, insensitivity to out-of-band noise to minimize the necessary control effort, robust operation so the interferometer has little down-time, and a well understood behavior.

A common-path interferometer, such as the Sagnac, is well suited to gravitational wave detection because it inherently exhibits many desirable characteristics. It can be operated with few or no transmissive optics and no resonant cavities giving it excellent power handling capabilities. By interfering two beams which have travelled identical

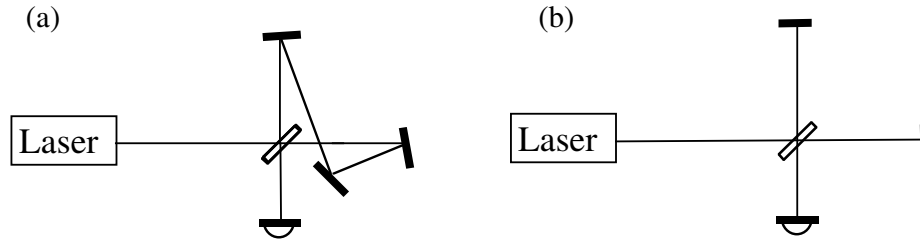


Figure 3.1: a) the basic layout of the Sagnac interferometer has the interfering beams travelling in opposite directions around a loop which includes both arms of the detector. b) the Michelson interferometer separates the interfering beams with one beam in each arm of the detector.

paths, the signal is virtually insensitive to any common-mode noise source. This means the tolerances on the laser amplitude and frequency stability for example can be eased allowing more freedom in engineering the high-powered laser. By nature of the common optical path, the Sagnac is passively locked and has no sensitivity to the slow movement of the interferometer mirrors. This eliminates the need for large dynamic range actuators to keep the interferometer locked while tidal forces and other large-amplitude low-frequency forces strain the earth under the interferometer. Thus the control effort can be focused on the spectral region where it counts – controlling the *in-band* motion of the core optics. Passive locking of a common-path interferometer is extremely robust making down time unlikely, a feature that has led it to be used in other devices that require good sensitivity in noisy environments.

The Sagnac interferometer has long been used in fiber-gyroscopes for high sensitivity rotation sensing [45]. The reciprocal nature of the fiber-Sagnac allows detection on the bright fringe of the interference, which is virtually insensitive to noise from any components of the interferometer due to their reciprocal action on the two interfering beams, as described in section 3.1.3.

By using polarization control in the Sagnac interferometer the detection of a signal can be made on the dark fringe of the interference while still maintaining the reciprocal nature of the interferometer. This configuration retains the excellent noise rejection from reciprocity and simultaneously allows for very high power illumination without saturating the detector. Delay lines in the arms of the interferometer increase the

storage time to improve the interferometer response to signals in the frequency band of interest without the control requirements or thermally induced stability problems of resonant cavities. These modifications to the simple Sagnac interferometer form a foundation that allows it to meet all of the desirable characteristics outlined above, with perhaps the exception of being well understood. In this chapter I describe in detail the polarization Sagnac interferometer so that it may be better understood by the reader and present a 2 m tabletop interferometer based on this design. Chapter 6 extends this design by eliminating transmissive optics, and contains results from a 10 m all-reflective polarization Sagnac interferometer with suspended optics.

### 3.1 Interferometer Topology

The basic Sagnac interferometer consists of a beamsplitter which separates the input into two beams that counterpropagate around a loop. For a gravitational wave detector this loop is arranged to have two orthogonal arms. The light travels through one arm of the interferometer and then is sent into the other arm before being recombined at the beamsplitter with a beam that travelled the same path but in the opposite direction. The maximum response can be found by maximizing equation 2.14. The peak response occurs when the storage time of the interferometer is nearly equal to the period of the gravitational wave signal being detected. The frequency of the peak response is found by solving the transcendental equation

$$\omega\tau_{int} = 2 \tan(\omega\tau_{int}/4). \quad (3.1)$$

While the Sagnac interferometer has a peak response to signals at a frequency nearly equal to the inverse of the transit time for the beams around the loop, the zero frequency phase accumulated by the counterpropagating beams is identical, so the interference condition is not a function of the path length or the position of any of the mirrors as it is in the Michelson or the Fabry-Perot interferometer.

The interference contrast can be excellent if the interferometer is operated in a reciprocal configuration. That requires the detection be done on the reciprocal

port of the beamsplitter. For an amplitude splitting beamsplitter with reflected and transmitted fields that obey

$$E_r = rE_o, \quad E_t = itE_o, \quad (3.2)$$

for a suitable choice of reference planes, the output at the dark, non-reciprocal port is given by

$$E_d = (r^2 - t^2)E_o \quad (3.3)$$

and at the bright, reciprocal port by

$$E_b = (rt - tr)E_o. \quad (3.4)$$

We call the port of the beamsplitter where destructive interference occurs the non-reciprocal port due to the way the beamsplitter acts differently on the two interfering beams, reflecting one twice but transmitting the other twice. The residual intensity at the dark fringe due to any asymmetry in the beamsplitting ratio reduces the fringe contrast, resulting in excess power on the photodiodes and decreasing the sensitivity of the measurement. Operation of the interferometer in a fully reciprocal configuration (see section 3.1.3) with detection at the reciprocal port of the beamsplitter, a spatial filter at the input and output of the interferometer, polarization analysis and a signal readout scheme, eliminates any bias on the signal that would result in excess power on the detector or would couple dynamic effects in the interferometer to noise at the output.

Noise introduced by in-band motion of the core optics couples to the output signal through the asymmetry in the optic's position in the interferometer's optical path. For example, motion of a mirror at the half-way point of the interferometer loop does not produce noise on the output as the phase fluctuations it introduces onto the counterpropagating beams arrive at the beamsplitter simultaneously and cancel when the destructive interference condition is met. For an optic with a path length asymmetry of  $2\Delta L$ , meaning it is a distance  $\Delta L$  away from this symmetry point, the correlation of the phase fluctuations it induces on one beam to the differential phase

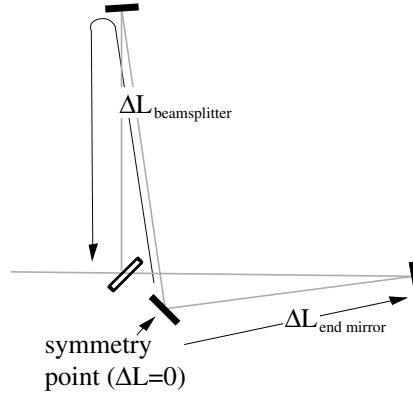


Figure 3.2: The asymmetry of an optic in the Sagnac loop is the optical path length between it and the half-way point of the loop. Any information imposed on the beams at a point with an asymmetry of  $\Delta L$  will arrive at the photodetector with a relative propagation delay of  $2\Delta L/c$  between the two beams.

of the interfering beams at the output is

$$\phi_{out}(\omega) = \sin \frac{4\pi\Delta L\omega}{c} \phi(\omega) \quad (3.5)$$

Figure 3.2 shows the point of zero asymmetry, the asymmetry length of an end mirror and of the beamsplitter. From equation 3.5 the Sagnac interferometer is most sensitive to noise from the beamsplitter, which has a maximum asymmetry length, and other optical components near the beamsplitter in the optical path.

### 3.1.1 The need for delay lines in the interferometer arms

The need for the gravitational wave detector to have good signal response in the measurement band requires the storage time of the light in the interferometer be comparable to the period of in-band signals. For detection between 10 Hz and 1 kHz it is desirable to have the storage time between 1 ms and 100 ms. This requires a total optical path length of several thousand kilometers. While it is impractical to make vacuum tubes for an interferometer of this dimension, it is possible to fold the optical path many times inside a shorter vacuum tube to achieve the desired storage time.

The beam path may either be folded into a delay line so that it makes a number of passes along discrete paths between the folding mirrors or a Fabry-Perot cavity so that all of the folded beam collapse to a single path. For an ideal delay-line every ray travels the same distance along the folded path before exiting the delay line. For a Fabry-Perot the output is composed of waves which travelled different numbers of times between the mirrors before being transmitted. Only the delay-line maintains the common path nature of the Sagnac interferometer and the advantages that common-path interferometry entail. Experimental investigations at the Australia National University of the Sagnac interferometer with cavities in the arms support this conclusion [46].

Another feature of delay lines in a Sagnac interferometer is that the noise caused by the Sagnac effect, which couples in through the area enclosed by the beams in the delay line, cancels out reducing the interferometer's response to the rotation of the earth. In a zero-area configuration with delay lines in the arms the response to earth rotation does not limit the sensitivity of the interferometer.

### 3.1.2 Zero-area Sagnac as a common path interferometer

Fiber-Sagnac interferometers are traditionally used for rotation sensing. Rotation of the interferometer affects the phases of the two counterpropagating beams differently [47]. The differential phase accumulated after propagating around the loop due to the Sagnac effect is

$$\Delta\phi = 8\pi \frac{\mathbf{A} \cdot \boldsymbol{\Omega}}{c\lambda}. \quad (3.6)$$

where  $\mathbf{A}$  is the vector representing the area enclosed by the interferometer loop and  $\boldsymbol{\Omega}$  is the vector representing the rotation of the interferometer. For a gravitational wave detector it is desirable to minimize the sensitivity to the rotation of the interferometer. The phase noise due to rotation is

$$\tilde{\phi}(\omega) = 8\pi \frac{\mathbf{A}}{c\lambda} \tilde{\boldsymbol{\Omega}}(\omega) + 8\pi \frac{\boldsymbol{\Omega}}{c\lambda} \tilde{\mathbf{A}}(\omega). \quad (3.7)$$

For rotation of the earth,  $\Omega = 7.27 \times 10^{-5} \text{ rad/s}$  and  $d\Omega(\omega) \approx 10^{-8}\Omega$ , [48] which constrains  $A$  and  $\tilde{A}(\omega)$ . It has been suggested by Sun [22] that the constraint on the maximum area enclosed by the interferometer can be met by folding the interferometer loop into two arms that enclose equal, but opposite area. Although this configuration encloses no net area, it splits the loop into two subloops which each couple in noise that only cancels at zero frequency. When the phase due to the Sagnac effect in each beam subtracts, the *noise* from the Sagnac effect is only reduced by a frequency dependent term, not eliminated. For example the power spectral density of phase noise due to the Sagnac effect in *one* arm of the interferometer  $\tilde{\phi}_{arm}(\omega)$ , combines with equal magnitude noise from the other arm of the interferometer to produce a power spectral density of the interferometer's output phase difference of

$$\tilde{\phi}_{out}(\omega) = \frac{\sin(\tau_{arm}\omega/2)}{\tau_{arm}\omega} \tilde{\phi}_{arm}(\omega) \quad (3.8)$$

where  $\tau_{arm}$  is the storage time of the light in each arm of the interferometer. If the path of the light is arranged so that it forms  $n$  closed loops when projected onto the plane of rotation, each successive loop enclosing equal area but of alternating sign as the previous loop, an approximation appropriate for an  $n$ -bounce delay line, then equation 3.8 can be generalized to give

$$\tilde{\phi}_{out}(\omega) = \frac{\sin^n(\tau_{loop}\omega/2)}{\tau_{loop}\omega} \tilde{\phi}_{loop}(\omega) \quad (3.9)$$

where  $\tau_{loop}$  is the storage time of the light in each of the  $n$  loops of the arm. Equation 3.7 for phase noise due to the Sagnac effect in each loop combines with equation 3.9 for the phase noise for all  $n$  loops to give the total phase noise due to the Sagnac effect in an  $n$ -bounce delay line Sagnac,

$$\tilde{\phi}_{out}(\omega) = \frac{8\pi}{c\lambda} (A_{loop}\tilde{\Omega}(\omega) + \Omega\tilde{A}_{loop}(\omega)) \frac{\sin^n(\tau_{loop}\omega/2)}{\tau_{loop}\omega}. \quad (3.10)$$

At frequencies where  $\sin^n(\tau_{loop}\omega/2)$  is of order unity a tight constraint is imposed on the area enclosed by the loops and the mirror orientation stability necessary to

control the fluctuations. These frequencies, however, are approximately  $n$ -times larger than the frequency of the measurement band. At frequencies in the measurement band,  $\omega \approx \frac{\pi}{n\tau_{loop}}$  and  $\sin(\omega\tau_{loop}) \approx \omega\tau_{loop}$ , so  $\sin^n(\tau_{sl}\omega/2) \approx (\pi/2n)^n$ , which for an interferometer with even only a few folds of the interferometer arm reduce the constraints on  $A$  and  $\tilde{A}(\omega)$  to the level where they are not of concern. Thus it stands that the Sagnac effect can be neglected in a zero-area Sagnac interferometer with delay lines in the arms.

### 3.1.3 Using the Sagnac in a Reciprocal Configuration

While it is necessary to detect at the dark fringe of interference to avoid saturating the photodetectors with high circulating power, it is also desirable to detect on the reciprocal port of the beamsplitter where any beamsplitter asymmetry does not degrade the sensitivity of the interferometer. Four basic elements are required for full reciprocal operation of the interferometer without any noise coupling from any optics to first order. Figure 3.3 illustrates these four requirements; detection at the reciprocal port of the beamsplitter, an input and output spatial filter, an input polarizer and output analyzer, and a signal extraction scheme. These elements are described in the following four paragraphs.

First detection on the reciprocal port of the beamsplitter is necessary so that the beamsplitter is used symmetrically. The reciprocal port of a Sagnac beamsplitter is the same as the input port of the interferometer. It is therefore necessary to pick off an output beam which is propagating back towards the laser. By using polarization control, as is described in section 3.2, the polarization Sagnac allows the output beam to be selected with a polarizing beamsplitter ( $PBS_1$ ).

Secondly, a spatial filter at the input and output is necessary to assure that the detected spatial mode is the same as the spatial mode injected into the interferometer. By achieving optimal mode overlap of the input and output beams, any process, such as scattering at optical surfaces that converts light into other spatial modes, only removes light from the interferometer without changing the bias point of the interference or introducing spurious signals. In the polarization Sagnac interferometer, the

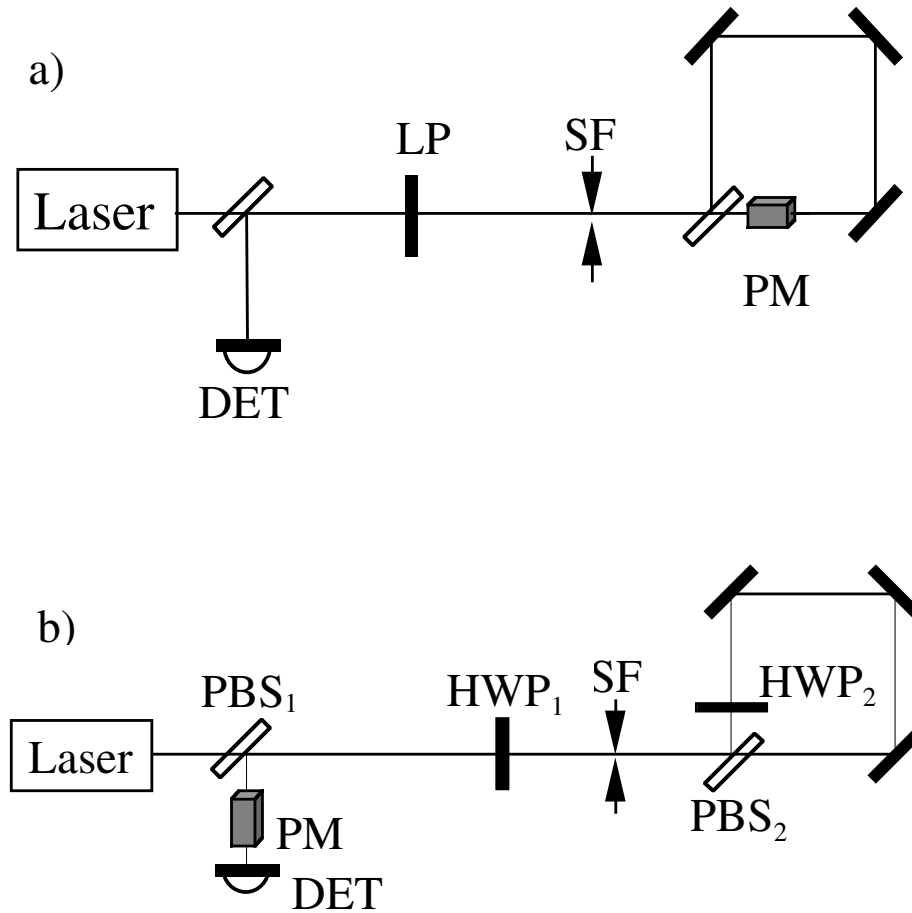


Figure 3.3: a) The minimum reciprocal configuration for the Sagnac interferometer with detection on the bright fringe. A linear polarizer (LP) acts as a polarizer and analyzer, a spatial filter (SF) acts on the input and output beams, and a phase modulator (PM) produces a bias on the signal for detection at the photodetector (DET). b) The polarization Sagnac interferometer with an external detection scheme in place of the internal phase modulation for signal readout. Additional elements include half-wave plates (HWP) and polarizing beamsplitters (PBS) to control the polarization of the circulating light.

input and output beams are colinear so a single spatial filter (SF) can simultaneously select the input and output mode, and, by construction, produce optimal overlap of the aligned interferometer.

Additionally a polarizer is necessary at the input and output of the interferometer to remove any polarization degeneracy of the detected spatial mode. This prevents elements that affect the polarization from changing the bias point of the interference condition or otherwise converting light into a form which produces noise on the detector without containing useful signal. In the polarization Sagnac interferometer the polarizing beamsplitter ( $PBS_2$ ) acts as both a polarizer for the incoming light and an analyzer for the output light so that the only light with the desired polarization reaches the photodetector.

Finally the reciprocal configuration of the Sagnac interferometer requires a method to produce a signal with a first order dependence on the differential phase of the interfering beams. This is achieved by allowing a fraction of the light returning towards the laser to be separated by the polarizing beamsplitter for use as a local oscillator[49][50]. Since the local oscillator is orthogonally polarized to the signal, its phase relative to the signal can be easily adjusted by using waveplates. Heterodyne sidebands can be added to the local oscillator field by a modulator acting preferentially on the correct polarization.

The key to having the four elements of reciprocal operation in the Sagnac detector, while observing the dark fringe of the interference, is controlling the polarization of the light in the interferometer.

## 3.2 Polarization control in the Sagnac interferometer

The elements of a reciprocal Sagnac configuration that are not met in the simple Sagnac configuration shown in figure 3a are the symmetric use of the beamsplitter and spatial and polarization filtering of the input and output beams to ensure perfect overlap of the detected beam with the input beam. These aspects of the reciprocal

Sagnac interferometer can be added to the Sagnac by using polarization control.

To use the beamsplitter symmetrically a polarizing beamsplitter is used as the main beamsplitter. Orthogonally-polarized components of the input polarization are split into the two counterpropagating beams. An element, such as a half-wave plate, in the interferometer rotates the polarization of the light by  $90^\circ$  so that the reflected beam returns to the beamsplitter and is transmitted and vice versa. In this configuration all of the light exits the interferometer on the reciprocal port of the beamsplitter. The polarization-rotating element in the interferometer ensures that the polarization of the counterpropagating beams is identical everywhere, while the polarizing beamsplitter acts as a polarization filter on the input and output beams to remove light that is not the correct polarization leaving the interferometer.

The output beam is collinear with the input beam and propagates back towards the laser. A spatial filter can simultaneously filter the spatial mode of the input and output beam to ensure spatial mode overlap of the beams. With the polarization control and the spatial filter, only a signal readout scheme is necessary to allow full reciprocal operation of the Sagnac interferometer.

### 3.3 Signal readout in the polarization Sagnac Interferometer

The light exiting the polarization Sagnac interferometer is the sum of two beams with orthogonal polarization states that counterpropagated through the interferometer arms. If no signal is present the relative phase of the two output polarization states is identical to the relative phase of the input polarization states. A signal introduces an additional time dependent phase difference between these states. Figure 3.4 shows that these two output polarizations can be projected onto a basis where the polarization components represent the sum and difference of the two interfering beams from the interferometer. The phase between these beams is a function of the polarization state of the input beam. To detect the dark fringe of interference we use a linearly polarized input beam and separate the orthogonal polarization state at the

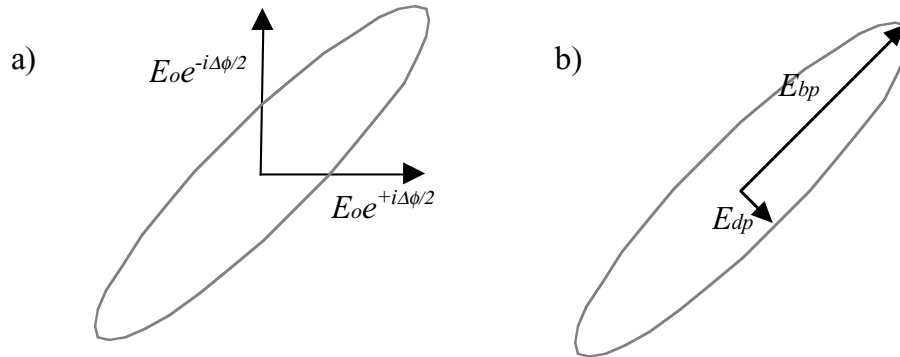


Figure 3.4: Elliptical polarization state of interferometer output. a) The relative phase shift of  $\Delta\phi$  between the orthogonally polarized interfering beams produces an elliptical polarization state. b) The output is resolved into polarization components along the principle axes of the ellipse. The dark polarization, the minor axis of the ellipse, contains the signal field and is a measure of the phase shift. The bright polarization, the major axis of the ellipse, is the carrier field and contains most of the power.

output for detection.

The dark polarization is separated from the output beam using a polarizer, which is chosen to leak a bit of the bright polarization for use as a local oscillator. The phase difference between the local oscillator and the signal is constant due to the common path they travelled in the interferometer. This eliminates the need for active phase control of the local oscillator that is usually necessary in external modulation schemes [51][52]. The static phase difference between the signal and local oscillator is adjusted using a wave plate. Heterodyne sidebands are added to the local oscillator by an electrooptic modulator oriented to only act on the local oscillator polarization. Balanced detection is accomplished by properly adjusting the polarization state of the output so that a polarizing beamsplitter resolves the beam into the sum and difference of the signal and the local oscillator to be separately detected allowing the photocurrents to be electronically subtracted [53][54].

The signal extraction technique described here has many useful advantages over other methods of signal extraction such as frontal [55] [56][57], internal [58] or external modulation. The local oscillator is common path to the signal eliminating the need for active phase control and eliminating the need for alignment as is necessary with

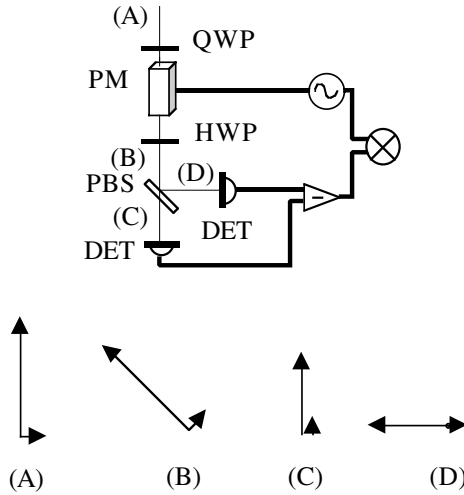


Figure 3.5: Heterodyne detection scheme for the polarization Sagnac interferometer. The polarization state of the signal and the local oscillator is shown at (A) the pickoff from the interferometer, (B) after rotation by the half wave plate and (C) and (D) on each of the balanced detectors. The phase modulator PM acts only on the vertical polarization.

external modulation. The electrooptic modulator is placed at the output of the interferometer, where it only sees the power in the dark fringe, eliminating many problems caused by transmitting high power through the modulator crystal, as is necessary for frontal and internal modulation. The balanced detection eliminates the first order sensitivity to amplitude noise which is otherwise present, and the common path nature of the detection scheme completely eliminates the dependence on frequency noise which is present when there is a path length asymmetry between any of the interfering beams.

### 3.4 Experimental investigations of a tabletop polarization Sagnac interferometer

Figure 3.6 shows a schematic of the 2 m arm-length polarization Sagnac tabletop interferometer with 75 bounce delay lines in each arm of the interferometer arms to lower the frequency of the interferometer's response peak to 275 kHz. A 300 mW

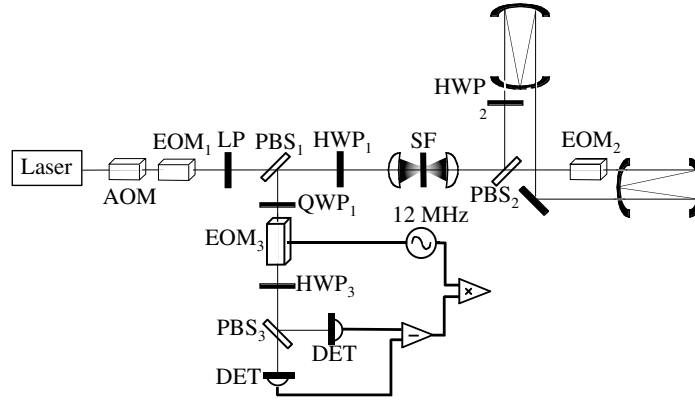


Figure 3.6: The optical layout of the 2 m 75 bounce delay-line polarization Sagnac interferometer with linear polarizer (LP), polarizing beamsplitters (PBS), half waveplates (HWP), quarter waveplate (QWP), spatial filter (SF), electrooptic modulators (EOM), acousto-optic modulator (AOM) and photodetectors (DET). Each arm contains a 75 bounce, 2 m long delay line. The beamsplitter  $PBS_1$  is slightly tilted to select 0.3% of the cross polarization. Not shown is the premode cleaner cavity immediately after the laser.

single frequency Nd:YAG non-planar ring oscillator was locked to a mode cleaner cavity [59] which was tuned to be a highly selective filter for the s-polarized  $TEM_{00}$  gaussian mode of the beam. The beamsplitter  $PBS_2$  has an extinction of -33 dB. A phase modulator,  $EOM_2$ , is placed in one arm of the interferometer immediately after the beamsplitter and driven by a waveform to generate a differential phase modulated signal. The light exiting the interferometer encounters the beamsplitter  $PBS_1$  that has been slightly misaligned in angle so as to reduce its extinction to -25 dB (0.3% leakage). This beamsplitter picks off 99.7% of the signal and 0.3% of the carrier to use as a local oscillator. Phase modulation sidebands are imposed on the local oscillator by the resonant electrooptic-optic modulator  $EOM_3$  for heterodyne detection at 12 MHz.

### 3.4.1 Fringe Contrast

The fringe contrast of the interferometer was measured and its dependence on different effects was investigated. Measurements of the fringe contrast were made with and

without the spatial filter, which is necessary to remove light converted out of the desired spatial mode.

A pair of 10x microscope objectives was used as a unity magnification telescope in the input and output beam paths with a 10  $\mu\text{m}$  pinhole placed at the focus between the objectives to reject high spatial frequency modes. The fringe contrast, defined by

$$C = \left( \frac{P_{bp} - P_{dp}}{P_{bp} + P_{dp}} \right), \quad (3.11)$$

where  $P_{bp}$  is the power exiting the bright port of the interferometer and  $P_{dp}$  is the power exiting the dark port of the interferometer, was measured to be 0.856 without the pinhole in place and 0.998 with the pinhole acting as a spatial filter. The improvement in fringe contrast represents a reduction of the background intensity by 20 dB.

### 3.4.2 Birefringence

Measurements of the fringe contrast with an extra birefringent element inside the interferometer loop that converts light out of the desired polarization confirmed that depolarization acts like a loss and does not reduce the fringe contrast. A misalignment of the half wave plate in the interferometer loop reduces the power reaching the detector by  $\cos^2(2\Delta\theta_2)$ . The power not reaching the detector is simply lost through the unused port of the beamsplitter  $PBS_2$ . A birefringent element in the interferometer, such as thermally induced birefringence in the mirrors, can also cause power to leak out the unused beamsplitter port if the birefringence principle axis is at an angle with respect to the circulating polarization direction. This was demonstrated by placing a variable retardation waveplate into the interferometer loop and measuring the power and the signal level transmitted to the detector. Figure 3.7 shows that a birefringent element at an angle  $\theta'$  with respect to the principle axes of the beamsplitter  $PBS_2$  having a retardation of  $\Gamma$ , the transmission efficiency of the interferometer is reduced to

$$\eta_i = \cos^2(\Gamma/2) + \cos^2(2\theta') \sin^2(\Gamma/2) \quad (3.12)$$

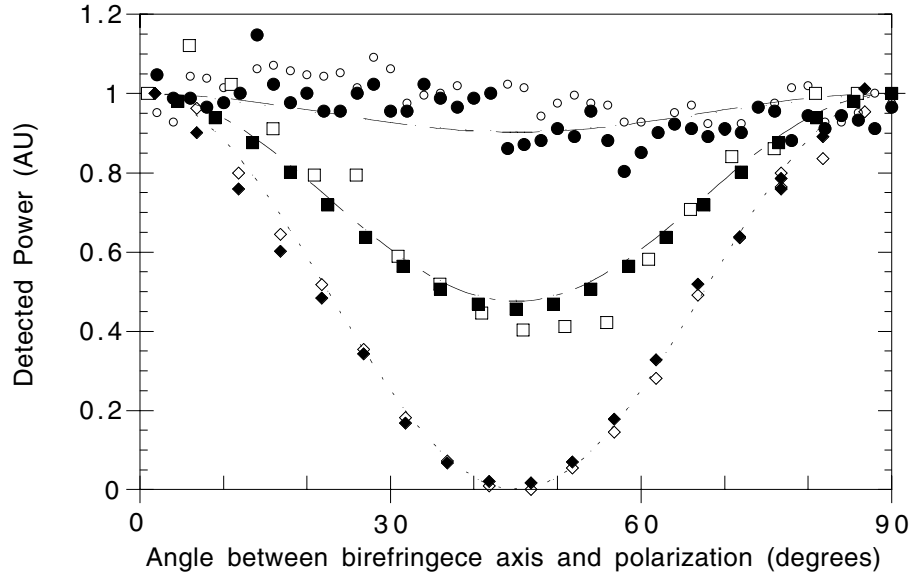


Figure 3.7: The reduction in power observed when an adjustable waveplate was present in the interferometer loop providing variable levels of birefringence oriented at selected angles with respect to the polarization direction of the beamsplitter. Solid markers indicate relative signal level, while hollow markers represent the total relative power level on the detector. Circles mark data for 0.09 waves of birefringence, diamonds mark data for 0.25 waves of birefringence and squares mark data for 0.5 waves of birefringence in the interferometer loop. The dotted line represents equation 3.12. The birefringence acts like a loss and does not reduce the contrast as is evidenced by the constant ratio between the signal and the total power.

for both the signal and the local oscillator, meaning that the birefringence caused a loss of useful power but did not degrade the fringe contrast.

### 3.4.3 Laser frequency noise

The sensitivity of the polarization Sagnac interferometer to frequency noise was measured. The input field was phase modulated with a swept frequency sin wave with a modulation depth of 2.5 rad by the electrooptic-optic modulator  $EOM_1$ . A 300 kHz differential signal was imposed on the light by the phase modulator  $EOM_2$  placed immediately after the beamsplitter  $PBS_2$  at the point of maximum asymmetry in the interferometer with a modulation depth of 32 mrad. Here the modulator's interaction

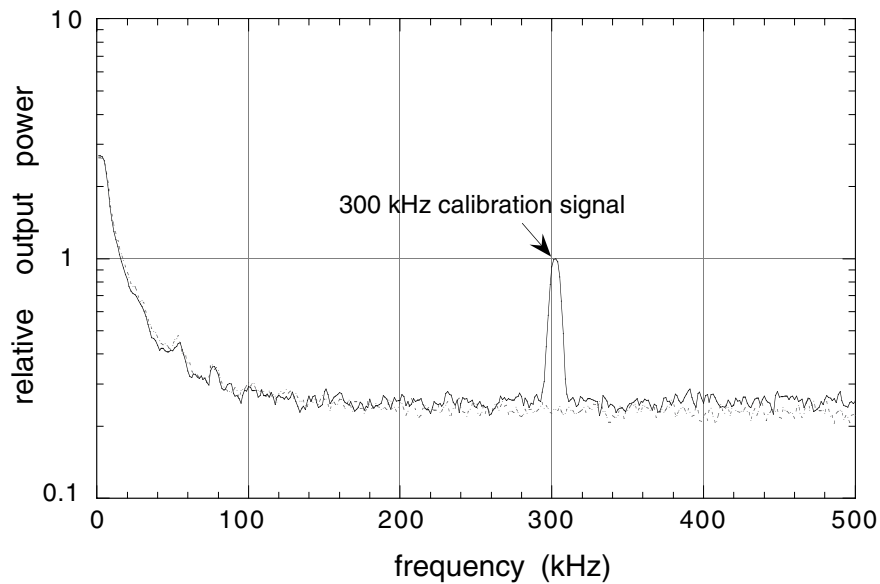


Figure 3.8: Measurement of the frequency noise suppression of the polarization Sagnac interferometer. The solid trace is the noise floor with input phase noise present. The dotted trace is without the input phase noise. The output power levels are normalized to a 32 mrad amplitude modulated calibration signal at 300 kHz. The difference between the two traces represents the conversion of the 2.5 rad of input frequency noise to amplitude noise on the detector, a coupling of less than  $2.5 \times 10^{-4}$ .

with each of the counter-propagating beams occurs with a relative delay of one loop transit time giving a peak frequency response at 275 kHz. Figure 3.8 shows traces of the interferometer output recorded with the phase modulation on and off. The average increase in the noise floor over the measurement bandwidth was attributed to the broadband phase modulation. The value of this noise was calibrated against the response of the interferometer to the 300 kHz signal. The coupling of relative frequency noise to relative amplitude noise by the interferometer from zero frequency to 4 times the peak frequency was less than  $2.5 \times 10^{-4}$ , representing excellent rejection of laser frequency noise.

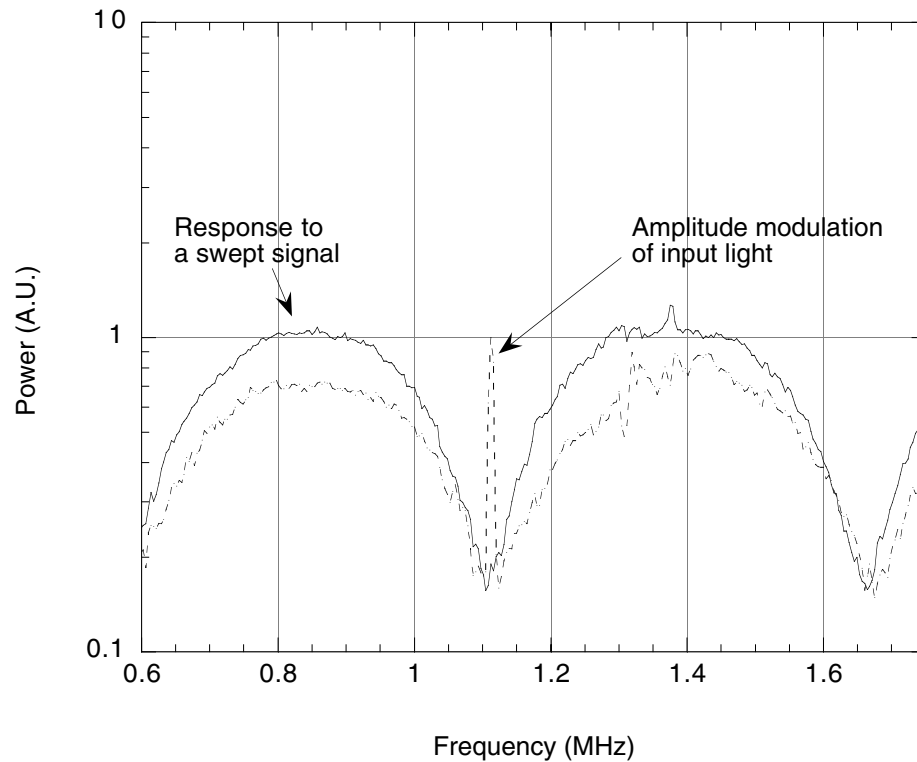


Figure 3.9: Demonstration of the amplitude noise suppression due to balanced detection. Both a differential swept-frequency signal, tracing out two peaks of the Sagnac interferometer response, and an amplitude modulation placed on the input field producing a spike at 1.125 MHz, are detected by a single detector (dashed trace). Using two balanced detectors (solid trace) the sensitivity to the amplitude modulation is reduced.

#### 3.4.4 Laser amplitude noise

A 1.125 MHz amplitude modulation was imposed on the input field by an acousto-optic modulator. This frequency was chosen to coincide with a null of the interferometer's frequency response so that a swept-frequency differential signal could also be imposed on the light without affecting the noise floor at the AM frequency. Figure 3.9 shows that with balanced detection the signal was observed but the amplitude noise spike was suppressed to the electronic noise of the measurement. When one detector was blocked the unbalanced output signal was reduced and the AM noise spike was observed.

### 3.5 Summary

In summary, the 2 m table top prototype demonstrated several important features of the polarization Sagnac interferometer. The polarization scheme allowed detection of the dark fringe on the symmetrical port of the beamsplitter, so that the fringe contrast is not degraded by asymmetry in the beamsplitter. Further, a spatial filter simultaneously acting on the input and output light prevented unintended spatial modes from reaching the photodetector and spoiling the high fringe contrast. Despite the use of polarization sensitive optics, birefringence in the interferometer only acts like a loss common to both beams, the magnitude of which is understood. The common paths of the interfering beams prevent laser frequency noise from being converted to amplitude noise at the detector, and the balanced detection scheme provided excellent rejection of laser amplitude noise. This shows that the polarization Sagnac interferometer has many of the characteristics desirable for an advanced gravitational wave detector. In the next few chapters I explore some of the challenges to developing a design based on this interferometer which would be appropriate for a LIGO-scale gravitational wave detector.

# Chapter 4

## Delay lines for energy storage

Delay lines are necessary to increase the storage time of the interferometer arms without compromising the common path nature of the Sagnac interferometer. Figure 4 shows that delay lines increase the interferometer response at low frequencies and can tune its peak response into the measurement band. Although the conceptual action of the delay line, to fold the path of the light, is simple to understand, there are many effects that the delay line has on the light beams that need to be understood; the geometry of the mirrors and the beam size in the delay lines must be optimized to reduce clipping of the beam, the effect of thermal noise at the perimeter of the mirror, where the reflection spots are located, must be understood, and scattered light trapped in the delay lines must be controlled and reduced. In this chapter I present a description of progress in each of these areas.

A significant result of my work is the development of a method to reduce the effects of noise from scattered light – a method that is technically easy to implement. The method uses a slow laser frequency sweep and is presented in section 4.2.3. An additional result is a constraint placed on allowable beam clipping found by numerical analysis described in section 4.1.4. Although constraints on beam size and delay line geometry have been previously investigated[60][61][62] [63] and are well understood, I reproduce much of this analysis in this chapter for completeness.

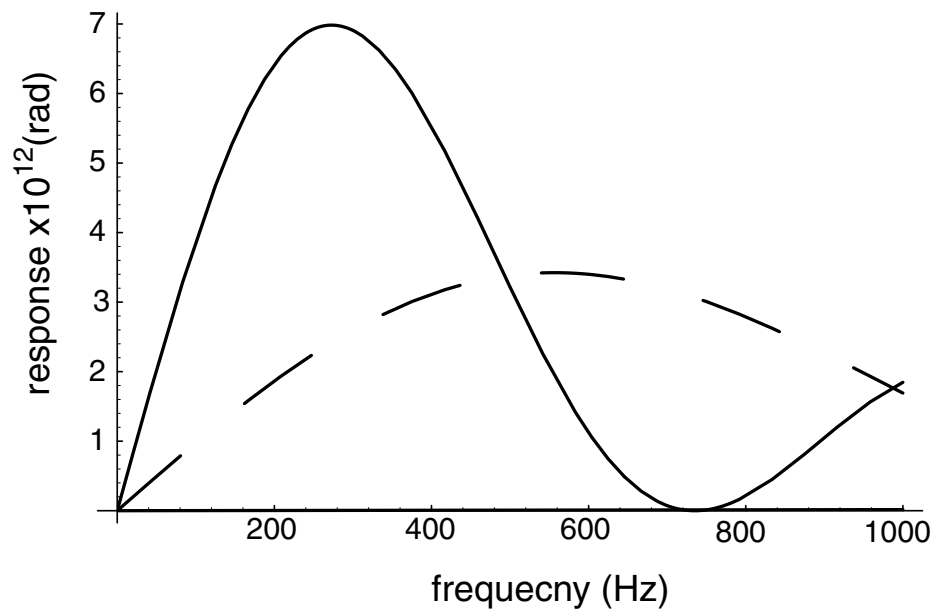


Figure 4.1: The response of the delay line Sagnac interferometer with laser illumination at 532 nm. The solid curve is for a 4 km interferometer with 51 bounce delay lines in the arms. The dashed curve is for a 2 km interferometer with 51 bounce delay lines or equivalently a 4 km interferometer with 25 bounce delay lines in the arms.

## 4.1 The delay line design

In this section I describe the analysis which leads to the parameters for a LIGO-scale delay line; the geometry of the delay line, the gaussian beam parameters of the beam in the delay line, the effect of beam clipping and the constraints it places on the mirror size. The techniques necessary to implement the design without degrading the sensitivity of the interferometer are discussed in the section 4.2.

### 4.1.1 Delay line geometry

The simplest delay line geometry consists of a light path folded between two mirrors. The mirrors may in general be curved so as to steer and focus the beam on each reflection. The required mirror sizes depend on the number of folds, the spot separation and the spot sizes on the mirror. From symmetry the spot sizes, and thus the required mirror size for equal diameter mirrors, are minimized when the mirrors have equal radii of curvature. We therefore restrict our analysis to the case of equal radii mirrors.

The ABCD matrix [23] describing the mirrors and the propagation distance between the mirrors can be used to calculate the beam's position, orientation, and gaussian beam parameters at every reflection from the mirrors. The ABCD matrix describing gaussian beam propagation generalized to allow beam astigmatism is a 4x4 block diagonal matrix containing the 2x2 matrices describing the propagation of the x and y components of the beam. It is given by

$$M = \begin{bmatrix} M_x & 0 \\ 0 & M_y \end{bmatrix} = \begin{bmatrix} A_x & B_x & 0 & 0 \\ C_x & D_x & 0 & 0 \\ 0 & 0 & A_y & B_y \\ 0 & 0 & C_y & D_y \end{bmatrix} \quad (4.1)$$

This formalism allows us to consider astigmatic mirrors. However, we limit consideration to the case where the axis of the astigmatism of the mirrors are parallel, so that the overall ABCD matrix remains block diagonal. In this form the solutions for the beam shape in the x and y directions are separable. The ABCD matrix allows us

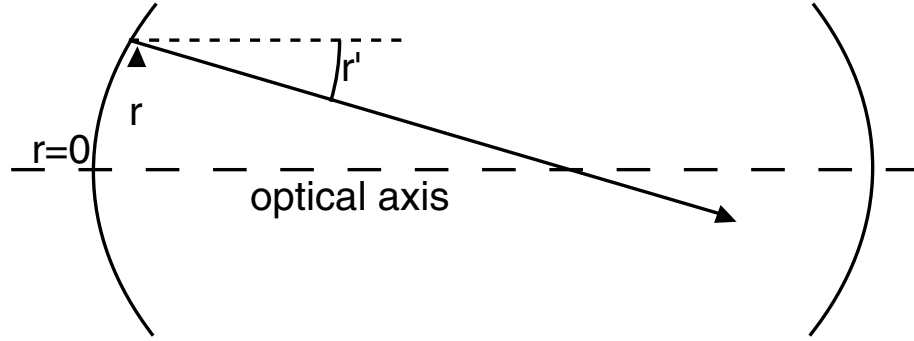


Figure 4.2: The the ray position and angle for calculations with the ABCD matrices. The ray angle,  $r'$ , is measured with respect to the direction of the optical axis. The ray position,  $r$ , is measured with respect to the intersection of the optical axis with the mirror surface.

to calculate the ray position and angle from

$$\begin{bmatrix} r_1 \\ r'_1 \end{bmatrix} = \begin{bmatrix} A & B \\ C & D \end{bmatrix} \begin{bmatrix} r_0 \\ r'_0 \end{bmatrix} \quad (4.2)$$

Where  $r_0$  and  $r_1$  the beam positions and  $r'_0$  and  $r'_1$  are the tangents of the angles of the rays before and after the optical system. Figure 4.2 shows a ray in the delay line. The optical axis of the delay line, from which the beam angle is measured, is defined by the line connecting the center of curvature of the two mirrors. The center of the mirrors,  $R = 0$ , is at its intersection with the mirror surfaces. In a delay line with two curved mirrors separated by a distance  $L$  the ABCD matrix for a single pass, or half-round-trip, is constructed from the submatrices  $M_x$  and  $M_y$  described by

$$M_{x,y} = \begin{bmatrix} 1 & L \\ -\frac{2}{R_{x,y}} & \left(1 - \frac{2L}{R_{x,y}}\right) \end{bmatrix} \quad (4.3)$$

where  $R$  is the radius of curvature of the mirrors in the x or y directions for  $M_x$  or  $M_y$  respectively.

Requiring that the beam exit the delay line after  $2N$  single passes, or  $N$  round-trips, at the same location where it enters requires that

$$M^{2N} = I. \quad (4.4)$$

Thus the eigenvalues for  $M$  must obey

$$\lambda^{2N} = 1 \quad (4.5)$$

allowing the eigenvalues to be written as

$$\lambda_1 = e^{i\theta} \quad \text{or} \quad \lambda_2 = e^{-i\theta} \quad (4.6)$$

where

$$\theta = \frac{\pi m}{N} \quad (4.7)$$

with  $m$  an integer.

For the ABCD submatrices of equation 4.3 the eigenvalues are

$$\lambda_{x,y} = \left(1 - \frac{L}{R_{x,y}}\right) \pm i \sqrt{1 - \left(1 - \frac{L}{R_{x,y}}\right)^2} \quad (4.8)$$

Equating 4.6 to 4.8 gives

$$\cos \theta_{x,y} = 1 - \frac{L}{R_{x,y}} \quad (4.9)$$

The position of the reflection spots can be found by propagating the input ray vector through powers of the single pass ABCD matrix. Sylvester's Theorem, which states that for any polynomial  $P(M)$  of a square matrix  $M$ , where  $\lambda_i$  represents one of  $N$  distinct eigenvalues of  $M$ ,

$$P(M) = \sum_{i=1}^N P(\lambda_i) \prod_{j \neq i} \frac{M - \lambda_j I}{\lambda_i - \lambda_j}, \quad (4.10)$$

can be used to find the value of the ABCD submatrices describing  $n$  half-round trips

between the mirrors

$$M_{x,y}^n = \frac{1}{\sin \theta} \begin{bmatrix} \sin n\theta - \sin(n-1)\theta & L \sin n\theta \\ -\frac{2}{R_{x,y}} \sin n\theta & 1 - \frac{2L}{R_{x,y}} \sin n\theta - \sin(n-1)\theta \end{bmatrix} \quad (4.11)$$

This matrix, used in equation 4.2 gives the position of the beam spot after  $n$  passes between the delay line mirrors

$$r_n = \frac{1}{\sin \theta} ((r_0 + Lr'_0) \sin n\theta - \sin(n-1)\theta). \quad (4.12)$$

We can find the condition that allows the most compact spot pattern by requiring that no spot be at a further distance from the mirror center than the input spot. Thus  $\sin(-\theta) < \sin(n-\theta)$  for  $n \neq 0$ . Together with the condition of equation 4.7 this requires  $\theta = \frac{\pi}{2} - \frac{\pi}{2N}$ ,  $N$  to be odd, and  $r'_0 = -\frac{L}{r_0}$ .

For  $N \gg \frac{\pi}{2}$  the pattern of spots on the mirrors is well approximated by

$$r_{x,n} = r_0 \cos n\theta_x \quad (4.13)$$

$$r_{y,n} = r_0 \cos n\theta_y \quad (4.14)$$

where the  $n = 0$  spot is assumed to be in the corner of the mirror. The spot pattern traces out a Lissajou pattern, which for spherical mirrors is an ellipse, as shown in Figure 4.3. If it is desired that the input spot be at a location other than the corner of the mirror, the spots can be renumbered by adding an arbitrary offset in the arguments of equations 4.13 and 4.14.

### 4.1.2 Gaussian beam parameters of the beam in the delay line

The Gaussian parameters of the beams in the delay line tell us how big the waist will be at each reflection spot. Together with the spot locations found in 4.1, this allows us to calculate the necessary mirror sizes. The ABCD matrix describing the transformation of the ray parameters in the delay line also describes the transformation of

the complex parameter,  $q(x)$ , of a Gaussian beam defined by

$$\frac{1}{q(x)} = \frac{1}{R(x)} - \frac{i\lambda}{\pi\omega^2(x)}. \quad (4.15)$$

After propagating through a system described by an ABCD matrix the output q-parameter,  $q_1$  is related to the input q-parameter,  $q_0$  by the ABCD rule

$$q_1 = \frac{Aq_0 + B}{Cq_0 + D} \quad (4.16)$$

With the multipass ABCD matrix given by equation 4.10 and the transformation law for the Gaussian q-parameter given by equation 4.16 the q-parameter of the beam at the mirror surface can be computed after  $n$  passes between the mirrors,

$$q_n = \frac{(\sin n\theta - \sin(n-1)\theta)q_0 + L \sin n\theta}{\frac{-2}{R} \sin n\theta q_0 + \left(1 - \frac{2L}{R}\right) \sin n\theta - \sin(n-1)\theta}, \quad (4.17)$$

for the x and y-directions independently. Here  $q_0$  is the Gaussian q-parameter of the input beam defined by

$$\frac{1}{q_0} = \frac{1}{R_{in}} - \frac{i\lambda}{\pi\omega_{in}^2}. \quad (4.18)$$

The beam waist at the  $n^{\text{th}}$  reflection on the mirror surface is found from equation 4.15 and 4.17 and the trigonometric relations

$$\sin((n-1)\theta) = \cos(\theta) \sin(n\theta) - \sin(\theta) \cos(n\theta) \quad (4.19)$$

$$\sin^2(\theta) = 1 - \cos^2(\theta). \quad (4.20)$$

The waist is given by

$$\begin{aligned} \left(\frac{\omega_n}{\omega_0}\right)^2 &= \frac{1}{\sin^2\theta} \left( \left[ \left(\frac{L\lambda}{\pi\omega_0^2}\right)^2 + \left(\frac{L}{R} + \frac{L}{R_0}\right)^2 \right] \sin n\theta^2 + \right. \\ &\quad \left. 2 \left[ \sin\theta \left(\frac{L}{R} + \frac{L}{R_0}\right)^2 \right] \sin n\theta \cos n\theta + \sin^2\theta \cos n\theta^2 \right). \end{aligned} \quad (4.21)$$

When written in terms of  $\omega_m$ , the waist size of the cavity mode formed by the

mirrors,

$$\omega_m = \sqrt{\frac{\lambda L}{\pi \sin \theta}} \quad (4.22)$$

equation 4.21 becomes

$$\begin{aligned} \left(\frac{\omega_n}{\omega_0}\right)^2 = & \frac{1}{2} \left( 1 + \left(\frac{\omega_m}{\omega_0}\right)^4 + \left(\frac{\pi\omega_m^2}{\lambda}\right)^2 \left(\frac{1}{R} + \frac{1}{R_0}\right)^2 \right) + \\ & \frac{1}{2} \left( 1 - \left(\frac{\omega_m}{\omega_0}\right)^4 - \left(\frac{\pi\omega_m^2}{\lambda}\right)^2 \left(\frac{1}{R} + \frac{1}{R_0}\right)^2 \right) \cos 2n\theta + \\ & \left(\frac{\pi\omega_m^2}{\lambda}\right) \left(\frac{1}{R} + \frac{1}{R_0}\right) \sin 2n\theta, \end{aligned} \quad (4.23)$$

from which it can be shown that the maximum and minimum spot sizes on the mirrors obey

$$\omega_{min}\omega_{max} = \omega_m^2. \quad (4.24)$$

Knowledge of the sizes of the spots on the mirrors is necessary to determine the minimum mirror diameter necessary to accommodate a given number of spots, or conversely the maximum delay that can be achieved in a delay line for LIGO given the constraints that the vacuum system places on the mirror diameter.

### 4.1.3 Delay line mirror size

With the size of the spot pattern, and the beam spot sizes calculated, it is straightforward to determine the size of the mirrors necessary to accommodate a delay line with a given number of spots. The mirror must be large enough so that the edges of the spots do not fall off the mirror and the spots must be separated enough so that they don't overlap at the input aperture. These constraints lead to different required mirror sizes for spherical mirrors and astigmatic mirrors as well as for different input beam parameters. In all cases we quantify the amount of tolerable clipping by the S-parameter, which measures the minimum radial distance,  $a$ , at which the beam is

allowed to be clipped, measured in units of the beam radius,

$$S = \frac{a}{\omega} \quad (4.25)$$

We consider the various cases separately.

### Spherical mirrors with matched spots

The simplest case to consider is a delay line with spherical mirrors so that the spot pattern traces out an ellipse on the mirror. If the input beam is chosen to focus to a waist at the center of the delay lines and have a phasefront with a radius of curvature at the mirrors that match the curvature of the mirrors the spots will all be the same size given by

$$\omega = \omega_m = \pi \sin \theta \sqrt{\lambda L}. \quad (4.26)$$

The spots must be separated by  $S$  beam radii to avoid overlap at the input aperture. This requires the circumference of the spot pattern be

$$\pi D_p \geq N \times 2S\omega \quad (4.27)$$

where  $D_p$  is the diameter of the spot pattern on the mirrors. The edges of the mirror must extend  $S\omega$  beyond the spot pattern to prevent the beam spots from spilling over the edge of the mirror. This requires

$$D_m \geq D_p + 2S\omega \quad (4.28)$$

The relations 4.26, 4.27, and 4.28 combine to give the expression for the required mirror diameter of a matched, spherical delay line

$$D_m \geq \left( \frac{2N}{\pi} + 2 \right) S \sqrt{\frac{\lambda L}{\pi \sin \theta}}. \quad (4.29)$$

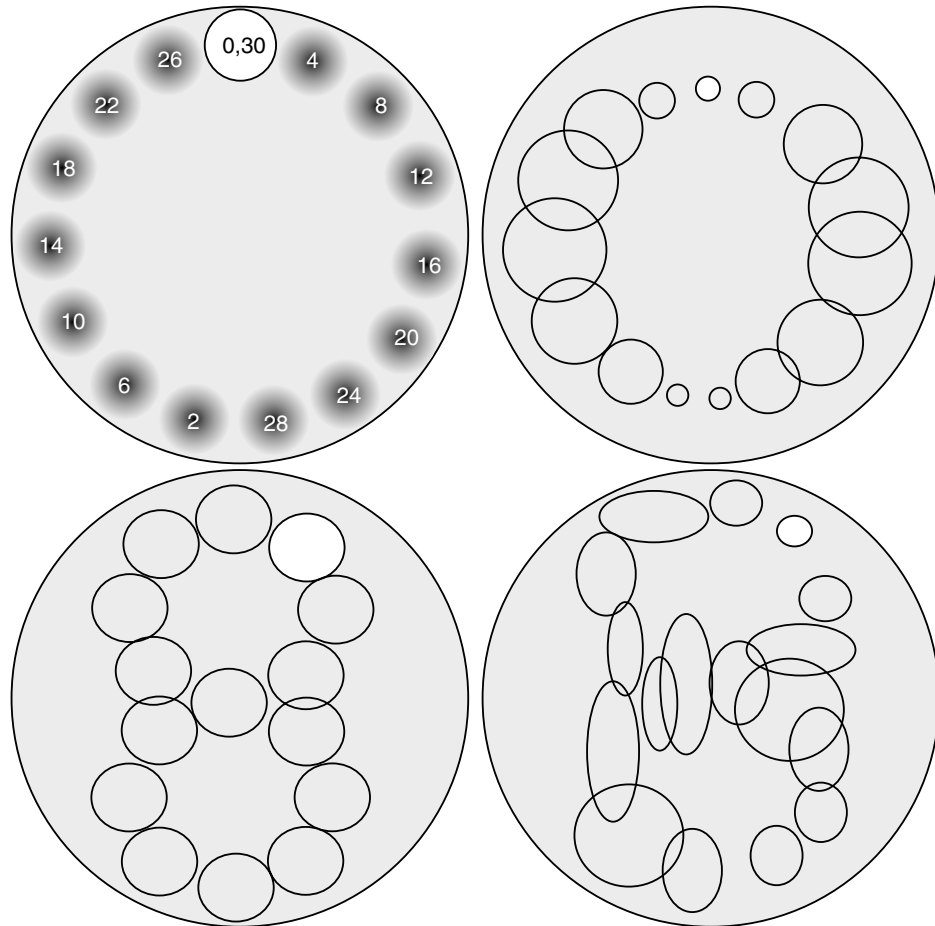


Figure 4.3: The reflection spot pattern on the input mirror for a matched geometry with spherical mirrors (top left), an unmatched geometry with spherical mirrors (top right), a matched geometry with aspherical mirrors (bottom left), and an unmatched geometry with aspherical mirrors (bottom right). The top left drawing contains the spot numbers as well to better illustrate the path the beam takes in the near-confocal geometry. Multiple delay lines can share a common mirror provided their spot patterns and input holes are well separated. For example a smaller pattern of spots from a 2 km delay line could illuminate the central region of a 4 km delay line with spherical mirror producing an inner circle of spots in the the top two diagrams.

### Spherical mirrors with unmatched spots

For delay lines with many spots it becomes advantageous to focus the input beam to a tighter spot than the matched beam size  $\omega_m$ . This causes the spots near the input aperture to be smaller than in the matched case, which allows them to be closer together without overlapping. Other spots, however, become larger than the matched diameter and require the mirror to extend further beyond the center of the spots; the largest spot size is described by equation 4.24. There is an optimum input beam size which minimizes the required size of the mirror. The constraint of relation 4.27, that the spots not overlap at the input hole, can be approximated by

$$D_p \geq \frac{2N}{\pi} S \omega_{in} \quad (4.30)$$

where we replace the size of the spots neighboring the input aperture with the size of the input beam. The constraint on the mirror diameter given by relation 4.28 and the relationship between the minimum and maximum spot sizes, given by equation 4.24, gives a required mirror diameter of

$$D_m \geq D_p + 2S\omega_{max} = D_p + 2S\frac{\omega_m^2}{\omega_{in}}. \quad (4.31)$$

With the constraint on the spot pattern diameter of equation 4.30 this becomes

$$D_m \geq \frac{2N}{\pi} S \omega_{in} + 2S\frac{\omega_m}{\omega_{in}}. \quad (4.32)$$

Minimizing the mirror diameter with respect to  $\omega_{in}$  gives

$$D_m \geq \frac{4S}{\pi} \sqrt{\frac{\lambda LN}{\sin \theta}} \quad (4.33)$$

with the input beam focused to a spot size of

$$\omega_{in} = \sqrt{\lambda LN} \sin \theta \quad (4.34)$$

at the input.

### Aspheric Mirrors with matched spots

The mirror size necessary to accommodate spot patterns that follow Lissajou figures other than simple ellipses depends on the order of the Lissajou figure, but as the spot pattern now includes the center of the mirror, efficient packing of the spots is possible and occurs when the spots are well distributed over the entire area of the mirror. The mirror area must be sufficiently large to accommodate all  $N$  spots, requiring the height and width of the mirror

$$H_m = W_m \geq 2S\sqrt{N}\omega_m \quad (4.35)$$

For a cylindrical mirror substrate the diameter of the substrate must be large enough to accommodate the square filled with the spot pattern, and also the edges of the outer-most spots that extend beyond the edge of the pattern of spot centers. This requires a mirror diameter of

$$D_m \geq 2S\sqrt{2N}\omega_m + 2S\omega_m, \quad (4.36)$$

which can be written as

$$D_m \geq 2S(\sqrt{2N} + 1)\sqrt{\frac{\lambda L}{\pi \sin \theta}} \quad (4.37)$$

### Aspheric Mirrors with unmatched spots

If we consider aspheric mirrors that produce a Lissajou spot pattern, but allow the input beam to be optimally focused to increase the number of spots on the mirrors we find that relation 4.36 becomes

$$D_m \geq 2S\sqrt{2N}\omega_{in} + 2S\frac{\omega_m^2}{\omega_{in}} \quad (4.38)$$

which is minimized when

$$\omega_{in} = \frac{1}{\sqrt[4]{2N}}\sqrt{\frac{\lambda L}{\pi \sin \theta}} \quad (4.39)$$

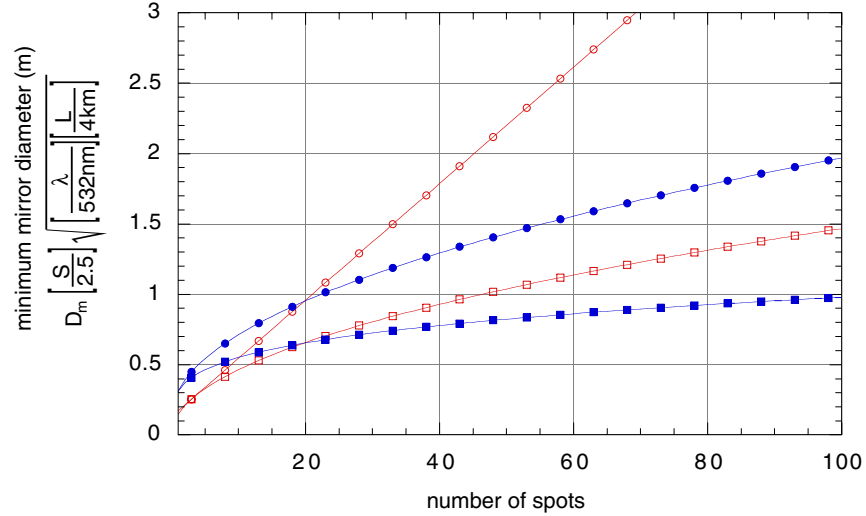


Figure 4.4: The minimum mirror diameter required for various delay line configurations as a function of the number of spots on the mirror. Hollow circular markers represent spherical mirrors with matched spots. Solid circular markers represent spherical mirrors with unmatched spots. Hollow square markers represent aspheric mirrors with matched spots and solid square markers represent aspheric mirrors with unmatched spots. The delay line has a clipping parameter of  $S = 2.5$  as defined by equation 4.25, a wavelength of  $\lambda = 532nm$ , and a mirror separation of  $L = 4km$ .

giving

$$D_m \geq 4S \sqrt[4]{2N} \sqrt{\frac{\lambda L}{\pi \sin \theta}} \quad (4.40)$$

Figure 4.1.3 shows that a delay line with less than 20 spots the aspheric mirrors with matched spot sizes allow the smallest mirrors of the 4 configurations. For 20 or more spots, however, the aspheric delay line mirrors with unmatched spots allow the smallest mirrors. Since more than 20 bounces are necessary to set the peak frequency response to less than 1 kHz with LIGO's 4 km arms, it is beneficial to use aspheric mirrors with unmatched spots. With 532 nm light and a clipping factor of  $S = 2$  to achieve 51 round trips in the delay line, enough to bring the peak frequency of a LIGO scale Sagnac interferometer below 400 Hz, 67 cm diameter aspheric mirrors or 86 cm diameter spherical mirrors are necessary. If larger mirrors are available the beam clipping could be reduced or the number of spots increased to improve the low frequency response of the delay-line Sagnac interferometer.

#### 4.1.4 Effect of beam clipping

Clipping the Gaussian beam at the input and output aperture and by the edge of the delay line mirrors cause power to be lost and the phase front of the beam in the far field to become convoluted. The amount of clipping which can be tolerated is a critical parameter in determining the size of the delay line mirrors required to accommodate a given number of spots since the required mirror size scales linearly with the clipping parameter,  $S$ , defined by equation 4.25.

Numerical modelling of a Gaussian beam propagating through a delay line with clipping from the mirror edge and the input aperture allows determination of the effects of the clipping on the interferometer sensitivity. Using a fast fourier transform algorithm for propagating the beam through free space we compare the output of a delay line with clipping to an ideal beam. We define the contrast as the residual power when the beams destructively interfere compared to the power in the uninterfered beams

$$C = 10 \log \frac{P_{dp}}{P_0} \quad (4.41)$$

The simulation shows that the effect of the aperture clipping is comparable to that of the edge clipping, which validates our choice of a single clipping parameter for both effects. The results of the model suggest that this contrast loss is less than the actual power loss due to the tails of the Gaussian beam being clipped. For a clipping loss of 1% a clipping tolerance of  $S \geq 2$  is desired to keep the contrast above 40 dB, the level at which 1 W of excess power is incident on the photodetector for 10 kW of circulating power. This level allows the delay line spot patterns to be small enough to fit within the 1 m diameter LIGO vacuum tanks while having enough spots to bring the peak frequency of the interferometer into the measurement band when light with a wavelength of  $532nm$  or shorter is used.

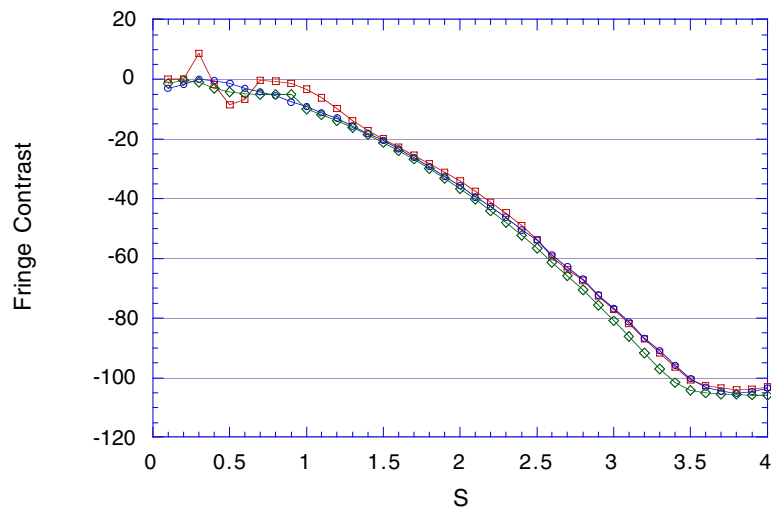


Figure 4.5: The interference fringe contrast between a clipped beam and an unclipped beam. The circular markers represent the effects of only clipping by the edge of the mirror. The diamond markers represent clipping only at the input aperture and the square markers represent the effects of both forms of clipping.

## 4.2 Implementation of the delay line

Having discussed the parameters for a LIGO-scale delay line in the previous section, I describe in this section what is necessary to implement the design without degrading the sensitivity of the interferometer. Alignment requirements of the end mirrors, noise imposed on the beam by thermally induced fluctuations of the mirror surface, and the control of scattered light in the interferometer through a laser frequency sweep are discussed.

### 4.2.1 Alignment tolerances of the delay line

When the re-entrance condition is met for the delay line spots the output beam behaves as if the input beam were reflected off of the back surface of the delay line. Thus the behavior of the beam in the delay line can be separated from the behavior of the beam outside of the delay line.

If the delay line mirrors have an astigmatism which prevents the reentrance condition from being met, or the separation of the mirrors is not correct for the output beam to be reimaged at the entrance spot, the output beam will be offset from the input beam. While this would cause misalignment of the beams in a Michelson interferometer with delay lines, it can be accommodated in a Sagnac interferometer as the position and angle of the turning mirror can be adjusted to accommodate the offset beam.

Tilting of either delay line mirror changes the orientation of the optical axis of the delay line, and hence changes the centerpoint for the spot patterns on the mirrors. The change in position of the spots is

$$\Delta x_n = \frac{y_n - y_0}{2y_0} L \Delta \theta_{y, far} + \frac{x_n}{x_0} L \Delta \theta_{y, near} \quad (4.42)$$

$$\Delta y_n = \frac{y_n - y_0}{2y_0} L \Delta \theta_{x, far} + \frac{x_n}{x_0} L \Delta \theta_{x, near} \quad (4.43)$$

where  $\Delta \theta$  is the tilt of the near or far mirror around the x or y-axis as labeled. The change in optical path created by a misaligned delay line mirror can be approximated by N times the change in length between the line segment connecting the center of

each of the spot patterns on the mirrors.

$$\Delta L \approx N \left( \sqrt{L^2(1 + \Delta\theta_x^2 + \Delta\theta_y^2)} - L \right) \quad (4.44)$$

resulting in an additional phase accumulated in the delay line of

$$\Delta\phi \approx \frac{NkL}{2} (\Delta\theta_x^2 + \Delta\theta_y^2). \quad (4.45)$$

There is no first order sensitivity to misalignment of the delay line mirrors. Second order noise couplings are discussed in chapter 5.

### 4.2.2 Thermal noise from the delay line mirrors

For frequencies from 20 Hz to 200 Hz thermal noise in the core optics is expected to be the dominant noise source. The thermal noise level is dependent only on the temperature of the optic, which determines the thermal energy driving the vibrational modes of the optic, and the material parameters of the optics that determine the frequencies and quality factor for those modes. By using materials with low elastic loss that support acoustic modes with a high quality, and by constructing the optic so that the lowest frequency vibrational modes are well above the measurement band most of the thermal energy can be channeled out of the measurement band into higher frequency vibrations that produce noise spikes at several kilohertz. For materials with a finite loss, however, the tails of these spikes extend into the measurement band with an amplitude that limits the sensitivity of the interferometer. Since the vibrational modes of the core optics are well above the measurement band, we use a quasi-static approach to find the response of the mirror to thermally induced mirror fluctuations at the frequencies of interest.

Nakagawa[64][65] has shown that the spectral density of phase noise induced on a Gaussian beam by reflection from a mirror at finite temperature can be related to the elastic properties of the mirror by

$$S_\varphi^{Single}(\omega) = \frac{16}{\pi^2} \frac{k^2}{w^4} \iint dS \iint dS' e^{-2|\vec{r}|^2/w^2} e^{-2|\vec{r}'|^2/w^2} \langle \delta z(\vec{r}) \delta z(\vec{r}') \rangle_\omega \quad (4.46)$$

where  $k$  is the wavevector,  $r$  and  $r'$  are the position vectors for the mirror and the Gaussian beam. The static Green's function for the optic is used to calculate the cross spectral density of surface displacements. Equation 4.46 was used to calculate the spectral density of phase noise on a beam passing through a delay line, giving

$$\begin{aligned} S_\varphi(\omega) &= S_\varphi^E(\omega) + S_\varphi^I(\omega) \\ &= \sum_{n=1}^N S_\varphi^E(\omega, \vec{r}_n, \vec{r}_n) + 2 \sum_{n=2}^N \sum_{q=1}^{n-1} \cos[2(n-q)\tau\omega] \cdot S_\varphi^E(\omega, \vec{r}_n, \vec{r}_q) \\ &\quad + \sum_{n=1}^{N-1} S_\varphi^I(\omega, \vec{\rho}_n, \vec{\rho}_n) + 2 \sum_{n=2}^{N-1} \sum_{q=1}^{n-1} \cos[2(n-q)\tau\omega] \cdot S_\varphi^I(\omega, \vec{\rho}_n, \vec{\rho}_q), \end{aligned} \quad (4.47)$$

where  $S_\varphi^E(\omega)$  and  $S_\varphi^I(\omega)$  are the spectral density of phase noise produced by the end mirror and the input mirror respectively. For comparison the spectral density of phase noise on a beam passing through a Fabry-Perot cavity is

$$S_\varphi^{FP}(\omega) = \left[ \frac{(1+r)^2}{(1+r^2)} \right] \left[ 1 - \frac{2r_I}{1+r_I^2} \cos(2\omega\tau) \right]^{-1} \left[ S_\varphi^E(\omega) + r_I^2 S_\varphi^I(\omega) \right] \quad (4.48)$$

where  $\tau$  is the transit time and  $r_I$  is the input mirror field reflectivity.

Further it is shown that for the case of half-infinite mirrors, which contains much of the essential physics of the actual geometry but is easier to model, the spectral density of phase noise from a single reflection off of the mirror is

$$S_\varphi^{Single}(f) = \frac{4KT}{\pi^{3/2}} \frac{\phi(f)}{f} \frac{k^2}{w} \frac{(1-\sigma^2)}{E} \quad (4.49)$$

where  $K = 1.38 \times 10^{-23} \text{ J/K}$  is the Boltzmann constant,  $T$  is the mirror temperature,  $\phi(f)$  is the material loss,  $\sigma$  is the Poisson ratio and  $E$  the Young's Modulus. This gives a spectral density of phase noise for a Gaussian beam exiting a delay line formed by half-infinite mirrors,

$$\begin{aligned} S_\phi(f) &= S_\phi^{Single}(f) \{ (2N-1) + \\ &\quad 2 \sum_{n=2}^N \sum_{q=1}^{n-1} \cos[2(n-q)\tau\omega] e^{-(\vec{r}_n - \vec{r}_q)^2 / 2w^2} I_0 \left[ (\vec{r}_n - \vec{r}_q)^2 / 2w^2 \right] + \end{aligned}$$

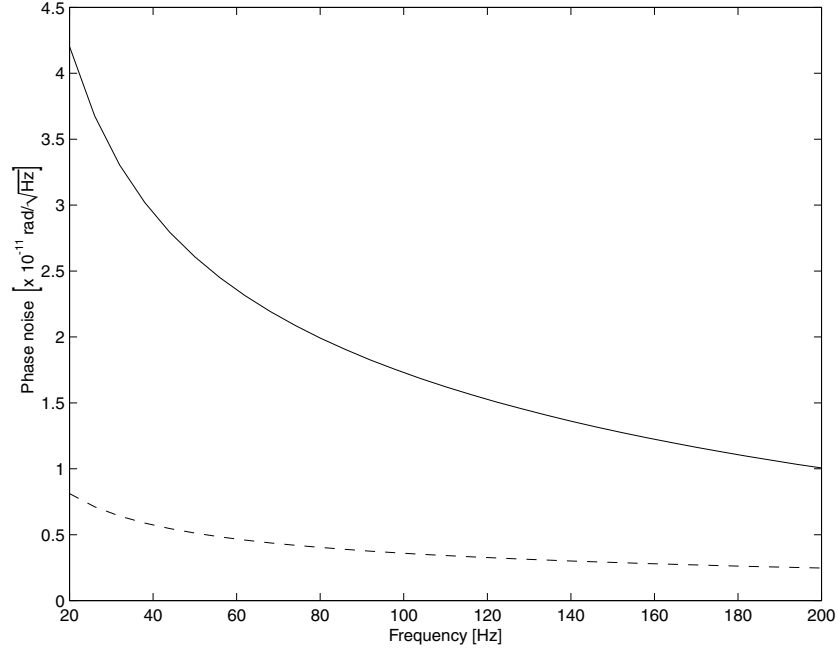


Figure 4.6: The phase noise induced by thermal noise in a matched spherical delay line (dashed curve) with 51 round trips, a beam separation of 2.5 beam radii, a laser wavelength of 532 nm and half-infinite silicon mirrors with a material loss of  $10^{-7}$  over the plotted frequency range. The thermal noise in a Fabry-Perot cavity (solid curve) for optics with the same material parameters is shown for comparison. The reflectivity of the mirrors is chosen so that the cavity has the same storage time as the delay line.

$$2 \sum_{n=2}^{N-1} \sum_{q=1}^{n-1} \cos [2(n-q)\tau\omega] e^{-(\vec{\rho}_n - \vec{\rho}_q)^2 / 2w^2} I_0 [(\vec{\rho}_n - \vec{\rho}_q)^2 / 2w^2] \} \quad (4.50)$$

where  $I_0(x)$  is the modified Bessel function of the first kind.

Figure 4.6 shows that over the range of frequencies where thermal noise is expected to be the dominant noise source, from 20 Hz to 200 Hz, the thermal noise in a delay line with half infinite mirrors is below that of a Fabry-Perot cavity with an equivalent storage time.

The thermal noise from the delay line becomes identical to that from the Fabry-Perot cavity as the separation of the delay line spots is reduced to zero. The results of this analysis can be understood by realizing that the cross spectral density of surface

displacements for the spots on the mirror is unity when the spots are collocated, as is the case for the Fabry-Perot, and decreases as the spot separation increases. In a real mirror with edges, the cross spectral density of surface displacements for spots located near the edges may increase compared to the half-infinite mirrors of the Nakagawa analysis. The correlation between separated spots, however, is always less than for collocated spots so we expect the results of this analysis still apply to finite physical mirrors.

### 4.2.3 Laser frequency sweep to control scattered light noise

The insensitivity of the Sagnac interferometer to laser amplitude and frequency noise and to out-of-band mirror motions is a consequence of the common path of the interfering beams. In a delay line, however, stray light can be scattered into the cavity formed by the delay line mirrors, travel many kilometers in the cavity then scatter back into the main mode of the interferometer increasing the interferometer's sensitivity to common-mode noise and out-of-band mirror motions[66]. Several methods have been considered for reducing the effect of this stray light[67][68]. We propose and demonstrate a promising new method using a laser frequency sweep that takes advantage of the Sagnac interferometer's insensitivity to out-of-band laser frequency noise [69].

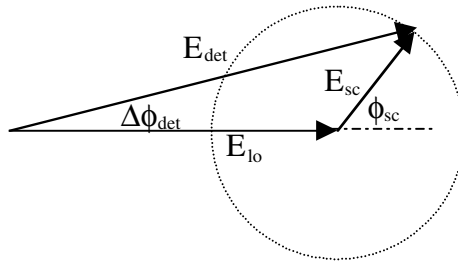


Figure 4.7: Phasor sum of local oscillator and scattered light field on the photodetector produces an uncertainty in the local oscillator phase.

The stray light, with its different number of passes between the delay line mirrors, can be differentiated from the light of the main signal and local oscillator beams of the interferometer by the difference in their transit times through the interferometer.

A suitable time dependent sweep of the laser frequency causes the scattered light arriving at the detector to have a different frequency than the local oscillator beam simultaneously arriving at the detector, but causes no such shift for the signal beam as it follows a path length equal to that of the local oscillator. This frequency sweep causes the beat frequency between the stray light and the local oscillator to be shifted while leaving that of the signal beam and the local oscillator unchanged. The sweep rate of the laser is chosen so that the noisy region of the stray light spectrum is shifted outside of the measurement band.

For light scattered and trapped in the delay lines of the interferometer the minimum excess distance traveled is one round trip of the delay line,  $2L$ , corresponding to a travel time of  $\frac{2L}{c}$ . Thus a time rate of change in the laser frequency of  $\dot{f}$  produces a frequency difference of at least

$$\Delta f \geq \dot{f} \frac{2L}{c} \quad (4.51)$$

between the scattered light and the local oscillator. This frequency difference shifts the noise spectrum of the stray light. There is a frequency,  $f_{sc,max}$ , beyond which the stray light noise spectrum does not limit the sensitivity of the interferometer, and there is a maximum frequency to the interferometer measurement band,  $f_{int,max}$ . The frequency shift,  $\Delta f$ , of the scattered light must be large enough to shift the highest negative-frequency noise sidebands above the interferometer high-frequency cutoff

$$\Delta f \geq f_{sc,max} + f_{int,max} \quad (4.52)$$

This requires the sweep rate of the frequency,  $\dot{f}$  to be

$$\dot{f} \geq \frac{c}{2L}(f_{sc,max} + f_{int,max}) \quad (4.53)$$

Since the laser frequency cannot be swept indefinitely, it is necessary to use a periodic waveform. The optimal waveform is triangular so that the frequency shift of the stray light relative to the local oscillator is constant as the frequency is swept up and down. At the turning points of the waveform within twice the excess travel time

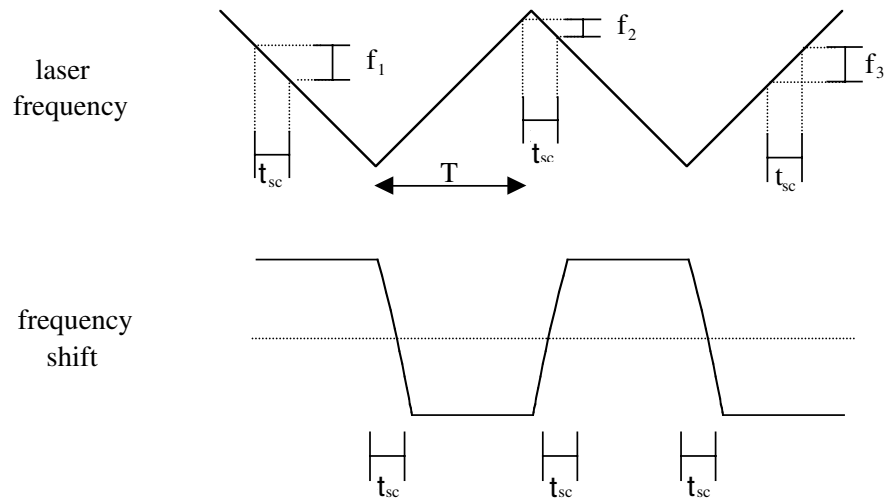


Figure 4.8: The ideal modulation waveform for the slow laser frequency sweep and the frequency shift it produces for stray light with a fixed delay time,  $t_{sc}$ .

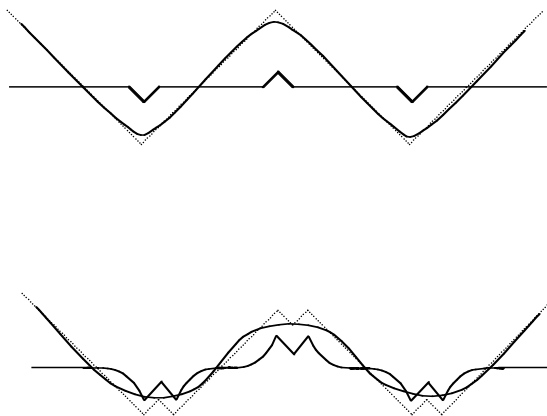


Figure 4.9: The modulation waveform for the slow laser frequency sweep with a finite bandwidth. To keep the slope of the waveform constant a fast actuator complements the slow actuator. The resulting waveform has  $k$  turning points per period.

of the stray light, the relative frequency shift of the stray light is reduced and passes through zero, reducing the fraction of time the stray light noise is shifted outside of the measurement band. For longer stray light delays the time that the stray noise is not shifted outside of the frequency band of interest increases. The rate that the laser frequency must be tuned, however, decreases allowing a longer period of time when the light is shifted outside of the frequency band of interest. Hence the fraction,  $x$ , of time the stray light noise is shifted outside of the measurement band is independent of the stray light delay and represents the performance of the modulation scheme. For an ideal modulation waveform it is

$$x = \frac{T - \tau_{sc}}{T} = 1 - \frac{f_{sc,max} + f_{int,max}}{\Delta f_{max}} \quad (4.54)$$

where  $\Delta f_{max}$  is the maximum dynamic range over which the laser frequency can be tuned and  $T$  is the half period of the triangular waveform. For a Nd:YAG laser the output frequency is tunable over a large dynamic range of about 50 GHz at a bandwidth of less than 1 Hz by controlling the laser crystal temperature and over a smaller dynamic range of about 30 MHz with a bandwidth up to 100 kHz by stressing the laser crystal to produce birefringence. To reach the performance specified by equation 4.54 it is necessary that the frequency tuning waveform be triangular, with linear slopes for times exceeding one stray light delay away from the turning points. If the dynamic range of the fast actuator is sufficient,

$$\Delta f_{max,fast} \geq \frac{c}{2L} \frac{f_{int,max} + f_{sc,max}}{f_{bw,slow}}, \quad (4.55)$$

the high frequency components of the triangle wave can be provided by the fast actuator. If the dynamic range of the fast actuator is less than this value it becomes necessary to construct a separate, smaller-dynamic-range triangular waveform for the fast actuator to drive while the slow actuator is rolling off. This introduces  $k$  extra turning points in the waveform, where  $k$  is the number of times the dynamic range is smaller than that required by equation 4.55. The performance of the modulation

scheme can be written generally for non-ideal modulation waveforms as

$$x = \frac{T - \tau_{sc}}{T} = 1 - k \frac{f_{sc,max} + f_{int,max}}{\Delta f_{max}} \quad (4.56)$$

where

$$k = \max \left[ 1, \frac{c}{2L} \frac{f_{int,max} + f_{sc,max}}{\delta f_{fast} f_{bw,slow}} \right] \quad (4.57)$$

For a delay-line Sagnac interferometer used in a gravitational wave detector with  $L = 4km$ ,  $f_{int,max} = 1kHz$  and  $f_{sc,max} = 3kHz$  and an amplified master oscillator with slow frequency tuning range of  $50GHz$  and a fast frequency tuning range of  $30MHz$  the performance of the modulation scheme is

$$x = 1 - 5 \times 10^{-7} \quad (4.58)$$

meaning that the noise produced by stray light can be completely removed from the measurement band for all but  $4ms$  of every 15 minute modulation period.

We have experimentally demonstrated the shifting of the stray light noise frequency. The spectrum of the output of a delay line Sagnac interferometer was measured with a phase modulation at 1.25 MHz imposed on the input light and a thin wire placed in the optical beam inside of the delay line to introduce scatter. The interference of the stray light with the local oscillator converts the phase modulation into amplitude modulation at the output. By sweeping the laser frequency through  $5GHz$  with a 10 second period we were able to shift the noise frequency by over  $100kHz$ .

This large-amplitude slow laser frequency sweep provides a simple way to reduce the effects of scattered light. Unlike the small-amplitude high-frequency modulation techniques described in Appendix A, the modulation waveform can be easily achieved without placing crystal modulators in the path of the laser beam, and without using difficult-to-generate high-voltage high-frequency waveforms to drive the modulators.

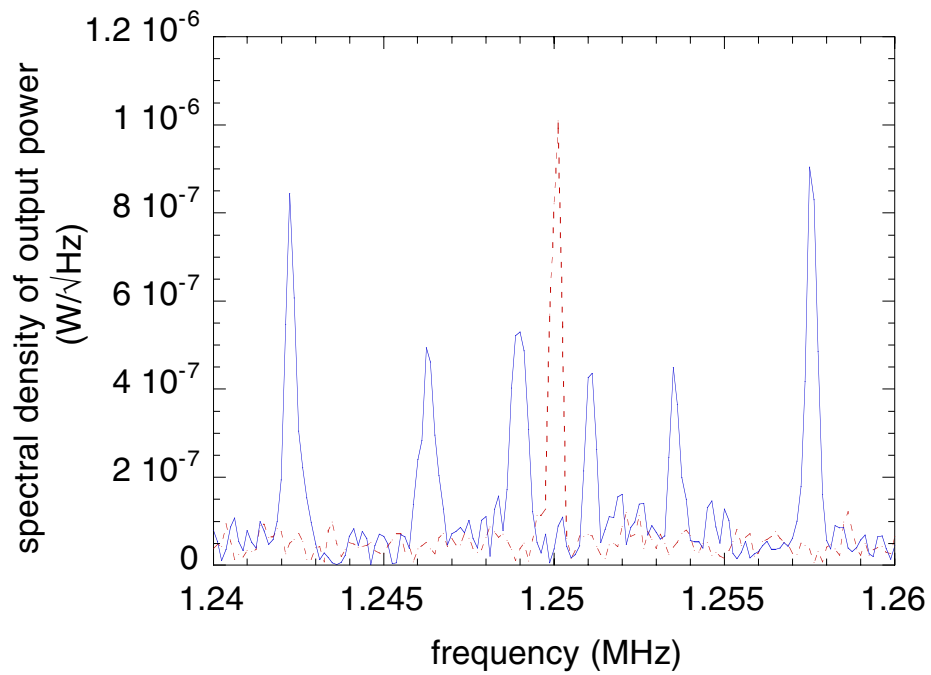


Figure 4.10: Scattered light noise introduced at 1.25 MHz with and without a laser frequency sweep to shift the noise away from its original frequency. Without the laser frequency sweep (dotted curve) low frequency motion of the scatterer produces noise around the 1.25 MHz modulation frequency. With the laser frequency sweep (solid curve) this noise is shifted to frequencies away from the 1.25 MHz modulation.

### 4.3 Conclusion

In conclusion, delay lines are necessary to increase the storage time of the interferometer arms without compromising the common path nature of the Sagnac interferometer. Because the reflection spots are on the perimeter of the mirror and must be well separated, delay lines require large mirrors. Additionally light with a wavelength of 532 nm or less is necessary to keep diffraction small enough so that enough spots can fit on the large mirrors to tune the peak response of the Sagnac interferometer well into the measurement band. Phase noise imposed by thermally driven motion of the mirror is likely less than that imposed by comparable motion of mirrors of a Fabry-Perot cavity. Large out-of-band motion of the mirrors (with amplitude on the order of an optical wavelength), however, can produce noise that is upconverted by scattered light into the measurement band. A new method to reduce scattered light noise has been described and experimentally demonstrated. Using a slow frequency sweep of the laser, we have shifted scattered light out of the measurement band. For a LIGO-scale 4 km delay line, the required frequency sweep is 150 MHz/s.

# Chapter 5

## Alignment tolerances

The common path of the beams in an ideal polarization Sagnac interferometer makes it insensitive to common mode noise sources such as laser frequency and amplitude noise, and also reduces its sensitivity to out of band noise such as mirror drift. These characteristics reduce the demand on the laser and seismic isolation system's performance. In this chapter the alignment and control requirements of the polarization Sagnac interferometer and a Fabry-Perot Michelson interferometer are calculated and compared. The intent is to characterize the control effort necessary for the polarization Sagnac interferometer and point out the tradeoffs offered relative to Michelson based interferometers. The parameters discussed include the interferometer's tolerance to noise coupled through mirror pitch, mirror yaw, longitudinal mirror position, transverse mirror position, laser amplitude noise, laser frequency noise, input polarization state, internal loss, and internal depolarization. Limits are placed on the value of these parameters to keep the overall noise within a factor of two of an ideal interferometer that is well-aligned and controlled. The seismic noise filtered through the suspension system, thermal noise of the mirrors, and quantum noise of the light are the dominant noise sources in the well-aligned interferometer. Table 5.6 at the end of this chapter provides a direct comparison between the control efforts of the two interferometer topologies.

## 5.1 Parameters for the alignment calculations

For comparison, two specific interferometer configurations based on the Michelson interferometer and the Sagnac interferometer have been considered. Neither configuration represents an actual design that has been proposed for an advanced LIGO detector, but rather are reference designs that contain many of the elements that would likely be included in an actual implementation an advanced LIGO detector.

The alignment and control effort of the interferometer is determined assuming there are 10 dominant sources of noise coupling into the output signal, each of which has an equal contribution so that the tolerable noise contribution from each is given by

$$\tilde{P}_i(\omega) \leq \frac{1}{\sqrt{10}} \tilde{P}_{ne}(\omega) \quad (5.1)$$

where  $\tilde{P}_i(\omega)$  is the noise power generated by the  $i^{th}$  noise source, and  $\tilde{P}_{ne}(\omega)$  is the noise equivalent power spectrum of an ideal interferometer that has a phase sensitivity of  $\tilde{\phi}(\omega) = 10^{-12} rad/\sqrt{Hz}$  at 100 Hz for a strain sensitivity of  $h = 10^{-23}/\sqrt{Hz}$ .

### 5.1.1 Power recycled Fabry-Perot Michelson interferometer

The Power Recycled Fabry-Perot Michelson interferometer has a small nominal path length difference between the two arms, used for generating a length sensing and control signal [70][71]. The path length asymmetry is a function of the modulation frequency used for generating the control signal. For this analysis a path length asymmetry of 40 cm and a modulation frequency of 25 MHz is used. Figure 5.1.1 shows the coupled cavities that enhance the interferometer sensitivity. The energy storage in the arms is increased by the resonant Fabry-Perot cavities with a power buildup of 50. The curvature of the Fabry-Perot mirrors is 10 km, their separation is 4 km, and the arm cavity reflectivities are matched to be within 0.01 of each other. The interferometer is biased so that the output port is dark for the carrier, but bright for the local oscillator sidebands. A power recycling mirror on the input port resonantly enhances the power circulating in the interferometer by a factor of 50. A laser wavelength of 1064 nm is used so that the absorption of light in the transmissive

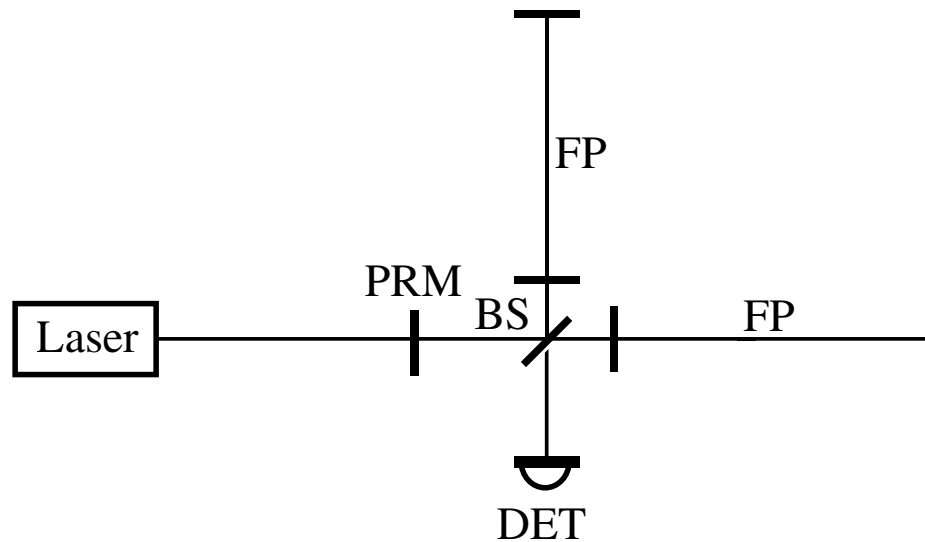


Figure 5.1: The power recycled Fabry-Perot Michelson interferometer. Critical elements include a power recycling mirror (PRM) a 50-50 beamsplitter (BS) and mirrors to form two Fabry-Perot cavities (FP) in the arms of the interferometer. The length of the Fabry-Perot cavities is assumed to be identical but the distance between the beamsplitter and the input couplers are assumed to be different by 40 cm. Not shown is a path for a portion of the input beam to be separated and mixed with the interferometer output on the detector to act as a local oscillator for homodyne or heterodyne detection.

optics is kept small.

### 5.1.2 Polarization Sagnac interferometer

The polarization Sagnac interferometer has delay lines with 51 round trips of the light in each arm. Figure 5.1.2 shows the layout of the optics in the polarization Sagnac interferometer. The delay line mirrors are near confocal, so both their curvature and their separation is 4 km. A wavelength of 532 nm is chosen to reduce the diffraction of the beam relative to 1064 nm light so that all 51 spots can be accommodated on the 1 m diameter delay line mirrors.

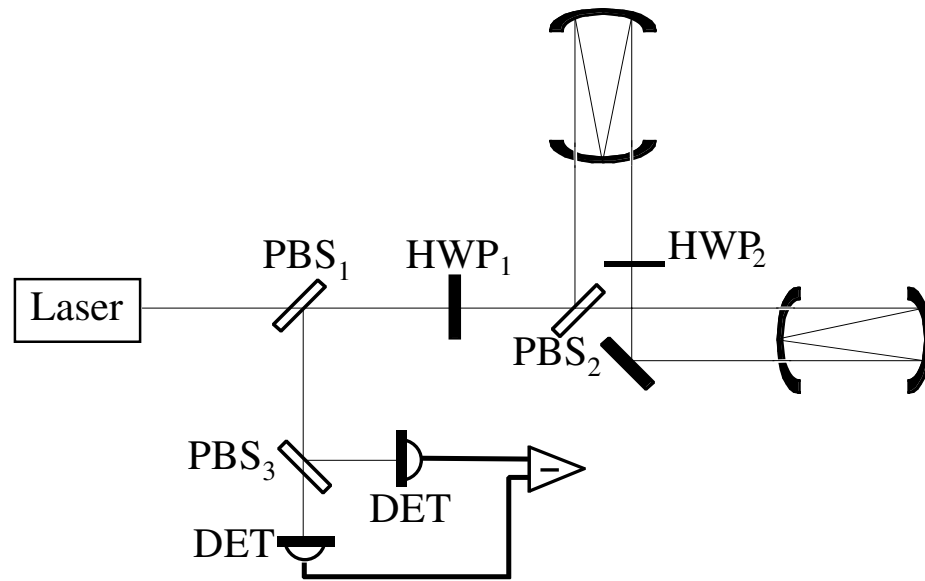


Figure 5.2: The delay-line polarization Sagnac interferometer. Critical elements include a polarizing beamsplitters (PBS) halfwave plates (HWP) and mirrors to form two delay-lines in the arms of the interferometer. Not shown is the phase modulator that adds heterodyne sidebands to the local oscillator polarization.

## 5.2 Alignment and stability of core optics

Motion of the core optics in the various degrees of freedom affect the position of the reflecting surfaces thereby affecting the phase of the output beams of the interferometer. It is therefore necessary to first determine the phase noise produced by longitudinal motion of the optical surfaces and then to determine the coupling of the other degrees of freedom into longitudinal motion at the reflection spots.

### 5.2.1 Sensitivity to mirror tilt

Mirror tilt noise couples into the interferometer signal through displacement of the reflection spots from the center of the mirror. The reflection spots on the delay line mirrors, being near the perimeter of the mirror, move in the longitudinal direction when the mirror is rotated about the x or y axis producing phase noise on the beam. For each spot moving inwards, however, the spot opposite it on the mirror is moving outwards, so the first order effect of tilt noise is cancelled if the spot pattern is

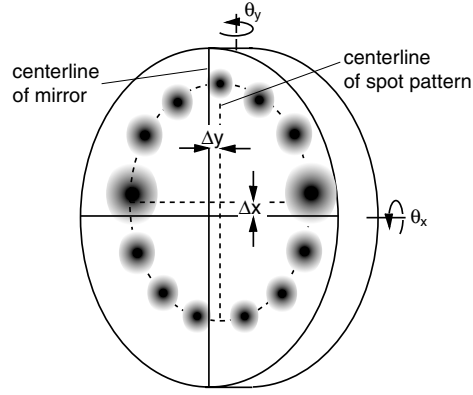


Figure 5.3: The displacement of the center of the spot pattern relative to the mirror center allows tilt noise to couple into the signal. Offset of the center of the spot pattern together with a tilted mirror couples pointing noise of the laser and tilt noise of the optic into phase noise at the interferometer output.

centered. In the Fabry-Perot there is also no first order sensitivity to mirror tilt when the spots are centered. The coupling of tilt noise through the beam offset is considered and used to set the requirements on the beam offset in the presence of the expected levels of thermal tilt noise. From the requirement on spot positioning, the angular deviation of the laser beam and of the other mirrors that steer the light onto the mirror, can be determined. Displacement and tilt in both transverse directions are degenerate so we consider only the total radial displacement of the center of the reflection spot in the Fabry-Perot or the center of the spot pattern from the center of the mirror in a delay line and the total tilt,

$$d = \sqrt{\Delta x^2 + \Delta y^2} \quad (5.2)$$

and

$$\theta = \sqrt{\theta_x^2 + \theta_y^2} \quad (5.3)$$

For the Fabry-Perot the excess phase accumulated by a beam when tilt noise is present is

$$\Delta\phi(t) = \tan^{-1} \left( \sum_{n=1}^{\infty} r^n e^{ik_0 d \theta (t - 2nL/c)} \right) \quad (5.4)$$

where  $r$  is the field reflection coefficient of the input coupler and the far mirror is assumed to have unity reflection. This gives a power spectral density of phase noise of

$$\tilde{\phi}(\omega) = \frac{k_0 d \tilde{\theta}(\omega)}{1 - r e^{-2i\omega L/c}} \quad (5.5)$$

For a delay line, since the consecutive reflection spots on a mirror are nearly  $180^\circ$  apart, the phases accumulated on consecutive reflections from a tilting mirror are opposite in sign. The total phase difference between two beams travelling in opposite directions through the interferometer is

$$\Delta\phi(t) = 2k_0 d \left( \sum_{n=1}^N (-1)^n \theta(t - 2nL/c) - \sum_{n=1}^N (-1)^n \theta(t - 4NL/c + 2nL/c) \right) \quad (5.6)$$

where  $N$  is the total number of round trips in the delay line, and the  $(-1)^n$  term accounts for the change in sign for each consecutive reflection.

The spectral density of phase noise due to mirror tilt is given by

$$\Delta\phi(\omega) = 4ik_0 d \int_{-\infty}^{\infty} \tilde{\theta}(\omega) e^{i\omega t} e^{-2i\omega N\tau} \left( \sum_{n=1}^N (-1)^n \sin(2\omega(N-n)\tau) \right) d\omega \quad (5.7)$$

The sum can be separated into a sum over odd numbered bounces and a sum over even numbered bounces. For  $2\omega L/c \ll \pi$  they can be approximated by integrals giving

$$\begin{aligned} \Delta\phi(\omega) &\approx 2ik_0 d \int_{-\infty}^{\infty} \tilde{\theta}(\omega) e^{i\omega t} e^{-2i\omega NL/c} \\ &\times \left( \int_{\nu=1}^N \sin(2\omega(N-\nu)L/c) d\nu - \int_{\nu=2}^{N-1} \sin(2\omega(N-\nu)L/c) d\nu \right) d\omega \end{aligned} \quad (5.8)$$

that evaluates to

$$\begin{aligned} \Delta\phi(\omega) &= 2ik_0 d \int_{-\infty}^{\infty} \tilde{\theta}(\omega) e^{i\omega t} e^{-2i\omega NL/c} \times \\ &\left( 1 - \cos(2\omega(N-1)L/c) - \cos(2\omega L/c) + \cos(2\omega(N-2)L/c) \right) d\omega, \end{aligned} \quad (5.9)$$

for the phase difference between the two beams of a delay-line Sagnac interferometer due to mirror tilt. In the measurement band,  $\omega L/c \ll \pi$ . The finite difference between cosine functions can be approximated by the derivative. With this approximation the phase noise due to mirror tilt in a delay line is

$$\tilde{\phi}(\omega) = 8k_0 d \cos((N-1)\omega\tau) \sin((N-2)\omega\tau) \tilde{\theta}(\omega) \quad (5.10)$$

Assuming the suspension systems provides a level of isolation to tilt noise comparable to its longitudinal isolation, the dominant source of mirror tilt noise is thermal noise of the core optic substrate tilting the reflecting surface of the optic. For an optic with a material loss  $\Phi(\omega)$  and a moment of inertia  $I$  about the suspension axis the thermal noise in the tilt mode has a magnitude of

$$\tilde{\theta}(\omega)_{thermal} = \sqrt{\frac{4kT\omega_0^2\Phi(\omega)}{I\omega^5}} rad/\sqrt{Hz}. \quad (5.11)$$

[72]

For a 1 m diameter, 30 cm thick silicon substrate ( $m=550$  kg,  $I=34$   $kgm^2$ ) with a material loss of  $\Phi = 10^{-7}$  in the frequency range corresponding to the gravitational wave measurement band, the thermal noise in the tilt mode at 100 Hz is  $\tilde{\theta}_{thermal}(\omega) = 1.6 \times 10^{-17} rad/\sqrt{Hz}$ . with this level of tilt noise the spots pattern on the delay line must be centered on the mirror to within  $d < 1.7$  mm according to 5.10 while for the Fabry-Perot the spots must be centered to within  $d < 0.2$  mm.

For the delay line, this tolerance requires the angular deviation of the other mirror a distance  $L$  away, be less than

$$\theta < \frac{d}{L} = 430 \times 10^{-9} rad \quad (5.12)$$

while for the Fabry-Perot

$$\theta < \frac{d}{L} = 50 \times 10^{-9} rad \quad (5.13)$$

### 5.2.2 Sensitivity to mirror translation

Translational motion of the mirrors produces a displacement of the reflecting surface either directly through longitudinal motion of the mirror, or by transverse motion coupling to longitudinal motion through the curved surfaces of the mirrors. The coupling of transverse motion to longitudinal motion is given by the orientation of the mirror surface at the reflection spot – a function of the shape and alignment of the mirror. The positioning requirement is determined, for the Fabry-Perot Michelson interferometer based on the need to keep the arm cavities resonant, and for the polarization Sagnac interferometer based on the need to meet the re-entrance condition for the delay lines.

Both the Fabry-Perot and the delay line mirrors' surfaces are spherical and hang parallel slightly out of the vertical planes which are non-parallel due to the curvature of the earth over the long baseline. The angle between the mirrors' local verticals is  $2\theta_v = \frac{L}{R_e}$  where  $R_e = 6.38 \times 10^6 m$  is the radius of the earth. Thus the angle between the vertical suspensions and the average vertical direction is  $\theta_v = \frac{L}{R_e}$ . With this angle the mirror surfaces can be described in their local coordinate frames by

$$z = \frac{x^2}{2R} + \frac{y^2}{2R} + \frac{L}{R_e}y \quad (5.14)$$

where  $R$  is the radius of curvature of the spherical mirrors and it is assumed that for any points on the mirror surface  $x, y \ll R, R_e$ . In this description the origin is at the center of the mirror,  $z$  is the direction of the optical axis,  $x$  is the horizontal transverse direction and  $y$  is the nearly vertical transverse direction.

#### Vertical motion

Consider first the coupling of vertical motion to the longitudinal direction. For  $R_e \gg R$  the coupling of vertical motion into longitudinal motion is

$$dz \approx \frac{L}{R_e}dy. \quad (5.15)$$

For a beam in a Fabry-Perot cavity, fluctuations in the vertical position of a mirror add a phase of

$$\phi(t) \approx \sum_{n=1}^{\infty} r^n 2k_0 \frac{L}{R_e} \Delta y(t - 2\omega n L/c) \quad (5.16)$$

so that the Fabry-Perot has a phase noise due to vertical mirror motion of

$$\tilde{\phi}(\omega) = 2ik_0 \frac{L}{R_e} \frac{1}{1 - r e^{-2i\omega L/c}} \Delta \tilde{y}(\omega), \quad (5.17)$$

This requires  $\tilde{y}(\omega) < 3.1 \times 10^{-18} \text{ m}/\sqrt{Hz}$  at 100 Hz.

In a delay line with fluctuations in the vertical position of one mirror, a beam acquires an excess phase of

$$\phi(t) = 2k_0 \frac{L}{R_e} \sum_{n=1}^{N-1} \Delta y(t - 2\omega n L/c) - 2k_0 \frac{L}{R_e} \sum_{n=1}^{N-1} \Delta y(t - 4NL/c - 2\omega n L/c). \quad (5.18)$$

Since the frequencies of interest are low compared to the inverse single pass travel time of the arm,  $\omega L/c \ll 1$ , this sum, when expressed in the frequency domain, can be approximated by the integral

$$\tilde{\phi}(\omega) = 4ik_0 \frac{L}{R_e} \widetilde{\Delta y}(\omega) e^{i\omega NL/c} \sin(\omega NL/c) \int_1^{N-1} \exp(2i\omega \nu L/c) d\nu. \quad (5.19)$$

The differential phase due to vertical motion of the delay line mirror, when evaluated and added to the excess phase of the counterpropagating beam, gives

$$\tilde{\phi}(\omega) = \frac{4k_0 L}{\omega \tau R_e} \sin(2(N-2)\omega \tau) \sin(\omega L/c) \tilde{y}(\omega) \quad (5.20)$$

requiring  $\widetilde{\Delta y}(\omega) < 41.0 \times 10^{-18} \text{ m}/\sqrt{Hz}$  at 100 Hz.

### Horizontal motion

For *horizontal* motion of the mirrors the additional phase accumulated on each reflection depends on the position of the reflection spot relative to the center of the

mirror,

$$dz = \frac{x}{R} dx. \quad (5.21)$$

In a Fabry-Perot cavity this results in a phase noise spectrum similar to equation 5.17 but with  $L \rightarrow x$  and  $R_e \rightarrow R$  giving

$$\tilde{\phi}(\omega) = 2ik_0 \frac{x}{R} \frac{1}{1 - re^{-2i\omega L/c}} \Delta\tilde{x}(\omega). \quad (5.22)$$

The horizontal motion of the mirror must be controlled to  $\tilde{x}(\omega) < 2.0 \times 10^{-14} \text{ m}/\sqrt{Hz}$  at 100 Hz for spot displacements from the center of the mirror of 0.1 mm, as constrained by equations 5.5 and 5.10.

Horizontal motion of a delay line mirror adds and subtracts phase from the beam at alternating reflection spots. The phase noise due to transverse mirror motion is found in an equivalent manner to the derivation of equation 5.10 with the substitutions

$$d \rightarrow x \quad (5.23)$$

and

$$\tilde{\theta} \rightarrow \frac{\widetilde{\Delta x}}{R} \quad (5.24)$$

giving

$$\tilde{\phi}(\omega) = 8k_0 \frac{x}{R} \cos((N-1)\omega L/c) \sin((N-2)\omega L/c) \Delta\tilde{x}(\omega). \quad (5.25)$$

This requires  $\tilde{\Delta x}(\omega) < 1.0 \times 10^{-12} \text{ m}/\sqrt{Hz}$  at 100 Hz for a beam displaced from the center of the mirror by no more than  $d = 0.1 \text{ mm}$ .

### Longitudinal motion

For direct *longitudinal* motion of the mirror the phase accumulated at the reflection spots add. For a Fabry-Perot near resonance, this produces an excess phase of

$$\phi(t) \approx \sum_{n=1}^{\infty} 2r^n k \Delta z(t - nL/c) \quad (5.26)$$

giving a spectral density of phase noise

$$\tilde{\phi}(\omega) = \frac{2k}{1 - r e^{i\omega L/c}} \Delta \tilde{z}(\omega). \quad (5.27)$$

This requires  $\tilde{z}(\omega) < 2.1 \times 10^{-21} \text{ m}/\sqrt{Hz}$  at 100 Hz.

In a delay line the excess phase due to longitudinal mirror motion is

$$\phi(t) = \sum_{n=1}^N 2k_0 z(t - 2nL/c) - \sum_{n=1}^N 2k_0 z(t - 2(N+n)L/c) \quad (5.28)$$

which gives a noise spectrum of

$$\tilde{\phi}(\omega) = \sin(\omega NL/c) \sum_{n=1}^N 4ik_0 \tilde{z}(\omega) e^{-i\omega(2n+N)L/c}. \quad (5.29)$$

The sum can be approximated by an integral so that equation 5.29 evaluates to

$$\tilde{\phi}(\omega) \approx \sin(\omega NL/c) 4k_0 \tilde{z}(\omega) \frac{c}{\omega L} e^{-i\omega L/c} \sin((N-1)\omega L/c). \quad (5.30)$$

This requires the longitudinal motion be constrained to  $\tilde{z}(\omega) < 5.5 \times 10^{-22} \text{ m}/\sqrt{Hz}$  at 100 Hz.

### Longitudinal position of the mirrors

The longitudinal *position* of the mirrors in the Fabry-Perot Michelson must be maintained to keep the interferometer on a dark fringe. For the dark port of the power recycled Fabry-Perot Michelson interferometer

$$P_{dp} = P_{bs} \sin(2\pi \Delta z / \lambda) \quad (5.31)$$

where  $P_{bs}$  is the power at the beamsplitter and  $\Delta z$  is the length offset. This requires

$$\Delta z_{rms} < \frac{\lambda P_{max}}{2\pi P_{bs}} \quad (5.32)$$

so that the dark port power remains below the maximum tolerable power  $P_{max}$ . Additionally a length offset of the Fabry-Perot cavities would decrease the power in one arm acting like a loss of magnitude

$$A_{eff} = 1 - \frac{P_r(\Delta z)}{P_r(0)}. \quad (5.33)$$

where

$$P_r(z) = \frac{P_0}{1 + F \sin(4\pi\Delta z/\lambda)} \quad (5.34)$$

is the power reflected from the Fabry-Perot cavity of finesse  $F$  and mirror spacing from resonance  $\Delta z$ . From the differential loss constraint

$$A < \frac{P_{max}}{P_{bs}} \quad (5.35)$$

required to keep the power on the dark port below  $P_{max}$ ,

$$\Delta z < \frac{\lambda P_{max}}{4\pi P_{bs} F} \quad (5.36)$$

which evaluates to  $\Delta z_{rms} < 1.6 \times 10^{-13}m$  for the reference design of the Fabry-Perot Michelson interferometer.

For the delay line Sagnac interferometer the only requirement on the longitudinal positioning of the mirrors comes from the need to meet the re-entrance condition on the delay line. The tangential position of the  $N^{th}$  spot on the delay line mirror is  $\theta = N \left(1 - \frac{L}{R}\right)$  so that a change in the position of a delay line mirror by  $\Delta L$  changes this angle by  $\Delta\theta = -N \frac{\Delta L}{R}$ . With the aperture diameter 2.5 times larger than the beam diameter at the output, at a change in angle of  $\Delta\theta = 1.25 \times 10^{-4}$  the intensity of the beam at the edge where it is clipped by the aperture changes by less than 1%, or a fraction of  $10^{-5}$  of the peak intensity of the beam. To keep the output beam centered on the output aperture at this level requires the mirror position to be held to  $\Delta z_{rms} < 1cm$ .

### 5.3 Sensitivity to laser noise

An ideal polarization Sagnac interferometer is highly insensitive to the common mode noise from the laser. Detection on the dark fringe of the interference and balanced detection ensure insensitivity to amplitude noise, while the common path of the interfering beams provide insensitivity to frequency noise. Stray light on the detector, such as that from scatter in the delay lines, however, breaks the symmetry of the interfering beams and provides coupling of frequency noise into the signal. The amount of coupling depends on the relative field strength of the stray light on the detector,  $\kappa$ , defined as

$$\kappa = \sqrt{\frac{P_{sl}}{P_o}}, \quad (5.37)$$

where  $P_{sl}$  the power of the stray light on the detector and  $P_o$  is the circulating power. The coupling also depends on the propagation time difference,  $\tau$ , between the local oscillator and the stray light. The interference of this stray light with the local oscillator is equivalent to the output of a Michelson interferometer superimposed on the output of the Sagnac and therefore provides a sensitivity to frequency and amplitude noise.

For the polarization Sagnac, laser frequency noise couples through the scattered light. The magnitude of the contribution is the given by the product of the fraction of scattered light reaching the detector, forming a ghost interferometer, with the conversion of laser frequency to amplitude noise by that ghost interferometer. The reference phase of the laser is treated as if it changes according to a gaussian probability-density function given by

$$P_\tau(\Delta\phi) = \frac{1}{\sqrt{2\pi\Delta\tau}} \exp\left(-(\Delta\phi)^2/2\Delta\tau\right) \quad (5.38)$$

where  $P_\tau(\Delta\phi)$  is the probability density that the phase changed by  $\Delta\phi$  in a time  $\tau$  and  $\frac{\delta}{2\pi}$  is the full linewidth in Hertz at the half power points [73]. The spectrum of relative

output intensity fluctuations for the ghost interferometer is given by Armstrong [74],

$$\frac{\tilde{P}(\omega)}{P_0} \approx \frac{4e^{-2\delta\tau}}{\delta} \left( \frac{\omega/\delta \sin(2\omega\tau)}{1 + (\omega/\delta)^2} - \frac{\sin(2\omega\tau)}{\omega/\delta} \right) \quad (5.39)$$

Reducing this by the relative amplitude of the ghost interferometer's signal,  $\kappa$ , gives an expression relating the detected phase noise to the laser linewidth

$$\tilde{\phi}(\omega) \approx \frac{4\kappa e^{-2\delta\tau}}{\delta} \left( \frac{\omega/\delta \sin(2\omega\tau)}{1 + (\omega/\delta)^2} - \frac{\sin(2\omega\tau)}{\omega/\delta} \right). \quad (5.40)$$

This requires the laser linewidth for the polarization Sagnac to be less than 1 kHz to meet the sensitivity requirement and advanced LIGO detector.

The polarization Sagnac interferometer's sensitivity to laser amplitude noise also comes from the scattered light. For an input field with amplitude noise such that

$$E(t) = E_0 \left( 1 + \tilde{E}(\omega) \sin(\omega t) \right) \quad (5.41)$$

and the polarization components of the return field given by

$$E_s(t) = E(t) \quad (5.42)$$

$$E_p(t) = E(t) + \kappa E(t - \tau) \quad (5.43)$$

where  $\kappa$  is the relative field amplitude of scattered light seen by one beam. The signal noise spectrum is equivalent to a system with phase noise of

$$\tilde{\phi}(\omega) = 2\kappa \sin(\omega\tau/2) \tilde{E}(\omega). \quad (5.44)$$

For a relative scattering amplitude of  $\kappa = 10^{-4}$ , the laser amplitude noise must be below  $\frac{\tilde{E}(\omega)}{E_0} \leq 5 \times 10^{-9}/\sqrt{Hz}$  at 100 Hz. With the frequency shifting scheme of section 4.2.3, however, this frequency stability only needs to be met between 3 kHz and 4 kHz rather than at low frequencies below 1 kHz.

This can be compared with the coupling of laser noise to the detected signal in the Fabry-Perot Michelson interferometer, found by Camp et al [75]. The coupling of

frequency noise is

$$\frac{\tilde{P}(\omega)}{\tilde{P}_{sn}(\omega)} = 2\sqrt{\frac{P_0}{\hbar\omega_0}} t_r G_r^c \frac{\pi A_{cm}}{\omega} \tilde{f}(\omega) \quad (5.45)$$

where  $\tilde{f}(\omega)$  is the spectral density of laser frequency fluctuations. For an advanced LIGO interferometer  $t_r \approx 0.2$  is the field transmission of the recycling mirror,  $G_r^s \approx 50$  is the power buildup in the recycling cavity of the RF sidebands used as the local oscillator, and  $A_{cm} \approx 0.005$  is the arm cavity carrier reflectivity mismatch. To meet the sensitivity goals for this detector the spectral density of laser frequency noise must be  $\tilde{f}(\omega) < 2.7 \times 10^{-8} \text{ Hz}/\sqrt{\text{Hz}}$  in the measurement band. This can be compared to the requirement on the laser linewidth for the polarization Sagnac interferometer by considering the relation between laser frequency noise and laser linewidth[76] given by

$$\tilde{f}(\omega) = \delta \sqrt{\frac{2\hbar\omega_0}{P}}. \quad (5.46)$$

The requirement on the laser frequency noise is equivalent to a requirement that the laser linewidth obey  $\delta < 420 \text{ Hz}$ .

The same analysis by Camp gives a requirement on laser amplitude noise in the Fabry-Perot Michelson interferometer of  $\frac{\tilde{E}(\omega)}{E_0} < 1 \times 10^{-8}/\sqrt{\text{Hz}}$  at 100 Hz.

## 5.4 Polarization effects

Both the Fabry-Perot Michelson interferometer and the polarization Sagnac interferometer are sensitive to polarization effects. The polarization Sagnac is sensitive to changes in the input polarization, while the Fabry-Perot Michelson interferometer is sensitive to polarization changes in the arms of the interferometer.

The polarization state of the output beam of the polarization Sagnac interferometer is found using Jones calculus. We represent the transmission and reflection of the polarizing beamsplitters as

$$\hat{P}_t = i \begin{bmatrix} 1 - x & 0 \\ 0 & x \end{bmatrix}, \quad (5.47)$$

and

$$\hat{P}_r = \begin{bmatrix} x & 0 \\ 0 & 1-x \end{bmatrix} \quad (5.48)$$

where  $x^2$  is the power extinction ratio. We represent a signal that differentially phase modulates the clockwise and counterclockwise beams by the signal matrices

$$\hat{S}_+ = \exp(i\Delta\phi/2) \begin{bmatrix} 1 & 0 \\ 0 & 1 \end{bmatrix}, \quad (5.49)$$

and

$$\hat{S}_- = \exp(-i\Delta\phi/2) \begin{bmatrix} 1 & 0 \\ 0 & 1 \end{bmatrix} \quad (5.50)$$

for the clockwise and counterclockwise propagating beams respectively where  $\Delta\phi$  is the magnitude of the differential phase modulation. The output electric field is

$$\vec{E}_{out} = \hat{H}_1 \left( \hat{P}_{2,t} \hat{S}_- \hat{H}_2 \hat{P}_{2,r} + \hat{P}_{2,r} \hat{H}_2 \hat{S}_+ \hat{P}_{2,t} \right) \hat{H}_1 \cdot \vec{E}_{in} \quad (5.51)$$

where  $\hat{H}_1$  and  $\hat{H}_2$  represent the halfwave plates  $HWP_1$  and  $HWP_2$  in figure 3.6. With a linearly polarized input field at  $0^\circ$  the expression for the output is

$$\vec{E}_{out} = \begin{bmatrix} i \cos \frac{\Delta\phi}{2} \left( (1-2x_2^2) \sin 4\theta_1 \sin 2\theta_2 + 2x_2 \sqrt{(1-x_2^2)} \cos 2\theta_2 \right) \\ \sin \frac{\Delta\phi}{2} \sin 2\theta_2 - i \cos \frac{\Delta\phi}{2} \left( (1-2x_2^2) \cos 4\theta_1 \sin 2\theta_2 \right) \end{bmatrix} |\vec{E}_{in}| \quad (5.52)$$

where  $\theta_1$  is the angle between  $HWP_1$ 's fast axis and the x-axis,  $\theta_2$  is the angle between  $HWP_2$ 's fast axis and the x-axis,  $x_1$  is the power extinction ratio of  $PBS_1$ ,  $x_2$  is the power extinction ratio of  $PBS_2$ , the x and y axes are defined by the polarization axes of the polarizing beamsplitters and all angles are measured in degrees. The field selected by the polarizing beamsplitter  $PBS_1$  for post modulation is

$$\vec{E}'_{out} = \begin{bmatrix} \sqrt{x_1} & 0 \\ 0 & \sqrt{1-x_1} \end{bmatrix} \vec{E}_{out} \quad (5.53)$$

with  $E_{out}$  calculated in equation 5.52.

The input polarization is set by the halfwave plate,  $HWP_1$  at an angle  $\theta_1$  nominally to  $45^\circ$  so that there is equal power in the counterpropagating beams. A misalignment

of the angle of the linear input polarization, or relative phase between the polarization components of the input beam,  $\theta_{in}$  causes an imbalance in the power of the interfering beams producing a background power level of

$$P_{out} = \sin^2(\theta_{in})P_{in} \quad (5.54)$$

on the detector. To avoid saturating the detector this should remain below a limit of 1 watt. Thus the input polarization must be aligned to  $\theta_{in} \leq 1.0 \times 10^{-2}$  rad. *Fluctuations* in the polarization angle couple to the output signal. Differentiating equation 5.54 gives

$$\tilde{P}_{out}(\omega) = 2 \sin(\theta_{in})\tilde{\theta}_{in}(\omega) P_{in}. \quad (5.55)$$

For an input polarization misalignment  $\theta_{in} = 1.0 \times 10^{-2}$  rad, this requires the fluctuations in the input polarization to be less than  $\tilde{\theta}(\omega) = 5 \times 10^{-11} rad/\sqrt{Hz}$

Birefringence in the polarization Sagnac interferometer arms has little effect on the interference of the circulating beams since both beams see the same elements. Any light converted out of the desired polarization state is removed by the polarizing beam splitter at the output of the interferometer, thereby acting like a loss.

In the Fabry-Perot Michelson the polarization of the interfering beams must be matched to avoid excess power on the detector. Any polarization changing elements in the arms of the interferometer must be well matched as well. The excess power on the photodetector due to unmatched polarization states in the interferometer is

$$P_{out} = \sin^2(\Delta\theta)P_{bs} \quad (5.56)$$

where  $P_{bs}$  is the power at the beamsplitter, for example, the laser power enhanced by the power recycling cavity. This requires the polarization rotation in the arms be less than  $\Delta\theta \leq 1.0 \times 10^{-2}$ . Additionally there is sufficient delay  $\Delta t$  between the transit time of the local oscillator in the interferometer, which does not resonate in the arm cavities, and the carrier light, which does, to efficiently couple fluctuations of the input polarization angle in the measurement band to power at the detector.

The coupling produces noise of

$$\tilde{P}_{out}(\omega) = 2 \sin(\theta_{in}) \sin(\omega\Delta t) \tilde{\theta}_{in}(\omega) P_0 \quad (5.57)$$

so that at frequencies where  $\omega\Delta t = \frac{\pi}{2}$  the requirement on the input polarization noise of the Fabry-Perot Michelson is equivalent to that of the polarization Sagnac interferometer of relation 5.55.

From this analysis it is clear that the requirements on polarization for the polarization Sagnac and the Fabry-Perot Michelson interferometer are similar, with the polarization Sagnac requiring only the *input* polarization be controlled and the Fabry-Perot Michelson requiring only the differential polarization *in the arms* be controlled.

## 5.5 Internal loss

The polarization Sagnac interferometer is quite insensitive to loss since loss affects both interfering beams equally. The Fabry-Perot Michelson interferometer, however, requires both interfering beams be matched in amplitude, and therefore must have well matched losses in each of the interferometer arms. The residual power on the detector when the power from the two arms of the Fabry-Perot Michelson interferometer are unmatched is

$$P_{dp} = P_{bs} \Delta a \quad (5.58)$$

where  $\Delta a$  is the differential loss in the otherwise well matched interferometer arms. Assuming the differential loss is 1% of the total loss and that the detector can only handle 1 W of excess power, requires  $a < 40ppm$ .

## 5.6 Summary of alignment and control requirements

The alignment and control requirements of the polarization Sagnac Interferometer and the power-recycled Fabry-Perot Michelson interferometer have a few significant

differences. For the power-recycled Fabry-Perot Michelson interferometer, the absolute longitudinal positioning requirement for the mirrors is difficult to achieve or maintain and position offsets yield cross-couplings to other control factors. For the delay-line polarization Sagnac interferometer, the lack of coupled cavities in the interferometer makes achieving and maintaining the longitudinal position of the mirrors relatively easy. Additionally the Fabry-Perot Michelson interferometer requires the losses in the interferometer arms to be very well matched, demanding uniformity of the optics beyond what current manufacturing processes regularly achieve for fused silica, and well beyond what new manufacturing processes for sapphire will be able to reach. The polarization Sagnac interferometer, however, does not recycle light and therefore requires much greater laser power than the Fabry-Perot Michelson. The need for many bounces in the delay line arms of the polarization Sagnac interferometer requires efficient harmonic generation from the fundamental wavelength of solid-state lasers such as Nd:YAG or Yb:YAG. The comparisons of the requirements for the two configurations can be seen in table 5.6

	Fabry-Perot Michelson	delay-line Sagnac
Mirror Pitch	50 nrad	430 nrad
Mirror Yaw	50 nrad	430 nrad
Mirror Roll		
Vertical Mirror Stability	$3.1 \times 10^{-18} m/\sqrt{Hz}$	$41 \times 10^{-18} m/\sqrt{Hz}$
Horizontal mirror stability	$2.0 \times 10^{-14} m/\sqrt{Hz}$	$100 \times 10^{-14} m/\sqrt{Hz}$
longitudinal mirror stability	$21 \times 10^{-22} m/\sqrt{Hz}$	$5.5 \times 10^{-22} m/\sqrt{Hz}$
longitudinal mirror positioning	$10^{-13}$ m rms	1 cm rms
laser irradiance	200 W @1064 nm	10 kW @ 532 nm
laser amplitude stability	$10 \times 10^{-9}/\sqrt{Hz}$	$5.0 \times 10^{-9}/\sqrt{Hz}$
laser linewidth	420 Hz	6300 Hz
input polarization	-	$10^{-2} rad$
internal depolarization	$10^{-2} rad$	-
internal loss	40 ppm	-

Table 5.1: A comparison of the alignment and control requirements for the power recycled Fabry-Perot Michelson interferometer and the delay line polarization Sagnac interferometer. The requirements listed are necessary for the detector to have a phase sensitivity of  $\tilde{\phi}(\omega) = 10^{-12} rad/\sqrt{Hz}$  at 100 Hz, which is necessary to reach a strain sensitivity of  $h = 10^{-23}/\sqrt{Hz}$ .

# Chapter 6

## Scaling to High-Power

Advanced interferometers, such as LIGO III, require several kilowatts of circulating power for a quantum-noise limited sensitivity of  $h = 10^{-23}$ . Generation and handling of such high power is technically very challenging. Kilowatt class laser designs based on Yb:Yag have been proposed but their development is held back by the cost of the pump laser diodes. It is likely that the falling price of laser diodes will make kilowatt power solid-state lasers a reality within the next decade. Such high laser power, however, will lead to thermal distortions and thermal lensing in transmissive optics limiting the useful power. These thermal effects can be nearly eliminated by avoiding transmissive optics in the interferometer. The use of reflective optics not only eliminates power losses in the bulk substrates, but also allows substrate materials which are not optically transparent to be considered. In this chapter I present the motivation for using an all-reflective optics in the interferometer, a model for the effect of thermal distortions from reflective optics, and experimental results for a 10 m suspended optics all-reflective polarization Sagnac interferometer.

### 6.1 Thermal distortions

Thermal distortions arise from non-uniform heating of an optic at the surface or in the bulk. A Gaussian beam transmitting through an optic heats the surfaces and the bulk with a Gaussian profile. In the steady state the heat diffuses outward to the surfaces of

the optic and is radiated away. This temperature profile causes non-uniform expansion of the substrate resulting in a change in the shape of the optical surfaces (thermoelastic deformation) and, through the temperature dependence of the refractive index, a gradient index lens in the substrate (thermal lensing). The absorption coefficients of the coatings and the substrate material determines the fraction of laser power which heats the substrate. The thermal conductivity of the substrate material governs the uniformity of the temperature profile, and material properties such as Young's Modulus, Poisson's ratio, and the temperature dependence of the refractive index determines the magnitude of the thermal distortions.

When power is absorbed in an optic the thermal expansion causes a change of the sagitta of the optical surface. For a mirror this changes the effective radius of curvature of the optic. For a beamsplitter it creates a lens. The sagitta is the curvature depth of the mirror across the beam diameter. It can be approximated by  $s \approx \frac{\omega^2}{2R}$ . For mirrors with nearly confocal spacing,  $\omega \approx \sqrt{\frac{\lambda R}{\pi}}$ , this becomes  $s \approx \frac{\lambda}{2\pi}$ . For a cavity to remain stable, thermal distortion must be smaller than the sagitta. Winkler et. al. [77] have approximated the change in sagitta due to power absorption by

$$ds \approx \left[ \frac{\alpha/\kappa}{4\pi} (a_{coatings} + a_{bulk}) + \frac{\beta/\kappa}{4\pi} a_{coatings} + 1.3 \frac{\beta/\kappa}{4\pi} a_{bulk} \right] P_{inc} \quad (6.1)$$

where  $\alpha$  is the thermal expansion of the substrate material,  $\beta = dn/dt$  is the first order dependence of the index of refraction of the substrate material,  $\kappa$  is the thermal conductivity of the substrate material.  $a_{bulk}$  is the fractional power absorption for light transmitting through the substrate of the substrate material and  $a_{coating}$  is the fractional power absorbed by the optical coating. This approximation is used in table 6.1 to determine the power handling limit of an interferometer based on the optical and thermal properties of the core optics. Long cavities with several kilowatts of circulating power operate at the threshold of stability. Controlling interferometers with such cavities may not be possible, particularly when the cavity power is building up and dynamic thermal distortions are present during the acquisition of lock.

Table 6.1: Absorption coefficients and material parameters of some relevant optical materials. The power level that produces thermal distortions equal to the sagitta of confocally spaced mirrors separated by 4 km is given, as is the shot noise sensitivity level of an interferometer illuminated with that power level. A coating absorption of 1 ppm is assumed for all materials.

Material at 300 K	Lensing $\frac{\beta}{\kappa} (\frac{nm}{W})$	Expansion $\frac{\alpha}{\kappa} (\frac{nm}{W})$	Absorption ( $cm^{-1}$ )	Power Limit (W)	Sensitivity Limit ( $/\sqrt{Hz}$ )
<b>Transmissive</b>					
Sapphire	19	147	$4 \times 10^{-4}$	130	$80 \times 10^{-24}$
Fused Silica	17	370	$1 \times 10^{-3}$	$2 \times 10^3$	$20 \times 10^{-24}$
<b>Reflective</b>					
Sapphire	-	147	-	$300 \times 10^3$	$0.16 \times 10^{-24}$
Fused Silica	-	370	-	$120 \times 10^3$	$2.6 \times 10^{-24}$
Silicon	-	18	-	$2.5 \times 10^6$	$0.07 \times 10^{-24}$

Thermal distortions can be significantly reduced by using reflective optics to eliminating bulk absorption. Reflective optics also allow opaque materials such as silicon to be considered that have excellent thermal and mechanical properties. LIGO II will likely use some form of active thermal compensation to reduce the effects of thermal distortion potentially allowing up to 10 times more laser power to be used than without compensation. For detectors beyond LIGO II, however, it is unlikely that active compensation will be sufficient to allow the thermally loaded interferometer to operate. An all-reflective configuration is needed. We therefore consider in greater detail the effect of thermal deformations on reflective optics used as mirrors and reflective gratings[78] as beamsplitters and cavity input-output couplers.

We use the thermal analysis of Hello and Vinet[79] cast in a non-dimensional form that allows the magnitude of the thermal distortions to be approximated by an expression that is only a function of the substrate's material properties and the absorbed laser power.

For power absorption at the surfaces of a cylindrical substrate the thermal diffusion equation is

$$\nabla^2 T(r, z) = 0 \quad (6.2)$$

with radiative boundary conditions

$$-k \frac{\partial T(r, -h/2)}{\partial z} = \epsilon I(r) - 4\sigma' T_{ext}^3 T(r, -h/2) \quad (6.3)$$

$$-k \frac{\partial T(a, z)}{\partial r} = 4\sigma' T_{ext}^3 T(a, z) \quad (6.4)$$

$$-k \frac{\partial T(r, h/2)}{\partial z} = 4\sigma' T_{ext}^3 T(r, h/2) \quad (6.5)$$

where  $\epsilon$  is the fraction of the incident power absorbed,  $a$  is the radius of the cylindrical substrate, and  $h$  the thickness.  $k$  is the Boltzmann constant,  $\sigma'$  is the Stefan-Boltzmann constant corrected for the emissivity of the material, and the full radiative terms  $\sigma'(T^4 - T_{ext}^4)$  have been linearized around  $T_{ext}$ . For illumination with a Gaussian beam,  $I(r) = \frac{2P}{\pi\omega^2} \exp(-2\frac{r^2}{\omega^2})$  the thermal equation 6.2 and boundary conditions 6.3, 6.4, and 6.5 can be nondimensionalized by expressing the temperature in terms of a characteristic temperature  $\bar{T} = \frac{T}{T_c}$  with

$$T_c = \frac{\epsilon P}{\pi\omega k}, \quad (6.6)$$

and expressing the dimensions in terms of the beam waist,  $\bar{r} = \frac{r}{\omega}$  and  $\bar{z} = \frac{z}{\omega}$ . Hello and Vinet analyzed cylindrical substrates with these thermal conditions and showed that they lead to a temperature profile in the substrate that can be expressed as a Dini series

$$T(r, z) = T_{ext} + \sum_m \frac{\epsilon p_m a}{\kappa} e^{-\zeta_m h/2a} \frac{(\zeta_m - \tau)e^{-\zeta_m(h-z)/a} + (\zeta_m + \tau)e^{-\zeta_m z/a}}{(\zeta_m + \tau)^2 - (\zeta_m - \tau)^2 e^{-2\zeta_m h/a}} J_0\left(\zeta_m \frac{r}{a}\right) \quad (6.7)$$

with

$$\tau = 4\sigma' T_{ext}^3 a / \kappa. \quad (6.8)$$

Here  $\zeta_m$  is the  $m^{th}$  solution to

$$xJ_1(x) - \tau J_0(x) = 0 \quad (6.9)$$

and the coefficients  $p_m$  are given by

$$p_m = \frac{2\zeta_m^2}{\zeta_m^2 + \tau^2} \frac{1}{a^2 J_o(\zeta_m)^2} \int_0^a I(r) J_o\left(\zeta_m \frac{r}{a}\right) r dr. \quad (6.10)$$

The temperature profile of equation 6.7 has been used [80] to determine the thermo-elastic deformations in the substrate, which when written in dimensionless coordinates are given by

$$\bar{u}_r(r, z) = \frac{1}{\bar{r}} \int_0^{\bar{r}} \bar{T}(\bar{r}, \bar{z}) \bar{r} d\bar{r} + \frac{\omega^3}{a^2 h} \frac{\lambda + 2\mu}{2\mu(3\lambda + 2\mu)} (\bar{A}r + \bar{B}rz) \quad (6.11)$$

$$\begin{aligned} \bar{u}_z(r, z) &= \int_{-\bar{h}/2}^{\bar{z}} \bar{T}(\bar{r}, \bar{z}) d\bar{z} + \bar{\Phi}(\bar{r}) - \\ &\frac{\omega^5}{a^2 h^3} \frac{\lambda + 2\mu}{3\lambda + 2\mu} \left( \bar{A}z + \frac{1}{2} \bar{B}z^2 \right) - \frac{\lambda + 2\mu}{4\mu(3\lambda + 2\mu)} \bar{B}r^2, \end{aligned} \quad (6.12)$$

where the deformation vector is expressed in terms of a characteristic displacement,

$$\bar{u} = \frac{u}{u_c} \quad (6.13)$$

with

$$u_c = \frac{\alpha(3\lambda + 2\mu)\epsilon P}{2\pi(\lambda + \mu)k}, \quad (6.14)$$

Here  $\alpha$  is the thermal expansion coefficient, and  $\lambda$  and  $\mu$  are the first and second Lamé coefficients. They are related to the Young's modulus  $E$  and the Poisson's Ratio  $\nu$  by

$$\lambda = \frac{\nu E}{(1 + \nu)(1 - 2\nu)} \quad (6.15)$$

$$\mu = \frac{E}{2(1 + \nu)}. \quad (6.16)$$

The other terms are

$$\begin{aligned} \bar{A} &= \int_0^{a/\omega} \bar{r} d\bar{r} \int_{-\bar{h}/2}^{\bar{h}/2} \bar{T}(\bar{r}, \bar{z}) d\bar{z} \\ \bar{B} &= \int_0^{a/\omega} \bar{r} d\bar{r} \int_{-\bar{h}/2}^{\bar{h}/2} \bar{z} \bar{T}(\bar{r}, \bar{z}) d\bar{z} \end{aligned} \quad (6.17)$$

Table 6.2: Material parameters of some relevant optical materials at room temperature. All data are taken from the Electrooptics Handbook [81] except values for  $u_c$ , which are calculated from equation 6.14

Parameter	Fused Silica	Sapphire	Silicon
E: Young's Modulus [GPa]	72.6	400	165
$\nu$ : Poisson's Ratio	0.16	0.23	0.22
$\alpha$ : Thermal Expansion [ $\frac{10^{-6}}{K}$ ]	0.51	6.77	2.618
$\kappa$ : Thermal Conductivity [ $\frac{W}{mK}$ ]	1.38	46	140
$u_c$ : Characteristic Displacement [ $\frac{nm}{W}$ ]	68.2	28.8	3.63

and

$$\bar{\Phi}(\bar{r}) = \int_0^{\bar{r}} \frac{d\bar{r}'}{r'} \int_0^{\bar{r}'} \frac{\partial \bar{T}(\bar{r}'', -\bar{h}/2)}{\partial \bar{z}} r'' d\bar{r}'' + Constant \quad (6.18)$$

All free parameters in the normalized equations 6.11 and 6.12 can be combined in a single variable

$$\frac{1}{\bar{l}_{th}} = \frac{\omega}{l_{th}} \quad (6.19)$$

with  $l_{th}$  a characteristic length defined by

$$l_{th} = \frac{a}{\tau} = \frac{\kappa}{4\sigma' T_{ext}^3}. \quad (6.20)$$

$\bar{l}_{th}$  parameterizes the relative importance of radiative cooling from the heated surface versus thermal conduction into the substrate. For an ambient temperature of 300K, fused silica with thermal properties given in table 6.1 and an emissivity of 0.5 such that  $\sigma' = 0.5\sigma = 2.810^{-8} \frac{W}{m^2K^4}$ , the thermal length scale is  $l_{th} = 0.46m$ . For Silicon  $l_{th} = 46m$ . With a beam radius of  $\omega = 2cm$ , we have  $\frac{1}{\bar{l}_{th}} = 4 \times 10^{-2}$  and  $\frac{1}{\bar{l}_{th}} = 4 \times 10^{-4}$  for fused silica and silicon respectively. Thus the radiative term is small and the solutions to equations 6.11 and 6.12 with  $\frac{1}{\bar{l}_{th}} = 0$  are nearly universal curves. Figures 6.1 and 6.2 show the shape of the substrate deformation for typical optical substrates of a given geometry. With the magnitude of the deformations specified by the characteristic deformation of the material,  $u_c$  given by equation 6.14 and listed in table 6.1 for a few relevant materials.

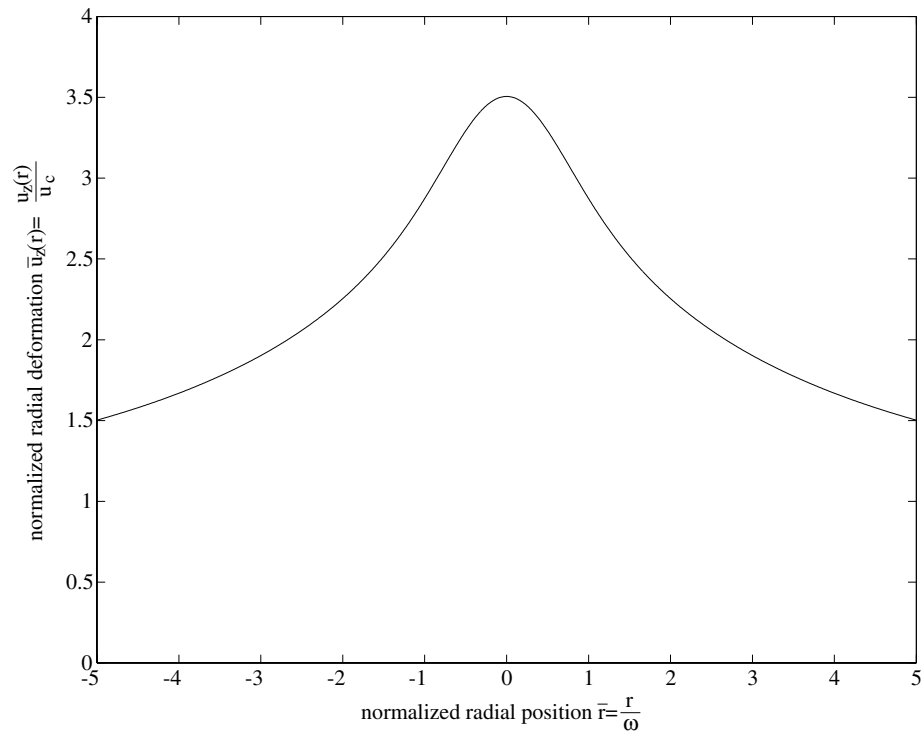


Figure 6.1: The axial surface deformation of a cylindrical substrate illuminated with a Gaussian beam. The axial deformation causes a ‘bump’ on the surface changing the radius of curvature of the optic. The magnitude of the deformation is normalized to the characteristic displacement of the substrate material given by equation 6.14. The average temperature rise of the optic produces the overall offset.

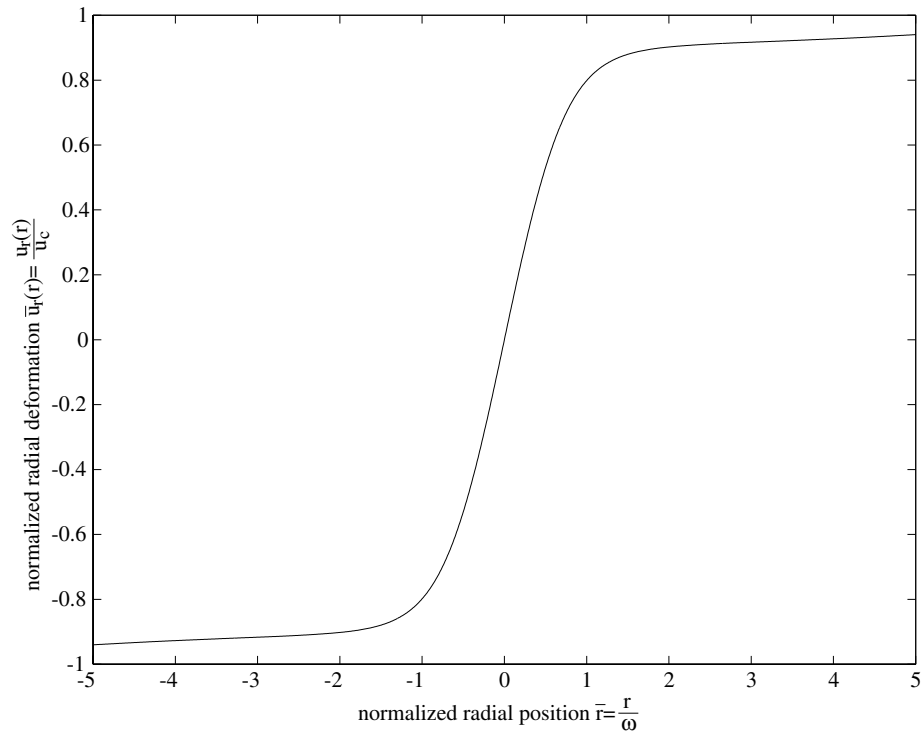


Figure 6.2: The radial surface deformation of a cylindrical substrate illuminated with a Gaussian beam. The radial deformation is only relevant when the optic is used as a grating – it causes the spacing of the grating grooves to change. The magnitude of the deformation is normalized to the characteristic displacement of the substrate material given by equation 6.14. The average temperature rise of the optic produces the overall offset.

Optical and mechanical parameters must be considered in choosing a substrate material for the optics, as must the mechanical loss of the material which governs the thermal noise produced by the optic. Fused silica has excellent optical properties and was chosen as the substrate material for LIGO based primarily on these properties and the commercial availability of large, well polished substrates. Sapphire is a material being considered for LIGO II because it has lower mechanical loss and better thermal conductivity than fused silica. The best sapphire examined to date, however, has significantly worse optical absorption than fused silica and is more difficult to obtain. A material readily available in large sizes with excellent thermal properties is elemental silicon. Silicon, however, is opaque at optical wavelengths and therefore cannot be used for transmissive optics.

## 6.2 Reflective optics

Virtually every transmissive optic in an interferometer design has a reflective counterpart which can be used to reduce thermal effects in the optics [82][83][84]. Perhaps the most obvious is curved mirrors replacing lenses. Other transmissive optics which need to be replaced by reflective optics include the beamsplitter, waveplates and possibly the spatial filter and pre-mode cleaner.

### 6.2.1 Grating beamsplitter

A diffraction grating with two real orders is functionally equivalent to a beamsplitter. For the polarization Sagnac it is necessary for the beamsplitter to separate the orthogonal polarization states of the light. Since the diffraction efficiency of a grating is generally polarization dependent, it is possible to tailor the design of the grating to make it a good polarizing beamsplitter. Large dielectric gratings with low loss capable of handling high power have been produced at Lawrence Livermore National Laboratory [85] for stretching and compressing the laser pulses of the National Ignition Facility. Thus the technology for fabricating large, high quality gratings exists.

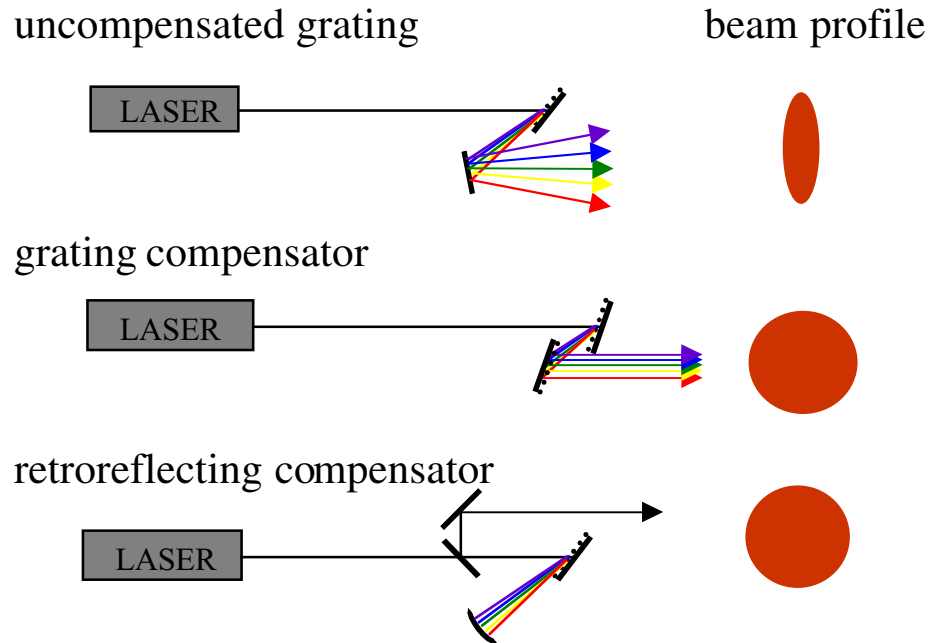


Figure 6.3: Illustration of the transfer of frequency noise of the laser to pointing noise of the diffracted beam. The top diagram shows frequency components of the light diffracted from a single grating producing a spread of the diffracted beam. The second diagram includes a second grating to compensate for the pointing noise which introduces a frequency dependent offset on the beam location. The third diagram is of a retroreflecting configuration which uses the same grating twice to compensate for the pointing noise without introducing an offset in the position of the beam. The shapes of the diffracted beams are shown on the right to illustrate the beamshaping effects of the grating and the additional compensating grating.

A few effects, however, still must be addressed with the use of a diffractive beamsplitter. The dispersion of the beamsplitter couples frequency noise of the laser to beam pointing fluctuations, the spatial profile of the diffracted beam is in general elliptical, and thermo-elastic deformation of the substrate affects the diffracted beam differently than the reflected beam in a way that has not been previously investigated.

The ellipticity of the diffracted beam can be reduced by using the grating near Littrow configuration such that  $\sin \theta_{in} \approx \sin \theta_{out}$ . This reduces the ellipticity, improving the overlap of the two interfering beams. The dispersion in the grating can be

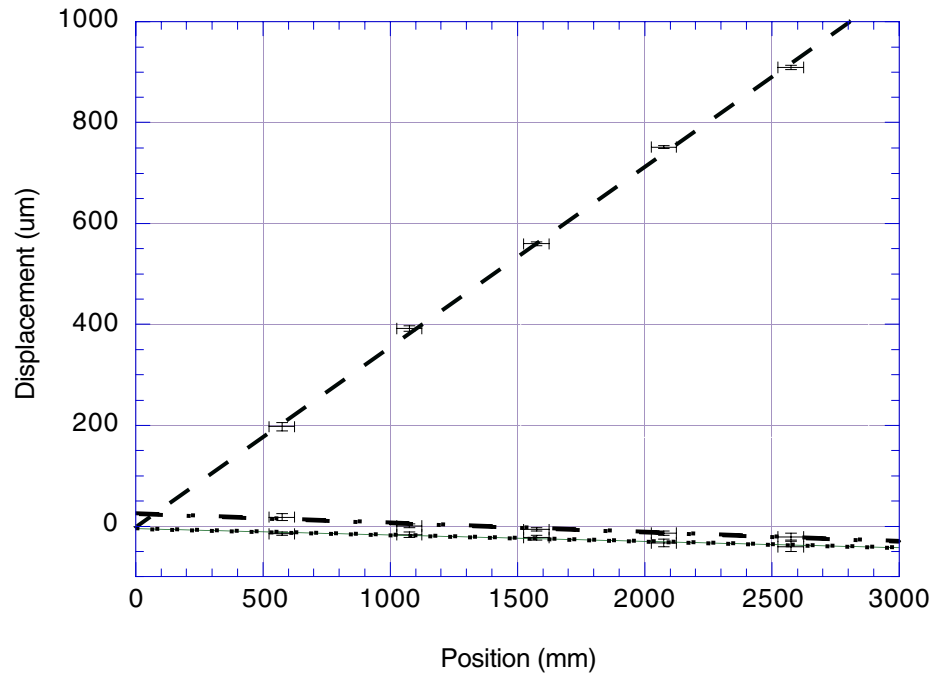


Figure 6.4: The displacement of the diffracted beam as a function of distance from the grating when the laser frequency is swept over 20 GHz. The dashed line is a fit to the data for light diffracted by a single grating, the dashed-dotted line is a fit to the data for light diffracted from a series of two gratings and the dotted line is a fit to the data for light retroreflected onto the diffraction grating.

compensated by using an additional grating or by double passing the grating to null the dispersion, as shown in figure 6.3. This technique has long been used with double passed acousto-optic modulators for frequency shifting a beam.

To demonstrate the beamsteering effect, a grating of pitch 1800 lines per millimeter was illuminated with 1064 nm light from an NPRO laser. The laser frequency was swept over 20 GHz by thermally tuning the laser crystal. The maximum displacement of the diffracted beam was measured. Figure 6.3 shows three configurations which were evaluated. Figure 6.4 shows that double passing the grating allows the dispersion to be nulled out, minimizing the coupling of laser frequency noise to beam pointing jitter.

The effects of thermo-elastic deformation of the grating have been investigated. For the reflected order, the grating acts like an ordinary mirror and the radial surface

deformation  $u_r(r, -h/2)$  can be neglected. The axial surface deformation  $u_z(r, -h/2)$  results in a phase distortion of  $\Delta\phi(r) = 2k_o u_z(r, -h/2)$  for a light beam reflected at normal incidence. More generally  $\Delta\phi(r) = C k_o u_z(r, -h/2)$  where  $C = \frac{1}{\cos\gamma_{in}} + \frac{1}{\cos\gamma_{out}}$  is a geometric factor relating the angle of the input and output reference planes to that of the grating. The phase distortion of the  $m^{\text{th}}$  diffracted order, which obeys the grating equation

$$\sin\gamma_{in} + \sin\gamma_m = \frac{m\lambda_o}{d}, \quad (6.21)$$

is influenced by the radial deformation of the substrate and the resultant changes of the local phase and period of the grating. The wavefront of the diffracted beam is perpendicular to the local k-vector of the light so that

$$\phi'(x) \equiv \frac{d\phi(x)}{dx} = k_o \tan\gamma_m, \quad (6.22)$$

With  $\gamma_m$  from equation 6.21 this becomes

$$\phi'(x) = k_o \frac{n\lambda/d - \sin\gamma_{in}}{\sqrt{1 - (n\lambda/d - \sin\gamma_{in})^2}} \quad (6.23)$$

In the near field, a distance  $z$  from the grating, the phase of the light at a point  $r_o$  on the cross section of the beam is dominated by the contributions of the illuminated grating within the first Fresnel zone. The diameter of this zone occupies a spatial extent on the grating surface of  $\Delta R \approx 2\sqrt{z\lambda}$ . If the change in radial deformation is small across this zone,  $\frac{du(r)}{dr} \ll \frac{u(r_o)}{\Delta R}$ , then the phase of the light at this point is well approximated by the phase of diffracted light from a grating with a uniform period identical to the local period at  $r_o$ , the center of the first Fresnel zone. Thus the gradient of the phase at any point in the beam's cross section converges to that given by equation 6.23 where the grating period  $d$  is replaced by the local period of the deformed grating, which can be approximated by  $d(x) \approx d_o(1 + \frac{du_x(x)}{dx}) = d_o(1 + u'_x(x))$  when the deformation is small,  $u_r(x) \ll x$ . This gives

$$\phi'_m(x) = k_o \frac{\frac{m\lambda}{d_o(1+u'_x(x))} - \sin(\theta_{in})}{\sqrt{1 - \left(\frac{m\lambda}{d_o(1+u'_x(x))} - \sin(\theta_{in})\right)^2}} \quad (6.24)$$

The *change* in the phase gradient due to a small radial deformation can be expressed as

$$\Delta\phi'_m(x) \approx -k_o \frac{m\lambda}{d_o} u'_x(x) = -mk_g u'_x(x), \quad (6.25)$$

where  $k_g = 2\pi/\Lambda$  with  $\Lambda$  the grating period. This can be integrated to recover the phase distortion due to the radial substrate deformation

$$\Delta\phi_m(x) \approx -mk_g u_x(x) \quad (6.26)$$

where the constant of integration is zero from the symmetry condition that  $u_x(0) = 0$ .

The wavefront distortion of the light in the diffracted order can be calculated by adding the phase changes due to the radial surface deformation to the phase change due to the axial surface deformation:

$$\Delta\phi_m(x) = \Delta\phi_m^z(x) + \Delta\phi_m^r(x) \quad (6.27)$$

The distortion in the reflected order and in the first diffracted order of a thermally loaded grating were calculated with this model for phase distortion and the substrate deformation shown in figures 6.1 and 6.2. In figure 6.5,  $\Delta\phi_0(x)$  and  $\Delta\phi_{-1}(x)$  are plotted relative to the phase change associated with the characteristic deformation for the substrate material,  $k_o u_c$ . The grating period used was  $d=833$  nm, the wavelength of the light was  $\lambda_{light}=1064$  nm, and the incident angle was  $\gamma_{in} = 40^\circ$ .

For an all reflective interferometer with a reflection grating as a beam splitter or a cavity input coupler the radial surface deformation of the optical substrate leads to a change in the grating profile that results in an additional phase front distortion in the diffracted light. The analysis in this section calculates the shape and magnitude of the surface deformations of a thermally loaded optical substrate. This allows the size of the deformations to be determined from only the absorbed power and the material properties of the substrate. It is clear that a material with high thermal conductivity and low thermal expansion is advantageous. Silicon is a material capable of handling

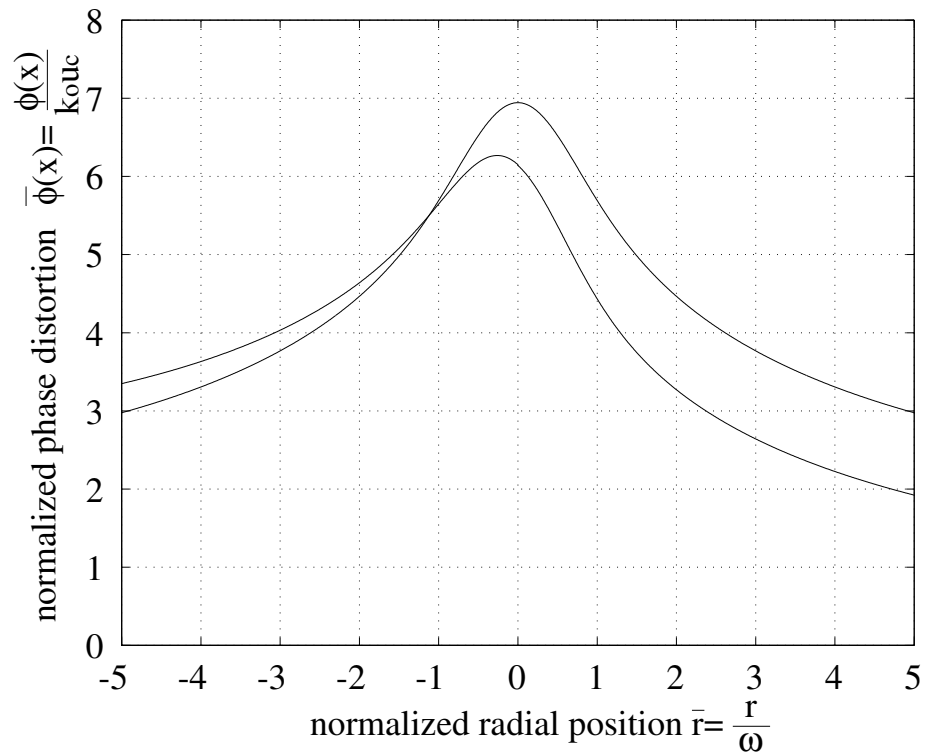


Figure 6.5: The total phase distortion of a wavefront reflected (top curve) and diffracted (bottom curve) from a thermally loaded grating. The magnitude of the distortion is normalized to  $k_0 u_c$ . For silicon optics an absorbed power of about 15 W will produce a phase distortion of  $\lambda/100$  across the beam waist for a wavelength of  $532\text{nm}$ .

more optical power than sapphire or fused silica (materials being considered for interferometric detectors with transmissive optics) that is available in large sizes and can be mechanically polished and coated to produce excellent mirrors.

### 6.2.2 Reflective waveplates

It is necessary to have a means of changing the polarization state without using transmissive waveplates to control the polarization of the beam in a reflective interferometer. Two possibilities include using the relative phase shift introduced between the s and p polarization of a beam reflecting off a mirror at non-normal incidence, and using a periscope to rotate the spatial profile of the beam, and hence its polarization.

A reflective dielectric mirror can be engineered to produce a  $180^\circ$  phase shift between the s and p-polarization components of the beam, so that it acts like a reflective half-wave plate. For a half-wave plate to rotate linear polarization by  $90^\circ$  there must be equal polarization components of the light along the fast and slow axis of the waveplate. For the reflective waveplate this means equal components of s and p-polarized light. In the polarization Sagnac interferometer, however, the polarization of the circulating light is set by the beamsplitter. For a beam path that stays in the horizontal plane the polarization in the interferometer is entirely s or p-polarization depending on the position in the loop relative to the waveplate. Thus it is necessary to reflect the light out of the horizontal plane so that the s and p-polarization directions for the reflective waveplate can be redefined such that there is equal power in each polarization component.

Both the polarization rotating periscope and the dielectric reflecting waveplate require the beam to travel out of the horizontal plane at some point. A vertical component to the beam direction requires increased stability of the mirrors in the vertical direction. Although it would be technically difficult to increase the vertical isolation of the suspension system, it is possible to place these elements near the symmetry point of the interferometer loop where displacement noise is common mode and the isolation requirements are weak.

### 6.2.3 Spatial filter

For high fringe contrast it is useful to select the spatial mode of the input and output beams of the interferometer with a spatial filter. The spatial filter can take many forms including a cavity, a pinhole or a single mode fiber. These devices, however, have their own power handling limitations. Cavities are subject to the same thermal distortions of the interferometer core optics, The strongly focused beam at a pinhole can damage the membrane containing the pinhole and single mode fibers are damaged by high intensity fields in their core.

A cavity can be used as a spatial filter, either as a linear Fabry-Perot cavity or a ring cavity. A ring cavity with transmissive input and output coupling mirrors is used in LIGO I and is proposed for LIGO II as a spatial filter at the input. This ring cavity could be made to handle much higher power using diffractive optics as the input and output couplers.

We have demonstrated a ring cavity with a weak grating acting as the input and output coupler. The cavity is shown in figure 6.6. By using a weak grating as the input coupler the coupling can be made small and the losses associated with the grating, which are a fraction of the diffraction efficiency, can also be made quite small. A flat polarization selective grating,  $\eta_s = 0.95$  for s-polarization and  $\eta_p = 0.02$  for p-polarization, was used as one mirror in a three mirror ring cavity. The grating was illuminated with p-polarization and the other two mirrors were arranged to circulate the diffracted light inside of the ring cavity. The circulating light diffracted from the grating was taken as the output beam. While this configuration allows the diffraction losses to be small, the ellipticity of the circulating beam produced by the input grating requires either aspheric optics for compensation, or the gratings to be used near Littrow configuration where the ellipticity is smallest. We observed a finesse of approximately 100 in this cavity limited by the level of output coupling from the diffraction grating. A similar ring cavity with two gratings as the input and output couplers could be used as the pre-mode cleaner and spatial filter for the input and output beams of an all-reflective interferometer.

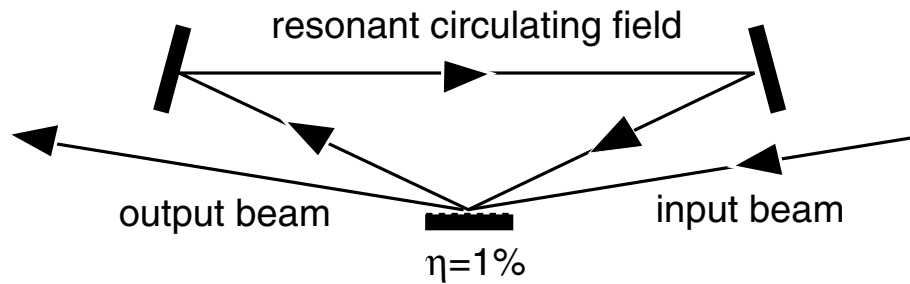


Figure 6.6: A resonant cavity with a grating as an input coupler. The light couples in and out of the cavity by diffracting from the weak grating. Since the grating efficiency is small, the associated losses, which are a fraction of the efficiency, are also small, allowing the cavity to have high finesse.

### 6.3 The polarization Sagnac with reflective optics

Figure 6.3 shows a schematic of the 10 m all-reflective Sagnac interferometer with suspended silicon optics. Although this interferometer operates with a circulating power well below that which would limit the sensitivity of an interferometer with transmissive optics, implementing all-reflective optics was important to gain experience with practical issues that are associated with their use. The suspension of the optics, which had no active control, was meant to demonstrate the robustness of the interferometer to mirror motion and the reduced control requirements of the Sagnac interferometer. Above all, this interferometer was a first step in bringing the elements of an advanced interferometer together into a working instrument.

#### 6.3.1 The suspension system

The suspension system of the interferometer is meant to keep the control of the instrument as simple as possible, allowing for large amplitude motion of the optics in the beam direction and relatively small motion of the optics in the other degrees of freedom.

The beamsplitter, the steering and focusing mirrors, and the polarization rotating periscope were all mounted on a single aluminum breadboard which was suspended upside down by 4 steel wires from a unistrut frame in the end chamber of the vacuum

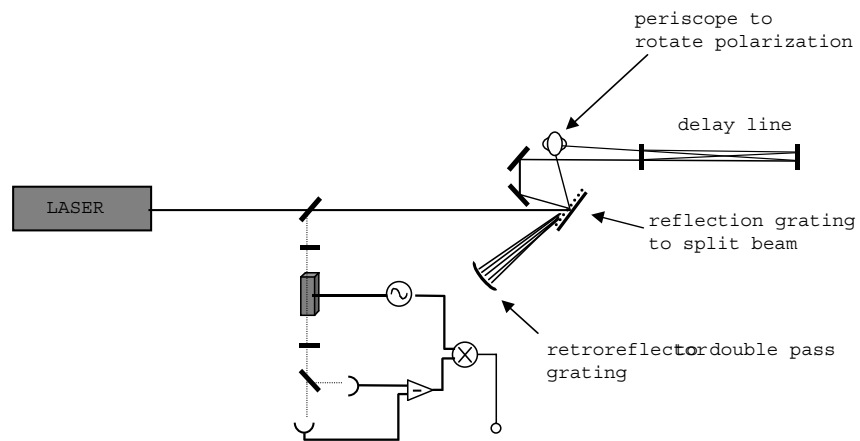


Figure 6.7: The 10 m Sagnac. The delay line mirror spacing is 9.41 m and there are 37 round trips making the peak response at 217 kHz. A periscope rotates the polarization of the beams in the interferometer by  $90^\circ$ . A reflective grating beamsplitter is double passed to eliminate its dispersion.

system at the LIGO Engineering Test Facility (ETF) located at Stanford. The suspension of this breadboard had a quality factor of  $Q \approx 10^4$ . Although the ringdown time for its 1 Hz pendulum motion is several hours, motion of the breadboard was not problematic as it has a mass of 40 kg and so was not easily excited when carefully touching the adjustment screw on the optics during alignment.

The delay line mirrors were each suspended by a 5-wire suspension which was intended to constrain the motion of the optics in all degrees of freedom other than the beam direction. In reality the twisting mode of the suspension which corresponds to the pitch of the mirror had a resonant frequency of 1.1 Hz – nearly degenerate with the 1 Hz resonant frequency of the longitudinal pendulum mode. All other degrees of freedom of the suspension had resonant frequencies above 10 Hz and so were relatively stiff compared to the longitudinal degree of freedom. One mirror was suspended from the unistrut cage in the end chamber of the vacuum system, while the other was suspended from a small unistrut cage located 9.41 m away in a tube positioned to connect the two end chambers of the vacuum system. During these experiments the tube was disconnected from the second end chamber and capped so that the two chambers could be used independently.

The delay line mirrors are 1 inch thick, 6 inch diameter silicon substrates with a mass of 1.1 Kg. They sat in a 200 g aluminum cradle that attached to the suspension wires. The wires were hung from two degrees-of-freedom tilt stages, one of which was mounted to the unistrut frame at the end of the vacuum tube, the other onto a linear translation stage with 4 inches of travel to allow the length of the delay line to be adjusted. This translation stage was attached to the unistrut frame in the end chamber of the vacuum system. The pitch and yaw of the mirrors were adjusted by manipulating the tilt stage from which they were hung, much like a marionette puppet is controlled. Eddy current damping of the suspensions were mounted to the unistrut frame 8" apart, with their poles on either side of the ends of the aluminum cradle so that the magnetic flux from each magnet passed through an end of the cradle. Motion of the ends of the cradle, which is primarily due to the twisting of the suspension, caused eddy currents to be created in the aluminum as it moved perpendicular to the magnetic flux. These eddy currents were dissipated by the electrical resistance of the



Figure 6.8: The delay line suspension system located within the Engineering test Facility 10 m vacuum system end tank

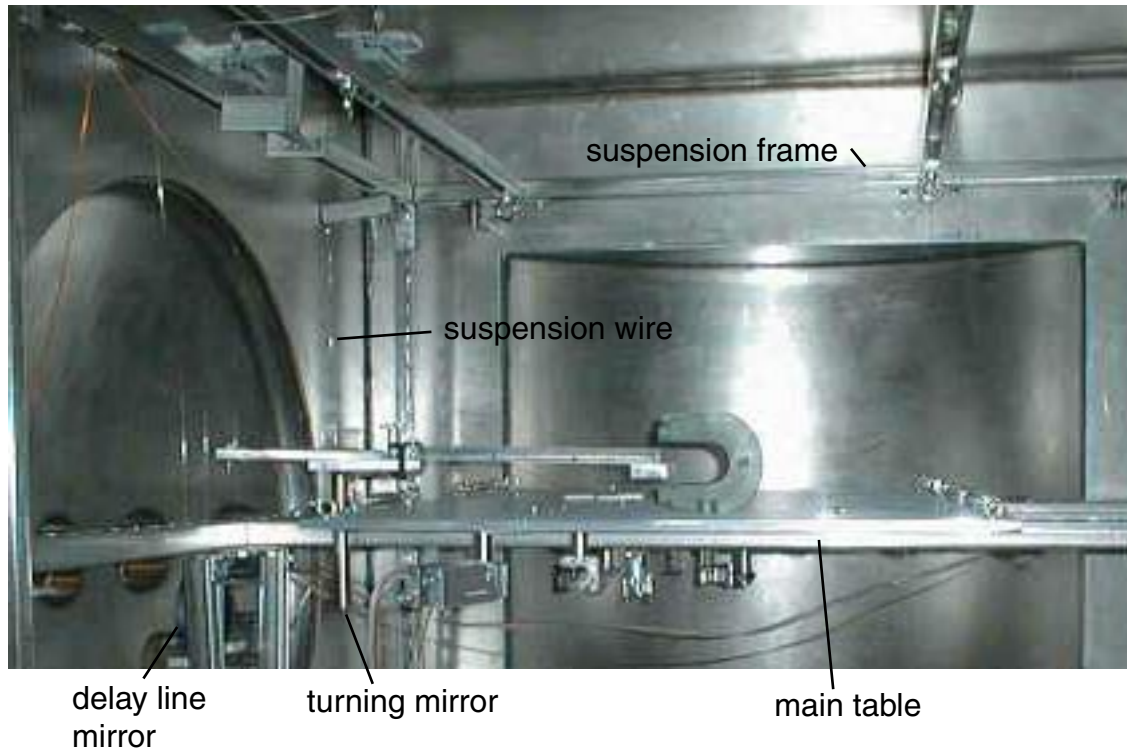


Figure 6.9: An overview of the suspension system. The beamsplitter and most of the turning mirrors are mounted directly to the main table which hangs from the suspension frame. The delay line mirrors and a single turning mirror are mounted on similar independent suspensions.

aluminum, thereby damping the motion of the cradle. With the dampers in place the ringdown time for the cradle was about 10 seconds.

The turning mirror, which reflects light into and out of the delay line, was suspended in a manner almost identical to that of the delay line mirrors. The motion of the cradle was also passively damped with eddy current damping. To preferentially damp out the twisting motion of this mirror, a long (24") fin was attached to the mirror mount which had an aluminum block mounted to the end. A large horseshoe magnet was placed on top of the 40 kg breadboard with its poles on either side of the aluminum block. This damped the motion of the turning mirror with respect to the relatively stable breadboard. The long fin acts like a lever allowing the damping to have a stronger effect on the twisting motion of the turning mirror.

Three of the suspensions were hung from a 6'x6'x6' unistrut frame that was initially shimmed into the vacuum chamber at four points along each of the side faces of the cube it defined. When the vacuum system was pumped down the frame was compressed causing enough differential motion of the suspension points for the interferometer to become misaligned to the point where the light would not return to the beamsplitter. After removing the shims so that the frame was only in contact with the vacuum chamber floor all noticeable drift of the optics was eliminated. The fourth suspension was hung from a frame at the end of a vacuum tube that protruded from the end tank. As the vacuum system was pumped down the bellows connecting sections of the tube to the end chamber compressed slightly, despite being reinforced by threaded rods, causing the length of the delay line to shorten and the reentrant condition of the beam to change. This was accommodated by an actuator on the translation stage from which one delay line mirror was hung. This allowed correction for the drift of the mirror after system was in vacuum.

### 6.3.2 The reflective optics

Reflective silicon optics were used in place of transmissive optics. Two issues with the polarization rotating periscope were challenging; the beam profiles of the two interfering beams are rotated  $90^\circ$  with respect to each other requiring a high degree of radial symmetry of the beams, which we did not have, and the rotation makes the alignment of the interferometer less intuitive.

Two curved mirrors before and after the delay line shape the beam to the profile that was optimized for the particular delay line geometry. None of these mirrors were used exactly at normal incidence since the beam travels in a ring and does not close on itself. The worst involved was a mirror at an incident angle of  $20^\circ$  due to the constraints of the breadboard in arranging the optical path. This rather large incident angle for a curved mirror introduced astigmatism in the beam, creating an elliptical beam profile. The beam in one direction was given this astigmatism before being rotated by the periscope, while the other encountered the periscope before reaching this mirror. The result is that the beams exiting the interferometer had a slightly

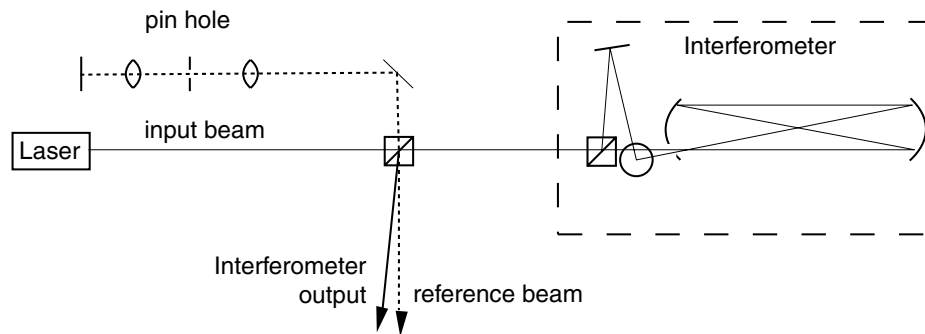


Figure 6.10: The reference beam for interferometer alignment is generated by retroreflecting the light picked off from the input beam. The beam is passed through a  $10\mu\text{m}$  pinhole before and after a retroreflecting mirror to ensure the beam returning to the beamsplitter is colinear with the beam picked off from the input beam. The position of the retroreflecting mirror is chosen to be at the focus of a lens so that the returning beams curvature matches that of the incoming beam. The reference beam has the desired curvature and orientation of the aligned interferometer output.

elliptical profile which were oriented at  $90^\circ$  with respect to each other. This limited the fringe contrast but still allowed the interferometer to function as designed.

The second difficulty in using the periscope for polarization rotation was acquiring overlap of the two output beams. Typically when aligning a Sagnac or other two-beam interferometer, a steering mirror can be tilted around one axis until the output beams coincide along that direction, then along the other axis until they coincide along that direction. By iterating this procedure for a pair of mirrors the output beams are made colinear. With the periscope, however, adjusting the tilt of a mirror caused the output beams to move orthogonally to each other. This greatly increases the parameter space over which one can search to look for good alignment. To deal with this a reference beam, shown in figure 6.10, not affected by the alignment of the steering mirror, was created for alignment.

The challenges introduced by using the periscope can be dealt with by taking care to preserve the radial symmetry of the beam profile and by developing practical techniques such as that used for alignment that aren't typically necessary for working with interferometers without such devices. Despite these challenges, the all-reflective delay-line polarization Sagnac interferometer was aligned by the author working alone.

### 6.3.3 Scattered light in the interferometer

The sensitivity of the interferometer was shot noise limited above 20 kHz with 300 mW of input laser power. Below 20 kHz the noise floor was set by mirror displacement noise coupling through scattered light. The noise from scattered light is due to both laser frequency noise and to mirror displacement noise caused by the motion of the fringe pattern of the Michelson ‘ghost’ interferometer formed between the local oscillator and the scattered light that finds its way to the detector. Two likely ways that light can reach the photodetector through an unintended path are through poor reimaging and through scattering. If the beam, returning to the entrance hole of the delay line after  $N$  round trips, is not reimaged precisely on the aperture the edge of the beam does not exit the delay line, but travels an additional  $m \times N$  round trips, where  $m$  is an integer, in the delay line before exiting through the entrance hole. Additionally light can scatter from one reflection spot into the beam of a neighboring reflection spot thereby acquiring or eliminating an additional path length of  $4m\Delta L$  where  $\Delta L$  is the separation of the delay line mirrors.

Using the laser frequency sweep described in section 4.2.3 the noise from scattered light was shifted to higher frequencies and the noise introduced by stray light with different excess path lengths was separated. We used a 15 V square waveform with a 10 second period to drive the thermal control of the Nd:YAG NPRO. The thermal response of the laser crystal cut off at about 1 Hz, so this produced an approximately triangular sweep of the crystal temperature that, through the temperature dependence of the index of refraction of the crystal, led to a laser frequency sweep of 2.17 GHz/s. Most of the scattered light noise is shifted by integer multiples of 5.05 kHz. Figure 6.11 shows the noise from scattered light shifted to several different frequencies corresponding to scattered light delays that are multiples of 37 round trips between the delay line mirrors, or one complete reimaging of the beam. Scattered light noise was also observed shifted to half of these frequencies, suggesting that another stray path is also taken by the the scattered light.

Figure 6.12 shows that at frequencies below 5 kHz, the frequency between the local oscillator and the scattered light with  $m = N/2$ , is reduced to the shot noise limit.

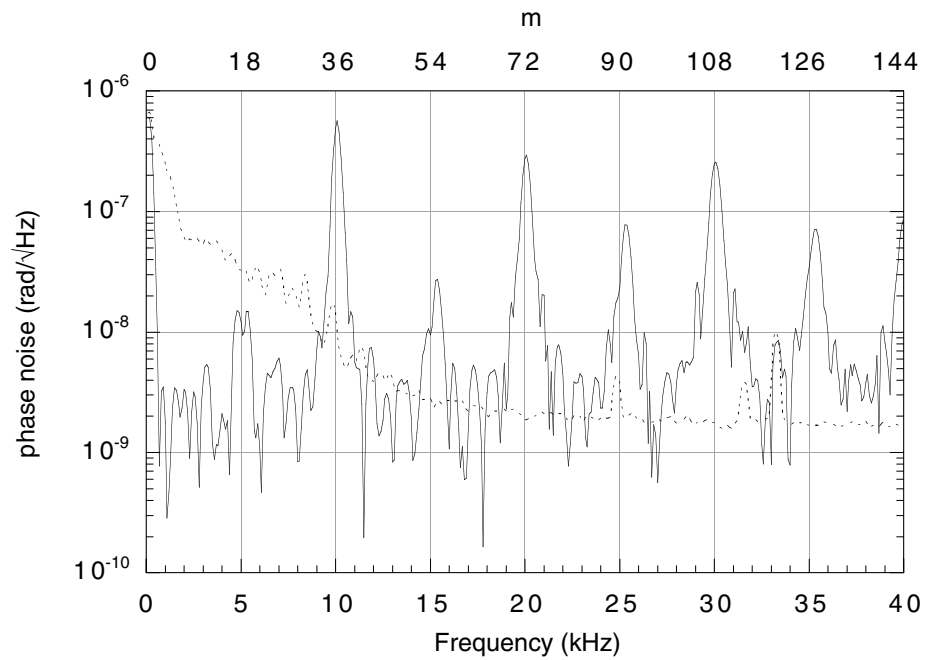


Figure 6.11: the noise spectrum from 0 to 40 kHz without the laser frequency sweep (dotted line) and with the laser frequency sweep (solid line). The noise from scattered light is shifted by a frequency which is proportional to the total excess path the light takes. The top axis of the graph is scaled to represent  $m$ , the excess number of round trips in the delay line for noise shifted by the stray light to that frequency.

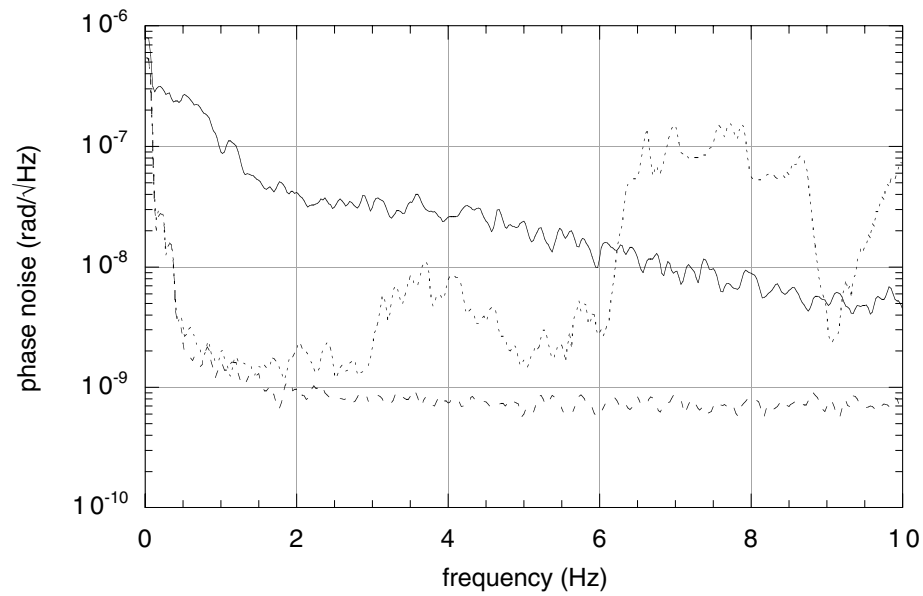


Figure 6.12: The low frequency noise floor of the polarization Sagnac interferometer. The equivalent phase noise for the photodetector dark current (dashed curve), the phase noise without the laser frequency sweep (solid curve) and the phase noise with the laser frequency sweep (dotted curve) are shown. Without the laser frequency sweep the noise floor is set by the scattered light. With the frequency sweep the noise floor is set by shot noise from about 500 Hz to 3 kHz and by electronic noise below 500 Hz.

## 6.4 Summary

Thermal distortions in the optics will limit the circulating power in advanced interferometric detectors. Power absorbed at the surface and in the bulk of transmissive optics create thermo-elastic deformations in the substrate and also create a thermal lens that distorts the transmitted wavefront. Operating the interferometer with all-reflective optics greatly increases the power handling capability of the interferometer and opens up the choice of optical substrates to include materials that don't have good optical properties in transmission. Silicon is one such material that is available in the large sizes necessary for delay line mirrors and can be commercially polished and coated. The thermal conductivity of silicon is sufficient that an all-reflective interferometer with silicon optics can handle several megawatts of power. Reflective gratings can act as beamsplitters, provided steps are taken to compensate the dispersion and beamshaping effects of the grating on the diffracted beam.

A 10 m all-reflective interferometer with suspended silicon optics was operated with shot-noise-limited sensitivity down to 500 Hz. A reflection grating was used as the polarizing beamsplitter with the diffracted beam being reimaged onto the grating to null the dispersion and eliminate the beam shaping effect of the grating. 6 inch diameter silicon optics were used for the delay line mirrors; they were polished to  $\lambda/20$ , and coated for a reflectivity of  $R = 0.99999$ . The mirrors were purchased from General Optics at a cost that was only 10% greater than for comparable fused silica mirrors. Although the alignment of the optics was not automated or actively monitored, the author was able to align the interferometer in the course of a day working alone. The position of the mirrors was not controlled, and the rms displacement noise for the delay-line mirrors was 50 microns. Despite this the measured sensitivity was shot noise limited at frequencies as low as 500 Hz for 300 mW of input power with the laser frequency sweep to reduce the low frequency effects of scattered light noise. This demonstrates the robustness of the Sagnac interferometer and the excellent sensitivity that the polarization scheme allows.

# Chapter 7

## Conclusion

The purpose of the work described in this thesis is to investigate the Sagnac interferometer for an advanced LIGO detector. Unlike first generation interferometric gravitational wave detectors, which were limited by available laser power, advanced detectors will be limited by thermal loading of the optics. The design parameters for an interferometer for thermally loaded operation are significantly different. The interferometer must operate robustly with high power illumination, making the use of transmissive optics and resonant cavities unfavorable. The Sagnac interferometer promises more robust operation than the Michelson interferometer; the work presented in this thesis helps to realize that promise for an advanced LIGO interferometer.

### 7.1 Summary of this work

I have developed and demonstrated a polarization Sagnac interferometer that uses all-reflective optics and delay-lines in the arms to set the interferometer response in the 10 Hz - 1000 Hz signal band to optimize sensitivity. The relative phase of the interfering beams is very stable, since the beams travel a common path allowing excellent sensitivity in noisy environments with little control of the interferometer degrees of freedom; for the 10 m interferometer with suspended optics, the root-mean-square relative motion of the uncontrolled mirrors was over 50 microns, but

the interferometer still achieved a shot noise limited phase sensitivity of  $\Delta\widetilde{\phi}(\omega) = 10^{-9} \text{radHz}^{-1/2}$  above 500 Hz.

There are three key components of the interferometer design. The first is a polarization scheme that allows the dark fringe of interference to be detected on the reciprocal port of the beamsplitter where the fringe contrast is unaffected by imperfections of the beamsplitter. This scheme allows the splitting ratio of the beamsplitter to be set by adjusting the polarization of the input beam so that the counterpropagating beams have equal power. It also allows a grating beamsplitter to be used in an all-reflective configuration and allows a spatial filter to simultaneously filter the input and output beams to remove any light that couples out of the intended spatial mode in the interferometer.

The second key component to the polarization Sagnac interferometer design is the signal readout scheme. The polarization state of the output is separated to produce orthogonally polarized signal and local oscillator beams. This is important because it maintains the common-path of the interfering beams – both signal beams *and* the local oscillator. Additionally it allows the heterodyne sidebands of the local oscillator to be generated by a phase modulator at the output of the interferometer where the modulator crystal is not subject to high power. With balanced detection this signal readout scheme has little sensitivity to amplitude or frequency noise of the laser.

The final key to the interferometer design is the laser frequency-sweep to reduce the in-band noise from scattered light. Scattered light from the delay lines that reach the photodetector add phase noise to the signal. This noise coupling has been the key reason that delay-lines have been avoided in first generation gravitational wave detectors. A large-amplitude, low-frequency sweep of the laser frequency results in a frequency difference between the local oscillator and the scattered light that shifts the phase noise from the scattered light out of the measurement band. The advantage of this method to suppress scattered light noise is that it is technically very easy to generate – the temperature of the laser head is slowly adjusted to tune the laser frequency.

The fundamental differences between a common-path interferometer and a resonant configuration are highlighted by the alignment and control tolerances calculated

in chapter 5. The key differences are that the delay line Sagnac requires much more laser power than the recycled Fabry-Perot Michelson, but is much less sensitive to the absolute position of the mirrors. In a few years the available laser power will likely exceed the power handling capability of the recycled Fabry-Perot Michelson interferometer, eroding the advantages of the resonant configurations.

In the delay line polarization Sagnac interferometer, all-reflective optics can be used. By eliminating transmissive optics, thermal lensing and thermo-elastic deformation caused by power absorbed in the bulk of the substrate are eliminated. Additionally, materials such as silicon that are not optically transparent but have excellent thermal and mechanical properties can be used. Thermal distortions in reflective silicon optics are approximately ten times smaller than in fused silica. In an all-reflective interferometer with silicon optics several megawatts of power can circulate in the interferometer before thermal distortions limit the interferometer sensitivity.

## 7.2 Future work

Although several challenges to using the Sagnac interferometer for gravitational wave detection have been addressed, more research is necessary to better characterize and understand this configuration.

The amount of scattered light trapped in LIGO-scale delay lines with high quality mirrors needs to be experimentally investigated. The amount of scattered light trapped in the delay lines with mirrors kept clean in vacuum and beam tube baffles to reduce the scatter from the tube walls will likely be less than that found here. The amount of scattered light sets the requirement on laser frequency and will influence the laser design.

High power lasers are needed at green wavelengths or shorter. Therefore the development of high power solid-state lasers such as Yb:YAG must continue and progress must be made on efficient second (or higher) harmonic conversion with high average power.

High finesse all-reflective mode cleaners must be developed. The demonstration of a low efficiency grating to couple into a resonant cavity provides a starting point for

this work. Custom gratings with low diffraction efficiency and correspondingly low losses in a ring cavity should provide performance comparable to traditional mode-cleaners with a much high power handling capability.

Two difficulties created by the need for high laser power are the difficulty in generating the intense fields, and the challenge of dumping the beam which is reflected from the interferometer back towards the laser. The polarization Sagnac reflects all of the carrier light back towards the laser, and therefore could become one of the mirrors forming the laser cavity. The active Sagnac interferometer would take advantage of the higher circulating internal cavity field. Further because the gain medium would be inside of the cavity it would not be necessary to lock the cavity, as the laser frequency would passively track the cavity. The output coupling of this laser would be due to the gravitational-wave-induced phase difference in the arms causing light to leave through the polarizing beamsplitter.

Additionally advanced techniques not discussed in this dissertation such as the use of cryogenic optics, squeezed light, and detection with quantum non-demolition could eventually be considered. My research suggests that the challenges to using the Sagnac interferometer in an advanced gravitational wave detector are tractable and if met would allow a much simpler, more robust system than resonant Fabry-Perot Michelson interferometer configurations.

...

# Appendix A

## Other methods to reduce scattered light noise

All methods to reduce the effects of scattered light involve dithering the frequency of the laser. The technique described in section 4.2.3 uses a very slow, but large tuning range frequency sweep. Two other techniques involve much faster, but smaller-amplitude frequency modulation.

The first alternative method involves phase modulating the input light at a frequency that is high compared to the measurement band of the interferometer [67]. The time difference between the main beam and the stray light causes the modulation to produce a time varying phase between the stray light and the main beam. The modulation depth can be chosen so that the phase averages to zero in the measurement time. In this case the noise spectrum from the stray light is shifted by the modulation frequency. This technique, however, only eliminates the noise from stray light with delays that are odd multiples of a single value; it cannot suppress noise from many paths the stray light can take between the delay line mirrors.

Another alternative method to reduce the effects of scattered light uses low coherence light to reduce the contrast of the interference of beams with a finite path-length-difference. This has been implemented [68][86] by increasing the linewidth of a narrow band source with Gaussian, or pseudo-random noise in the past. We have

investigated this method using a low coherence source illumination. Amplified spontaneous emission (ASE) from a pumped Nd:Glass fiber illuminated a 2 m, 75 bounce delay-line polarization Sagnac interferometer. Figure A shows the effect the low coherence illumination on the delay line spot pattern. Figure A shows the scattered light limited noise floor for the interferometer with laser illumination and the low coherence ASE illumination.

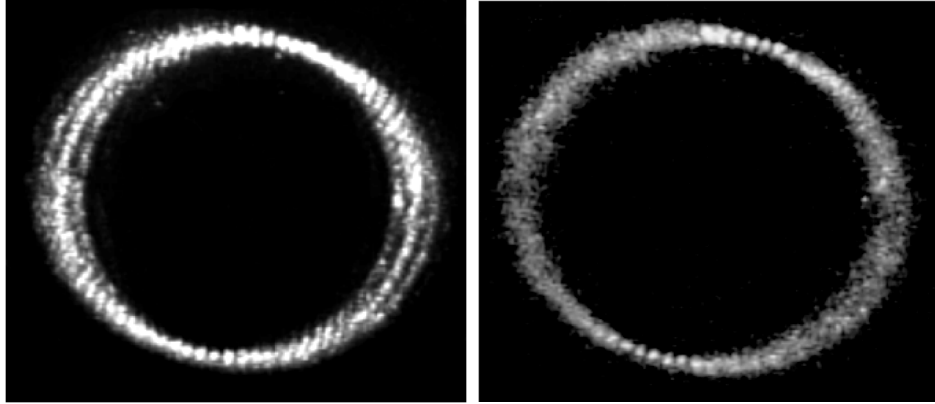


Figure A.1: The spot pattern in a delay line with (a) coherent illumination and (b) incoherent illumination. The interference effects where the beams overlap are not present with the incoherent illumination

Following the analysis of Armstrong [74], consider a light source with a spectral linewidth of  $\delta$ . If the reference phase of the light undergoes a random walk the probability that it will have changed by  $\Delta\phi$  in a time  $\tau$  is

$$P_\tau(\Delta\phi) = \frac{1}{\sqrt{2\pi\delta\tau}} e^{-\frac{\Delta\phi^2}{2\delta\tau}}. \tag{A.1}$$

At the dark port of the Sagnac interferometer the two main beams interfere with a local oscillator and any scattered light which reaches the detector

$$\vec{E}_{dp} = \vec{E}_1 - \vec{E}_2 + \vec{E}_{LO} + \vec{E}_{sc} \tag{A.2}$$

so that in the absence of a gravitational wave signal, with

$$\vec{E}_1 - \vec{E}_2 \rightarrow 0, \tag{A.3}$$

the intensity envelope at the detector is

$$\langle I_{\text{det}}(t) \rangle = \left| \vec{E}_{LO}(t) + \vec{E}_{sc}(t) \right|^2 = \langle I_{LO}(t) \rangle + \langle 2E_{LO}(t) E_{sc}(t) \cos(\Delta\phi_\tau) \rangle + \langle I_{sc}(t) \rangle \quad (\text{A.4})$$

which when transformed to the frequency domain using

$$\langle I_{\text{det}}(\omega) \rangle = \frac{1}{2\pi} \int_{-\infty}^{\infty} \langle I_{\text{det}}(t) \rangle e^{i\omega t} dt \quad (\text{A.5})$$

gives

$$\langle I_{\text{det}}(\omega) \rangle = (I_{LO} + I_{sc}) \delta(\omega) + 2E_{LO}(\omega_0) E_{sc}(\omega - \omega_0) \int_{-\infty}^{\infty} \cos(\Delta\phi_\tau) dt. \quad (\text{A.6})$$

Replacing the integral over all time with a probability integral over all possible outcomes gives

$$\langle I_{\text{det}}(\omega) \rangle = (I_{LO} + I_{sc}) \delta(\omega) + 2E_{LO}(\omega_0) E_{sc}(\omega - \omega_0) \int_{-\infty}^{\infty} P_\tau(\Delta\phi) \cos(\Delta\phi_\tau) d\Delta\phi \quad (\text{A.7})$$

which evaluates to

$$\langle I_{\text{det}}(\omega) \rangle = (I_{LO} + I_{sc}) \delta(\omega) + 2E_{LO}(\omega_0) E_{sc}(\omega - \omega_0) e^{-\delta\tau/2}. \quad (\text{A.8})$$

Thus the intensity of the interference between the scattered light and the local oscillator is decreased by a factor of  $e^{-\delta\tau/2}$  for light with a finite linewidth.

The relative fluctuations of the output intensity of a 2 beam interferometer has been calculated by Armstrong [74] to be

$$\rho = \frac{1}{2} \frac{1 + e^{-4\delta\tau} - 2e^{-2\delta\tau}}{1 + e^{-\delta\tau} + e^{-2\delta\tau}} \quad (\text{A.9})$$

where the total time difference between the two beams is  $2\tau$ . The power spectrum of

intensity fluctuations is

$$S_i(f) = \frac{4e^{-2\delta\tau}}{\delta} \left( \frac{2\pi f/\delta \sin(4\pi f\tau)}{1 + (2\pi f/\delta)^2} - \frac{\sin(4\pi f\tau)}{2\pi f/\delta} \right) \quad (\text{A.10})$$

found from

$$S_i(f) = 4 \int_0^{\infty} R_i(T) \cos(2\pi fT) dT \quad (\text{A.11})$$

where

$$R_i(T) = \langle i(t+T) i(t) \rangle = \lim_{x \rightarrow \infty} \frac{1}{x} \int_0^x i(t+T) i(t) dt \quad (\text{A.12})$$

so the intensity noise is

$$\tilde{I}(\omega) = 2 \sqrt{P_1 P_2 \frac{4e^{-2\delta\tau}}{\delta} \left( \frac{\omega/\delta \sin(2\omega\tau)}{1 + (\omega/\delta)^2} - \frac{\sin(2\omega\tau)}{\omega/\delta} \right)} \quad (\text{A.13})$$

For  $\omega \ll \delta$

$$\lim_{\delta\tau \ll 1} \tilde{I}(\omega) = 2 \sqrt{\frac{2}{3} P_1 P_2 \delta \tau^{3/2}} \quad (\text{A.14})$$

and

$$\lim_{\delta\tau \gg 1} \tilde{I}(\omega) = 2 \sqrt{2 P_1 P_2 \delta^{-1/2}}. \quad (\text{A.15})$$

For the intensity noise to be below the shot noise on the detector as given by equation 2.23

$$\delta < \sqrt{\frac{3 P_{BS} \hbar \omega_0}{4 P_1 P_2 \tau^3}} \quad \text{if } \delta\tau \ll 1 \quad (\text{A.16})$$

and

$$\delta > \frac{4 P_1 P_2}{P_{BS} \hbar \omega_0} \quad \text{if } \delta\tau \gg 1 \quad (\text{A.17})$$

where  $P_{bs}$  is the power on the beamsplitter, which is not necessarily related to the two beams interfering at the photodetector, for instance when  $P_1$  is due to scattered light,  $P_2$  is a local oscillator but the bulk of the power on the beamsplitter  $P_{bs}$  is from two beams which interfere destructively at the detector.

To keep the intensity noise due to scattered light below the shot noise level it is necessary to use a source with a broad enough linewidth so that the scattered light

essentially adds up incoherently with the local oscillator on the detector

$$\delta > \frac{4P_1P_2}{P_{BS}\hbar\omega_0} \tag{A.18}$$

however the source linewidth must not be so broad that intensity noise is generated between the two destructively interfering beams of the Sagnac

$$\delta < \sqrt{\frac{3P_{BS}\hbar\omega_0}{4P_1P_2\tau^3}} \tag{A.19}$$

where  $\tau$  represents half of the transit time difference between the beams, one half of the optical period for the polarization Sagnac. Defining the source coherence as  $L_c = \frac{c}{\delta}$  then

$$L_{int} < L_c < L_{sc} \tag{A.20}$$

where the effective interferometer asymmetry length is

$$\Delta L_{int} = c\sqrt{\frac{4P_1P_2\tau^3}{3P_{BS}\hbar\omega_0}} = 3 \times 10^{-7}m \tag{A.21}$$

and the effective scattered light asymmetry length is

$$\Delta L_{sc} = c\frac{P_{BS}\hbar\omega_0}{4P_1P_2} > 6 \times 10^{-8}m$$

for  $P_1 = P_2 = 1W$  for  $P_1 = 1W$  and  $P_2 = 10^{-6}W$ ,  $\Delta L = 6cm$ . Thus the optimal coherence length is near 10 microns, corresponding to

$$\delta = 3kHz.$$

...

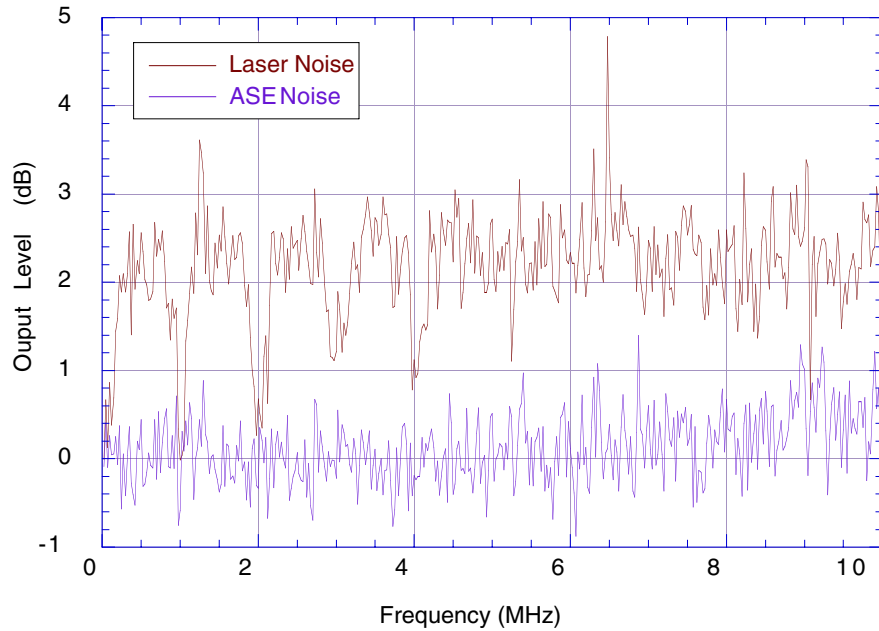


Figure A.2: Scattered light noise with laser illumination and with low coherence ASE illumination. A thin wire was placed in front of one delay line mirror to introduce scatter that couples seismic noise and laser frequency noise to the output signal. The top curve (solid trace) shows the noise level from 0 to 10 MHz when a highly coherence Nd:YAG laser illuminates the interferometer. The noise level is measured relative to the noise level with low-coherence ASE illumination (dashed trace). The noise from scattered light has a frequency dependence because of the relative delay of the scattered light compared to the main beam. The coupling of scattered light noise to the output is nulled at frequencies corresponding to the relative delay of the scattered light. With low coherence illumination the output noise level is comparable to the noise level with highly coherent illumination at the null frequencies indicating that the scattered light noise has been suppressed below the electronic noise floor of the measurement.

# Bibliography

- [1] Bernard F. Schutz, *A first course in general relativity* Cambridge University Press, 1985
- [2] C.W. Misner, K.S. Thorne, and J.A. Wheeler *Gravitation*, W.H. Freeman & Co., San Francisco (1970)
- [3] A. Einstein *Preuss. Akad. Wiss. Berlin*, Sitzungsberichte der physikalisch-mathematischen Klasse 668 (1916)
- [4] A. Einstein *Preuss. Akad. Wiss. Berlin*, Sitzungsberichte der physikalisch-mathematischen Klasse 154 (1916)
- [5] J.H. Taylor, L.A. Fowler, and P.M. McCulloch, *Nature* **277** (1979) 436
- [6] J.H. Taylor, and J.M. Weisberg, *Astrophysical Journal* (1989)
- [7] R.W.P. Drever et al., in “Quantum Optics, Experimental Gravitation and Measurement Theory”, eds. P. Meystre and M.O. Scully, Plenum Press, New York (1983) 503
- [8] R.W.P. Drever, in “Gravitational Radiation”, eds. N. Deruelle and T. Piran, North Holland, Amsterdam (1983) 321
- [9] B.J. Meers, “The frequency response of interferometric gravitational wave detectors”, *Physics Letters A*, **142**, no. 8-9, (1989) 465-70

- [10] D. Schnier, J. Mizuno, G. Heinzl, H. Lück, A. Rüdiger, R. Schilling, M. Schrempel, W. Winkler, K. Danzmann, “Power recycling in the Garching 30 m prototype interferometer for gravitational-wave detection”, *Phys. Lett. A* **225** (1997) 210-216
- [11] B.J. Meers, “Recycling in laser-interferometric gravitational-wave detectors”, *Physical Review D (Particles and Fields)* **38**, 2317-26 (1988).
- [12] K.A. Strain and B.J. Meers, “Experimental demonstration of dual recycling for interferometric gravitational-wave detectors”, *Physical Review Letters*, **66**, no.11, (1991) 1391-1394
- [13] M.M. Fejer, G.A. Magel, D.H. Jundt, and R.L. Byer, “Quasi-phase-matched second harmonic generation: tuning and tolerances”, *Journal of Quantum Electronics*, **28** no. 11 (1992) 2631-2654
- [14] J. Mizuno, K. Strain, P.G. Nelson, J.M. Chen, R. Schilling, A. Rüdiger, W. Winkler and K. Danzmann, “Resonant sideband extraction: A new configuration for interferometric gravitational wave detectors”, *Physics Letters A*, **175**, (1993) 273-276
- [15] J. Mizuno “Comparison of optical configurations for laser-interferometric gravitational wave detectors”, Ph.D. Thesis, University of Hannover, (1995)
- [16] G. Heinzl “Resonant Sideband Extraction - Neuartige Interferometrie für Gravitationswellendetektoren”, Diploma Thesis, University of Hannover (1995)
- [17] G. Heinzl, J. Mizuno, R. Schilling, W. Winkler, A. Rüdiger, K. Danzmann “An experimental demonstration of resonant sideband extraction for laser-interferometric gravitational wave detectors”, *Physics Letters A*, **217**, (1996) 305-314
- [18] G. Sagnac, *C. R. Acad. Sci.* **95**, 1410 (1913).
- [19] J. Anandan and R.Y. Chiao, “Gravitational radiation antennas using the Sagnac effect”, *General Relativity and Gravitation* **14**, no. 6, 515-521 (1982).

- [20] R. Weiss personal notes, July (1986)
- [21] The TAMA team “Gravity Wave Astronomy”, Report for Japanese government, Kyoto University, pg. 286-287 (1992)
- [22] Ke-Xun Sun, M.M. Fejer, E.K. Gustafson and R.L. Byer, “Sagnac interferometer for gravitational-wave detection”, *Physical Review Letters* **76**, no. 17, (1996) 3053-3056
- [23] A.E. Siegman, *Lasers* University Science Books, Mill Valley (1986)
- [24] S. Braccini, “Suspensions”, in *Gravitational Waves third Edoardo Amaldi conference*, ed. Syd Meshkov, AIP conference proceedings, 153-161 (2000).
- [25] Dhurandhar, S. V. Krolak, A. Lobo Detection of gravitational waves from a coalescing binary system-effect of thermal noise on the efficiency of the detector. *Monthly Notices of the Royal Astronomical Society* **237**, no. 2 (1989) 333-340
- [26] A. Gillespie and F. Raab, Thermal noise in the test mass suspensions of a laser interferometer gravitational-wave detector prototype, *Physics Letters A*, **178**, no. 5-6, (1993). 357-63.
- [27] F. Bondu and J.Y. Vinet, Mirror thermal noise in interferometric gravitational-wave detectors *Physics Letters A*, **198** no. 2 (1995) 74-8.
- [28] F. Bondu, P. Hello, J.Y. Vinet, Thermal noise in mirrors of interferometric gravitational wave antennas. *Physics Letters A* **246** no. 3-4 (1998) 227-36.
- [29] C.M. Caves, Quantum-mechanical noise in an interferometer, *Physical Review D (Particles and Fields)* **23** no. 8 (1981) 1693-708.
- [30] A. Yariv, *Optical Electronics*, Saunders College Publishing (1991)
- [31] H.A. Bachor, “A guide to experiments in quantum optics”, Wiley-VCH (1998)
- [32] C.M. Caves, Quantum-mechanical radiation-pressure fluctuations in an interferometer, *Physical Review Letters*, **45** no. 2 (1980) 75-79

- [33] P. Linsay, P. Saulson, R. Weiss and S. Whitcomb, “A Study of long baseline gravitational wave antenna system”, National Science Foundation Document (1983)
- [34] R.E. Vogt, R.W.P. Drever, K.S. Thorne, F.J. Raab and R. Weiss, “The construction, operation, and supporting research and development of a laser interferometer gravitational-wave observatory”, National Science Foundation Proposal (1989)
- [35] A. Abramovici, W.E. Althouse, R.W.P. Drever, Y. Gursel, S. Kawamura, F.J. Raab, D. Shoemaker, L. Sievers, R.E. Spero, K.S. Thorne, R.E. Vogt, R. Weiss, S.E. Whitcomb, and M.E. Zucker LIGO: the Laser Interferometer Gravitational-Wave Observatory, *Science* **256** 325-333, (1992)
- [36] B.C. Barrish and R. Weiss “LIGO and the Detection of Gravitational Waves”, *Physics Today*, **52**, no. 10, 44-50 (1999)
- [37] The GEO600 Team, “GEO600 - Proposal for a 600 m Laser-Interferometric Gravitational Wave Antenna”, MPQ Report **190** 18 p (1994)
- [38] C. Bradaschia, r. del Fabbro, A. di Virgilio, A. Giazotto, H. Kautzky, V. Montelatici, D. Passuello, A. Brillet, O. Cregut, P. Hello, C.N. Man, P.T. Manh, A. Marraud, D. Shoemaker, J.Y. Vinet, F. Barone, L. di Fiore, L. Milano, G. Russo, J.M. Aguirregabiria, H. Bel, J.P. Duruisseau, G. le Denmat, P. Tourrenc, M. Capozzi, M. Longo, M. Lops, I. Pinto, G. Rotoli, T. Damour, S. Bonazzola, J.A. Marck, Y. Gourghoulon, L.E. Holloway, F.E. Fuligni, V. Iafolla, and G. Natale, “The VIRGO project: a wide band antenna for gravitational wave detection”, *Nuclear Instruments and Methods in Physics Research, Section A (Accelerators, Spectrometers, Detectors and Associated Equipment)* **A289**, 518-25 (1990).

- [39] D. E. McClelland, D. G. Blair and R. J. Sandeman, “AIGO: A Southern Hemisphere Second Generation Gravitational Wave Observatory”, in *Seventh Marcel Grossman Meeting on General Relativity*, World Scientific, pp. 1418-1420 (1997).
- [40] D. E. McClelland, H.-A. Bachor, M. B. Gray, C. C. Harb and A. J. Stevenson, “Toward the development of a second generation long baseline laser interferometer for gravitational wave detection”, in *Seventh Marcel Grossman Meeting on General Relativity*, World Scientific, 1415-1417 (1997).
- [41] D. E. McClelland, M.B. Gray, D.A. Shaddock, B.J. Slagmolen, S.M. Scott, P. Charlton, B.J. Whiting, R.J. Sandeman, D.G. Blair, L. Ju, J. Winterflood, D. Greenwood, F. Benabid, M. Baker, Z. Zhou, D. Mudge, D. Ottaway, M. Ostermeyer, P.J. Veitch, J. Munch, M.W. Hamilton, and C. Hollitt, “Status of the Australian Consortium for Interferometric gravitational Astronomy”, in *Gravitational Waves third Edoardo Amaldi conference*, ed. Syd Meshkov, AIP conference proceedings, 140-149 (2000).
- [42] K. Tsubono, “300-m Laser Interferometer Gravitational Wave Detector (TAMA300) in Japan, in: *Gravitational Wave Experiments*, eds/: E. Coccia, G. Pizzella, and F. Ronga, World Scientific (1995) 112-114
- [43] K. Kuroda, Y. Kozai, M.-K. Fujimoto, M. Ohashi, R. Takahashi, T. Yamazaki, M.A. Barton, N. Kanda, Y. Saito, N. Kamikubota, Y. Ogawa, T. Suzuki, N. Kawashima, E. Mizuno, K. tsubono, K. Kawabe, N. Mio, S. Moriwaki, A. Araya, K. Ueda, K. Nakagawa, T. Nakamura, and members of the TAMA group, “Status of TAMA” in: *Gravitational Waves*, eds.: I. Ciufolini and F. Fidecaro, World Scientific, (1997) 100-107
- [44] M. Ando, K. Tsubono, “TAMA Project: Design and Current Status”, in *Gravitational Waves third Edoardo Amaldi conference*, AIP conference proceedings, 128-139 (2000).

- [45] S. Ezekiel and H.J. Arditty, ed., *Fiber-Optic Rotation Sensors and Related Technologies*, Springer-Verlag, New York **32** (1982)
- [46] D.A. Shaddock, M.B. Gray, D.E. McClelland, "Experimental demonstration of resonant sideband extraction in a Sagnac interferometer" *Applied Optics***37**, no. 34, 7995-8001 (1998).
- [47] E.J. Post, "Interferometric path-length changes due to motion", *Journal of the Optical Society of America*, **62** no. 2 (1972) 234-239
- [48] Freedman, A.P.; Ibanez-Meier, R.; Herring, T.A.; Lichten, S.M.; Dickey, J.O.; "Subdaily Earth rotation during the Epoch 1992 campaign", *Geophysical Research Letters*, **21**, no.9, 769-772 (1994).
- [49] P.T. Beyersdorf, M.M. Fejer and R.L. Byer "Polarization Sagnac interferometer with a common-path local oscillator for heterodyne detection", *J. Opt. Soc. Am. B* **16**, no. 9, (1999) 1354-1358
- [50] P.T. Beyersdorf, M.M. Fejer and R.L. Byer A Polarization Sagnac Interferometer with Post Modulation for Gravitational Wave Detection, *Optics Letters*, **24** no. 16 (1999) 1112-1114
- [51] R.W.P. Drever, talk at "10th International Conference on General Relativity and Gravitation", Padua (1983)
- [52] C.N. Man, D. Shoemaker, T.M. Pham, D. Dewey "External modulation techniques for sensitive interferometric detection of displacements", *Phys. Lett. A* **148** (1990) 8-16
- [53] K. Sun, M.M. Fejer, E.K. Gustafson and R.L. Byer, "Balanced heterodyne signal extraction in a postmodulated Sagnac interferometer at low frequency", *Optics Letters* **22**, 1359-61 (1997).
- [54] K. Sun, M.M. Fejer, E.K. Gustafson and R.L. Byer, "Balanced heterodyne signal extraction in a postmodulated Sagnac interferometer at low frequency", *Optics Letters* **22**, 1485-7 (1997).

- [55] L. Schnupp, Private communication (1986)
- [56] M. Regehr, F.J. Raab, and S.E. Whitcomb, “Demonstration of a power-recycled Michelson interferometer with Fabry-Perot arms by frontal modulation”, *Optics Letters*, **20**, (1995) 1507-1509
- [57] M. Regehr, “Signal Extraction and Control for an Interferometric Gravitational Wave Detector”, Ph.D. Thesis, California Institute of Technology, (1995)
- [58] J. Mizuno and I. Yamaguchi “Method for analyzing multiple-mirror coupled optical systems”, *Journal of the Optical Society of America A*, **16**, no.7, 1730-1739
- [59] B. Willke, N. Uehara, E.K. Gustafson, R.L. Byer, P.J. King, S.U. Seel and R.L. Savage, Jr. “Spatial and temporal filtering of a 10-W Nd:YAG laser with a Fabry-Perot ring-cavity premode cleaner” *Optics Letters***23**, no. 21, 1704-1706 (1998).
- [60] D. Herriott, H. Kogelnik, and R. Kompfner, “Off-Axis Paths in Spherical Mirror Interferometers”, *Applied Optics*, **3**, no. 4 523-526 (1964)
- [61] D. Herriott and H. Schulte, “Folded Optical Delay Lines”, *Applied Optics*, **4**, no. 8 883-889 (1965)
- [62] H. Kogelnik, “Imaging of Optical Modes – Resonators with Internal Lenses”, *The Bell Systems Technical Journal*, 455-494 (1965)
- [63] J.B. McManus, P.L. Keabian, M.S. Zahniser, “Astigmatic mirror multipass absorption cells for long-path-length spectroscopy”, *Applied Optics*, **34**, no.18, 3336-3348, (1995)
- [64] N. Nakagawa, B.A. Auld, E.K. Gustafson, and M. M. Fejer “Estimation of thermal noise in the mirrors of laser interferometric gravitational wave detectors: Two point correlation function” *Review of Scientific Instruments*, **68** no. 9 (1997) 3553-3556

- [65] N. Nakagawa, E.K. Gustafson, P.T. Beyersdorf, and M.M. Fejer, "Estimating the off resonance thermal noise in mirrors, Fabry-Perot interferometers and delay-lines: the half infinite mirror with uniform loss", Submitted to Physical Review D, Sept 2000
- [66] J.Y. Vinet, V. Brisson, S. Braccini, "Scattered light noise in gravitational wave interferometric detectors: Coherent effects", Phys Rev D, **54**, no. 2, 1276-1286 (1996)
- [67] R. Schilling, L. Schnupp, W. Winkler, H. Billing, K. Maischberger and A. Rüdiger, "A method to blot out scattered light effects and its application to a gravitational wave detector", Journal of Physics E, **14**, no. 1, 65-70, (1981)
- [68] L. Schnupp, W. Winkler, K. Maischberger, A. Rüdiger and R. Schilling, "Reduction of noise due to scattered light in gravitational wave antennae by modulating the phase of the laser light", Journal of Physics E, **18**, no. 6, 482-485, (1985)
- [69] P.T. Beyersdorf, S. Traeger and M.M. Fejer "Removal of scattered light noise from the measurement band of a delay-line Sagnac interferometer by sweeping the laser frequency", to be published in optics letters
- [70] M.W. Regehr, "Signal Extraction and Control for an Interferometric Gravitational Wave detector" MIT Ph.D. Thesis, (1995)
- [71] M.W. Regehr, Raab, F.J. and Whitcomb, S.E., "Demonstration of a power-recycled Michelson interferometer with Fabry-Perot arms by frontal modulation", **20**, no. 13, (1995) 1507-1509
- [72] S. Rowan, "Design considerations for bottom stage LIGO II suspension", talk at Stanford University (1999).
- [73] A. Blaquiere, "Spectre de puissance d'un oscillateur non lineaire perturbe par le bruit", Annales de Radioelectricite **8** no. 36 (1953) 153

- [74] J.A. Armstrong, "Theory of Interferometric Analysis of Laser Phase Noise", *JOSA*, **56**, no. 8, 1024-1031 (1966)
- [75] J.B. Camp, H. Yamamoto, S.E. Whitcomb, and D.E. McClelland "Analysis of light noise in a recycled Michelson interferometer with Fabry-Perot arms", *JOSA A* **17**, no. 1 120-128 (2000)
- [76] A. Yariv, *Quantum Electronics 3<sup>rd</sup> Ed.*, Ch 21, (New York: Joyhn Wiley and Sons, 1989).
- [77] W. Winkler, K. Danzmann, A. Rüdiger, and R. Schilling, *Physical Review A* **44** no. 11, 7022-7035 (1990).
- [78] E.G. Loewen, E. Popov, *Diffraction Gratings and Application*, Marcel Dekker Inc., New York, pp. 507 (1997).
- [79] P. Hello and J.Y. Vinet, *J. Phys. France* **51**, 1267-1282 (1990).
- [80] P. Hello and J.Y. Vinet, *J. Phys. France* **51**, 2243-2261 (1990).
- [81] R.W. Waynant, M.N. Ediger (Eds.), *Electro-Optics Handbook*, McGraw-Hill (1993).
- [82] Ke-Xun Sun and R.L. Byer, "All-reflective Michelson, Sagnac, and Fabry-Perot interferometers based on grating beam splitters", **23**, no. 8, (1998) 567-569
- [83] S. Traeger, P. Beyersdorf, E. Gustafson, R. Beausoleil, R.K. Route, R.L. Byer and M.M. Fejer, "All-Reflective Interferometry For Gravitational-Wave Detection" in: *Proceedings of the 3rd Edoardo Amaldi Conference on Gravitational Waves*, ed.: Sydney Meshkov, AIP conference proceedings 523, Melville (2000)
- [84] S. Traeger, P. Beyersdorf, L. Goddard, E.K. Gustafson, M.M. Fejer and R.L. Byer, *Polarization Sagnac interferometer with a reflective grating beam splitter*, *Optics Letters* **25** 10 722-724 (2000)

- [85] B.W. Shore, M.D. Perry, J.A. Britten, R.D. Boyd, M.D. Feit, H.T. Nguyen, R. Chow, G.E. Loomis and Lifeng Li, “Design of high-efficiency dielectric reflection gratings”, *JOSA A* **14**, no. 5 1124-1136 (1997)
- [86] D. Dewey, “A Search for Astronomical Gravitational Radiation with an Interferometric Broad Band Antenna”, MIT Thesis (1996)